

OCEANOGRAPHIC MESOSCALE FEATURES OFF THE
WEST GREENLAND COAST:
SATELLITE IMAGE ANALYSIS AND MODELLING

CENTRE FOR NEWFOUNDLAND STUDIES

**TOTAL OF 10 PAGES ONLY
MAY BE XEROXED**

(Without Author's Permission)

VEMBU SUBRAMANIAN







National Library
of Canada

Bibliothèque nationale
du Canada

Acquisitions and
Bibliographic Services

Acquisitions et
services bibliographiques

395 Wellington Street
Ottawa ON K1A 0N4
Canada

395, rue Wellington
Ottawa ON K1A 0N4
Canada

Your file *Votre référence*

ISBN: 0-612-89675-7

Our file *Notre référence*

ISBN: 0-612-89675-7

The author has granted a non-exclusive licence allowing the National Library of Canada to reproduce, loan, distribute or sell copies of this thesis in microform, paper or electronic formats.

L'auteur a accordé une licence non exclusive permettant à la Bibliothèque nationale du Canada de reproduire, prêter, distribuer ou vendre des copies de cette thèse sous la forme de microfiche/film, de reproduction sur papier ou sur format électronique.

The author retains ownership of the copyright in this thesis. Neither the thesis nor substantial extracts from it may be printed or otherwise reproduced without the author's permission.

L'auteur conserve la propriété du droit d'auteur qui protège cette thèse. Ni la thèse ni des extraits substantiels de celle-ci ne doivent être imprimés ou autrement reproduits sans son autorisation.

In compliance with the Canadian Privacy Act some supporting forms may have been removed from this dissertation.

Conformément à la loi canadienne sur la protection de la vie privée, quelques formulaires secondaires ont été enlevés de ce manuscrit.

While these forms may be included in the document page count, their removal does not represent any loss of content from the dissertation.

Bien que ces formulaires aient inclus dans la pagination, il n'y aura aucun contenu manquant.

Canada

**OCEANOGRAPHIC MESOSCALE FEATURES OFF THE WEST
GREENLAND COAST: SATELLITE IMAGE ANALYSIS AND MODELLING**

By

©Vembu Subramanian

**A thesis submitted to the School of Graduate Studies in partial fulfillment of the
requirements for the degree of Master of Science**

Environmental Science

Memorial University of Newfoundland

June, 2000

St. John's

Newfoundland

Canada

Abstract

The establishment of a station to receive National Oceanic Atmospheric Administration (NOAA) satellite data at the Northwest Atlantic Fisheries Centre, St. John's, Newfoundland in 1994 greatly expanded the AVHRR coverage of the coastal waters of the Newfoundland and Labrador region to include the West and East Greenland waters. The thermal infrared imagery selected from the data received at this station provide a valuable new perspective on oceanographic phenomena occurring in the waters off the coast of West Greenland. This perspective could not be attained using conventional shipboard and *in situ* oceanographic measurement techniques. A rich spectrum of mesoscale oceanographic features is revealed in the analyzed thermal infrared imagery, and the spatial and temporal scales of the various features such as West Greenland Current meanders, frontal waves and eddies are described first in this thesis. Then, a three-dimensional, primitive equation, regional, ocean circulation model of the West Greenland region based on the NOAA Geophysical Fluid Dynamics Laboratory (GFDL) Modular Ocean Model (MOM2 - version 2) code is used to elucidate the dynamics involved in modelling the current meanders and eddies. First, a numerical experiment was carried out by forcing the model from rest using an idealized initial density front with a passive open boundary condition in which there is no forcing specified at the open boundary to test and verify the satisfactory behaviour of the MOM2 model. In response to the initial forcing, two baroclinic Kelvin waves were formed and the waves were found to propagate out of

the model domain through the open boundaries without affecting the interior solution. Next, a numerical experiment was carried out to investigate the combined effects of wind and thermal forcings in the generation of current meanders and eddies. Results of the experiment show the development of a poleward surface current and an opposite flowing undercurrent. In time the core of the undercurrent becomes wider and seen to displace the core of the surface current, suggesting that there may be both vertical and horizontal shear. As a result the currents could become unstable, and lead to the development of current meanders and eddies.

Acknowledgements

I thank my supervisors Dr. Brad de Young and Dr. Jim Helbig for their continuous encouragement, support and guidance.

I thank School of Graduate Studies, Memorial University of Newfoundland for awarding Graduate Fellowship during my full-time enrollment in the programme. I am grateful to Dr. Nathan Rich for his support and encouragement throughout my course of studies.

I would also like to thank the computer system administrators Allan Goulding and Ken Forward of Memorial University of Newfoundland and Charlie Bromley and Dave Senciall of Northwest Atlantic Fisheries Center, St. John's for their help. I would like to thank my friend Fraser Davidson for his friendship and support throughout my studies at Memorial University.

Finally, I would like to thank my wife, Hamsa Subramanian, who deserves my warmest appreciation for understanding and timely help.

Table of Contents

1	Introduction	1
1.1	The need for regular monitoring of the marine environment	1
1.2	Objectives of this study	3
1.3	Organization of the thesis	5
2	The West Greenland Current system	6
2.1	Surface Currents off West Greenland	6
2.2	Hydrographic sections off the coast of West Greenland	8
3	Satellite Remote Sensing of the Marine Environment	22
3.1	The oceanographic capabilities of satellite sensors	22
3.2	Some potential oceanographic applications of NOAA-AVHRR data . . .	30
3.2.1	Fronts, meanders and eddies	30
3.2.2	Sea surface temperature	32
3.2.3	Ocean currents	34
3.2.4	Fisheries	36
4	The NOAA-AVHRR Image analysis	38
4.1	The TIROS/NOAA Satellites and AVHRR characteristics	39

4.2	NOAA-AVHRR data processing	42
4.2.1	Calibration of NOAA-AVHRR data	42
4.2.2	AVHRR image navigation	45
4.2.3	Cloud detection and land masking	60
5	Mesoscale features off the West Greenland coast observed in NOAA-AVHRR infrared imagery	66
5.1	AVHRR data selection and processing	66
5.2	Results	68
5.2.1	Observations of mesoscale surface circulation features	69
5.2.2	Spatial and temporal scale analysis of mesoscale features	74
5.3	Discussion	96
6	Modelling mesoscale circulation features of the West Greenland Current	101
6.1	Model Description	102
6.2	Numerical Experiments	108
6.2.1	Experiment 1: Test Case Run	108
6.2.2	Experiment 2: Role of wind and thermal forcings in the generation of current meanders and eddies	116
6.3	Summary	133

7 Summary and Discussion	136
---------------------------------	------------

References	140
----------------------	-----

List of Tables

3.1	Satellite sensors used for oceanographic applications.	26
4.1	Spectral characteristics and primary uses of AVHRR.	41
4.2	The basic characteristics of AVHRR.	42
5.1	List of AVHRR thermal imageries for the year 1995.	67
5.2	List of AVHRR thermal imageries for the year 1996.	68
6.1	Temperature, salinity and density in the model domain.	110

List of Figures

2.1	Surface currents in the northern North Atlantic Ocean in the summer of 1958 (Wegner, 1973). Bi : Baffin Island Current, Eg : East Greenland Current, Ei : East Iceland Current, Gu : Gulf Stream, Ir : Irminger Current, La : Labrador Current, Na : North Atlantic Current, Nc : North Cape Current, Ng : Norwegian Current, Ni : North Iceland Current, Po : Portugal Current, Sb : Spitsbergen Current, Wg : West Greenland Current. Solid current axes: relatively warm currents. Broken current axes: relatively cold currents.	9
2.2	Locations of oceanographic sections and CTD stations off the coast of West Greenland in July 1994 and January 1995.	10
2.3	Potential temperature and salinity along the Cape Farewell section, July 1994.	11
2.4	Potential temperature and salinity along the Cape Desolation section, July 1994.	11
2.5	Potential temperature and salinity along the Frederikshaab section, July 1994.	12
2.6	Potential temperature and salinity along the Fylla Bank section, July 1994.	12

2.7	Vertical profiles of temperature, salinity and potential density for the farthest station of hydrographic sections off the coast of West Greenland (July 1994).	13
2.8	T-S diagrams for the hydrographic sections off the coast of West Greenland (July 1994).	14
2.9	Potential temperature and salinity along the Fylla Bank section, November 1994 (Stein, 1994).	15
2.10	Potential temperature and salinity along the Cape Farewell section, January 1995.	17
2.11	Potential temperature and salinity along the Cape Desolation section, January 1995.	17
2.12	Potential temperature and salinity along the Frederikshaab section, January 1995.	18
2.13	Vertical profiles of temperature, salinity and potential density for the farthest station of hydrographic sections off the coast of West Greenland (January 1995).	19
2.14	T-S diagrams for the hydrographic sections off the coast of West Greenland (January 1995).	20
3.1	Sketch to illustrate the electromagnetic spectrum.	23

3.2	Approximate transmittance of electromagnetic waves through the atmosphere (Reeves, 1975).	23
3.3	Optical pathways to a sensor (Bullard, 1983a).	25
4.1	Processing steps for NOAA-AVHRR data collected at NWAFC satellite laboratory.	43
4.2	Orbital and scanning geometry at solution time t and intermediate time t' for indirect navigation.	48
4.3	An unregistered raw image of Greenland region (Channel 4, NOAA-14, August 15, 1995, 0545 UTC).	59
4.4	Georegistered NOAA-14 (Channel 4, August 15, 1995, 0545 UTC) image of West Greenland region created using indirect navigation method (1 st order navigation).	61
4.5	Georegistered NOAA-14 (Channel 4, August 15, 1995, 0545 UTC) image of West Greenland region with coastline map overlay.	62
4.6	Georegistered NOAA-14 (Channel 4, August 15, 1995, 0545 UTC) image of West Greenland region with coastline map overlay (2 nd order navigation).	63
4.7	NOAA-14 (Channel 4, August 15, 1995, 0545 UTC) image of West Greenland region after cloud detection and land masking. Also shown are bathymetric contours (500 - 3000 m).	65

5.1	NOAA-14 AVHRR channel 4 image of the West Greenland region that show the surface conditions on July 29, 1995, 1658 UTC. Also shown are the bathymetric contours.	70
5.2	NOAA-14 AVHRR channel 4 image of the West Greenland region that show the surface conditions on July 27, 1996, 1634 UTC. Also shown are the bathymetric contours.	71
5.3	NOAA-14 AVHRR channel 4 image of the West Greenland region that show the surface conditions on October 23, 1995, 0644 UTC. Also shown are the bathymetric contours.	72
5.4	NOAA-12 AVHRR channel 4 image of the West Greenland region that show the surface conditions on October 25, 1996, 2119 UTC. Also shown are the bathymetric contours.	73
5.5	NOAA-12 AVHRR image, 30 June 1995, 2146 UTC. Also shown are the bathymetric contours.	75
5.6	NOAA-12 channel 4 image, 8 July 1995, 1048 UTC.	76
5.7	NOAA-12 channel 4 image, 29 July 1995, 1131 UTC.	79
5.8	NOAA-12 channel 4 image, 30 July 1995, 1109 UTC.	80
5.9	NOAA-14 channel 4 image, 10 August 1995, 1629 UTC.	81
5.10	NOAA-14 channel 4 image, 11 August 1995, 0629 UTC.	82
5.11	NOAA-14 channel 4 image, 15 August 1995, 0545 UTC.	84
5.12	NOAA-12 channel 4 image, 15 August 1995, 1022 UTC.	85

5.13 NOAA-14 channel 4 image, 21 November 1995, 1621 UTC.	86
5.14 NOAA-14 AVHRR image, 22 June 1996, 1613 UTC. Also shown are the bathymetric contours.	88
5.15 NOAA-12 channel 4 image, 16 July 1996, 2126 UTC.	89
5.16 NOAA-14 channel 4 image, 24 July 1996, 1707 UTC.	90
5.17 NOAA-14 channel 4 image, 27 July 1996, 2046 UTC.	91
5.18 NOAA-14 channel 4 image, 10 August 1996, 2041 UTC.	92
5.19 NOAA-14 channel 4 image, 14 September 1996, 2115 UTC.	93
5.20 NOAA-12 channel 4 image, 15 September 1996, 1109 UTC.	94
6.1 The arrangement of variables in the horizontal plane for a grid with equal grid spacing in both directions.	107
6.2 Level 3 (500 m) temperature after 23 days.	113
6.3 Level 3 (500 m) temperature after 53 days.	114
6.4 Velocity vectors at level 1 (25 m) at the end of 23 days.	115
6.5 Velocity vectors at level 5 (1850 m) at the end of 23 days.	116
6.6 ETOPO5 bottom topography (depth in metres).	117
6.7 (a) Wind forcing and (b) The initial field of surface temperature used in this experiment.	118
6.8 Zonal velocity contours at level 1 (25 m) after 5 and 10 days of model run.	119
6.9 Zonal velocity contours at level 1 (25 m) after 20 and 30 days of model run.	120

6.10 Meridional velocity contours at level 1 (25 m) after 5 and 10 days of model run.	121
6.11 Meridional velocity contours at level 1 (25 m) after 20 and 30 days of model run.	122
6.12 Temperature contours at level 2 (150 m) after 5 and 10 days of model run.	123
6.13 Temperature contours at level 2 (150 m) after 20 and 30 days of model run.	124
6.14 Velocity vectors at level 1 (25 m) after 5 and 10 days of model run. . . .	126
6.15 Velocity vectors at level 1 (25 m) after 20 and 30 days of model run. . . .	127
6.16 Vertical section of meridional velocity at 61° N after 5 and 10 days of model run.	128
6.17 Vertical section of meridional velocity at 61° N after 20 and 30 days of model run.	129
6.18 Stream function after 5 and 10 days of model run. Positive values (solid lines) and negative values (dashed lines) indicate anticyclonic and cyclonic circulation respectively.	130
6.19 Stream function after 20 and 30 days of model run. Positive values (solid lines) and negative values (dashed lines) indicate anticyclonic and cyclonic circulation respectively.	131

Chapter 1

Introduction

1.1 The need for regular monitoring of the marine environment

Marine fisheries, oil, natural gas and seabed minerals are significant sources of natural and economic wealth. Reaping the benefits of these marine resources requires careful management, not only in the traditional coastal areas, but also in the vast, relatively unexplored frontier zones - the open ocean. The management of fish stocks and of the national and international fishing fleets and the rapid growth in oil and gas exploration which has led to increased shipping activities require accurate observation and increased monitoring of coastal and open oceans. In addition, the risk of environmental contamination due to outflow of polluted rivers, off-shore industry, shipping (oil spills, accidents) will pose particular challenges in the management of marine resources. Efficient management of marine resources and effective management of activities within the coastal zone is largely dependent upon the ability to identify, measure and analyze a number of processes and parameters that operate or react together in the highly dynamic marine environment. In this regard, measurements are required of the physical, chemical and biological features of coastal and open areas of the oceans. These measurements would

include temperature, current, sea state, bathymetry, water colour, sea ice and suspended sediments. *In situ* measurements have long been the principal source of information on the hydrography of the coastal and open zones of the oceans. Local measurements of temperature, salinity, turbidity, currents and water samples are made with the use of instruments on research ships and drifting buoys. Such measurements are accurate and can monitor conditions in varying water depths. However, surveying a large area by making a series of local measurements is both time consuming and expensive. Furthermore, this method of measurement is inadequate if the ocean phenomenon being monitored changes rapidly in time and space.

The scale of the coastal and open ocean zones requires that *in situ* measurement techniques be supplemented by remote sensing, thereby making it possible to observe much larger areas synoptically. Remote sensing from aircraft has proved to be useful for monitoring the marine environment (e.g. marine fisheries, sea surface temperature, ice and iceberg conditions), however, aircraft are restricted in range and by weather conditions, and are expensive to operate. In addition, some phenomena require observation during storms when aircraft are grounded (e.g. high waves, ice break-up, strong winds). Remote sensing of the marine environment from satellites overcomes many of these limitations and is especially useful for obtaining small-scale high resolution data in coastal zones. The advantage of satellite remote sensors over airborne or surface level sensors lies in the frequency of coverage of satellite overflights; in the regularity and uniformity

of coverage; in the relative low cost of each pass, as compared with the high cost of the average aircraft operation; and in the ability of satellites to collect data over larger areas and in remote locations where access is impossible. Satellite remote sensing also suffers from problems such as cloud cover in the case of sensors that rely on solar illumination as the source of radiation (optical and infrared sensors). In such cases, the data from the satellites which illuminate their target with their own pulse of electromagnetic radiation (microwave sensors) and observe the returned signal could be used. Microwave satellites suffers from availability problems, such as timeliness, coverage and limited frequency of overpasses. However, despite these problems satellite remote sensing provides the most cost-effective method to monitor and observe large areas of the oceans.

1.2 Objectives of this study

Starting in the late 1970s, the infrared images from Advanced Very High Resolution Radiometer (AVHRR) on the National Oceanic and Atmospheric Administration (NOAA) series of satellites have been used to compute the sea surface temperature and to study the sea surface thermal features such as fronts, meanders and eddies in the ocean. The fronts, meanders and eddies have significant biological consequences as they are regions of strong convergence of surface currents and relatively strong vertical motions, which can advect nutrients into the euphotic zone thus increasing the primary ocean productivity. Although it is possible to study these features using hydrographic data obtained

using *in situ* measurements, satellite infrared imagery allows us to observe their evolution, growth and propagation. The use of NOAA-AVHRR thermal infrared images to analyse mesoscale oceanographic features is well documented in the regions of Gulf Stream (Legeckis, 1975; Apel, 1980; Richardson, 1980; Churchill and Cornillon, 1991; Lee *et al.*, 1991), Kurushio (Kimura and Sugimoto, 1993), California Current (Ikeda and Emery, 1984; Randerson and Simpson, 1993), East Greenland Current (Wadhams, 1981; Bruce, 1995), Norwegian Coastal Current (Johannessen *et al.*, 1989) and Labrador Current (LeBlond, 1982; Ikeda, 1987). But, very little attention has been devoted to satellite remote sensing off the coast of West Greenland. There have been no publications on West Greenland despite the fact that there are important questions of oceanography and fisheries that could be addressed with satellite remote sensing data. The establishment of a NOAA satellite receiving station at Northwest Atlantic Fisheries Centre (NWAFC), St. John's, Newfoundland in 1994 that covers all coastal waters of Newfoundland, Labrador and a large part of West/East Greenland gives us an excellent opportunity to study the oceanographic phenomena occurring off the coast of West Greenland using satellite data. In this thesis, I offer a first description of the mesoscale oceanographic features (fronts, meanders and eddies) observed off the coast of West Greenland using NOAA-AVHRR infrared images acquired at NWAFC and examine their spatial and temporal scales. I then proceed to study the complicated dynamics of these features with the latest version (version 2) of the NOAA Geophysical Fluid Dynamics Laboratory (GFDL) Modular Ocean Model (MOM2) of the West Greenland region.

1.3 Organization of the thesis

The remainder of the thesis is organized as follows: Chapter 2 describes the surface circulation and hydrography off the West Greenland coast. In chapter 3, an overview of the satellite remote sensing of the marine environment which describes the oceanographic capabilities of satellite sensors (ocean colour, infrared and microwave) and some potential oceanographic applications of NOAA-AVHRR infrared data is presented. In chapter 4, we present the details of NOAA-AVHRR satellite system and the data processing steps for the AVHRR data collected at NWAFC satellite laboratory. Chapter 5 describes the results of the spatial and temporal scale analysis of the oceanographic features observed in the NOAA-AVHRR infrared images off the coast of West Greenland. In chapter 6, we present the results of the numerical experiments performed with the MOM2 regional ocean circulation model of the West Greenland. Chapter 7 provides the summary and conclusions.

Chapter 2

The West Greenland Current system

2.1 Surface Currents off West Greenland

The subpolar gyre of the North Atlantic Ocean includes the North Atlantic Current, the Irminger Current, the West and East Greenland Currents, and the Labrador Current. The surface currents in the northern North Atlantic derived from the analysis of the International Geophysical Year (IGY) data set by Wegner (1973) are shown in Fig. 2.1. The West Greenland Current (depicted as **Wg** in Fig. 2.1) is a mixture of two currents: the cold East Greenland Current (**Eg**) and the warm Irminger Current (**Ir**). The East Greenland Current derives its thermohaline properties from the Arctic Ocean and carries cold ($-1.8\text{ }^{\circ}\text{C}$) and low salinity (< 34.5) water of the Arctic origin southwestward along the east coast of Greenland. During much of the year the current is ice covered, and transports considerable sea ice in winter and spring (Aagaard, 1989). Only in the late summer and fall is the current not covered by ice. This southwestward flowing cold current is joined at the shelf break by the warm ($4 - 6\text{ }^{\circ}\text{C}$) and saltier ($34.95 - 35.1$) water of Irminger Current (Clarke, 1984). According to Lee (1968), the Irminger current arises from the northern branch of the North Atlantic Current (**Na**), which turns northwards

near the mid-Atlantic ridge. A part of the North Atlantic Current turns southwestwards in Denmark Strait, and then flows along the edge of the East Greenland Current as Irminger Current.

The East Greenland and Irminger Currents flow together around the southern tip of Greenland into the Labrador Sea as West Greenland Current. It is seen from the Fig. 2.1 that the main direction of the West Greenland Current is northwestwards along the coast, but a branch of the current turns westward between 60° N and 64° N. The current that continues north up the west coast of Greenland branches off to the west and turns southward in Baffin Bay as Baffin Island Current (**Bi**), also called as Baffin Current. The Baffin Island Current is a combination of West Greenland Current inflow and the outflow of cold Arctic Ocean waters from the channels of the Canadian Arctic region. The southward flowing Baffin Island Current joins the branch of West Greenland Current that turned westward between 60° N and 64° N and continues to flow south as the Labrador Current down the west side of Labrador Sea back into the Atlantic. On the West Greenland shelf, the northward flowing West Greenland Current close to the coast has temperatures around 2°C , and the Irminger Current ($> 4^{\circ}\text{C}$), which still marks the outer edge of the cold component is found at greater depths towards north. The Labrador Current water has temperatures around 0°C or less and salinities 30 to 34.

The East Greenland and Irminger Current components of the West Greenland Current system, and variations in the flow of each component could play an important role in the

climatic conditions around West Greenland region, and the marine ecology, especially the West Greenland cod fishery. Hermann *et al.*, (1965) studied the effect of temperature and currents on the distribution of cod larvae at West Greenland. According to them, the most important cod spawning grounds seem to be along the western slopes of the banks, mainly at depths between 200 and 600 m in the relatively warm water of the Irminger Current. The water temperature over the banks and their western slopes, where the cod eggs and larvae are found, depends very much on the relative strength of cold East Greenland and warm Irminger water components, and play an important role in the survival of cod eggs and larvae. The eggs and larvae are carried northward by the West Greenland Current or westward by the westerly branch of the current. The larvae that drift westward with the westerly branch are probably lost for the Greenlandic cod stock, but may contribute to the recruitment of the Labrador cod stock.

2.2 Hydrographic sections off the coast of West Greenland

In this section, the thermohaline conditions off the coast of West Greenland region based on the analysis of hydrographic observations collected during July 1994 and January 1995 are described. These data were obtained from the office of the International Council for the Exploration of the Sea (ICES) in Denmark and the Institut für Seefischerei, Hamburg, Federal Republic of Germany respectively. Locations of oceanographic sections and the CTD stations off the coast of West Greenland are shown in Fig. 2.2.

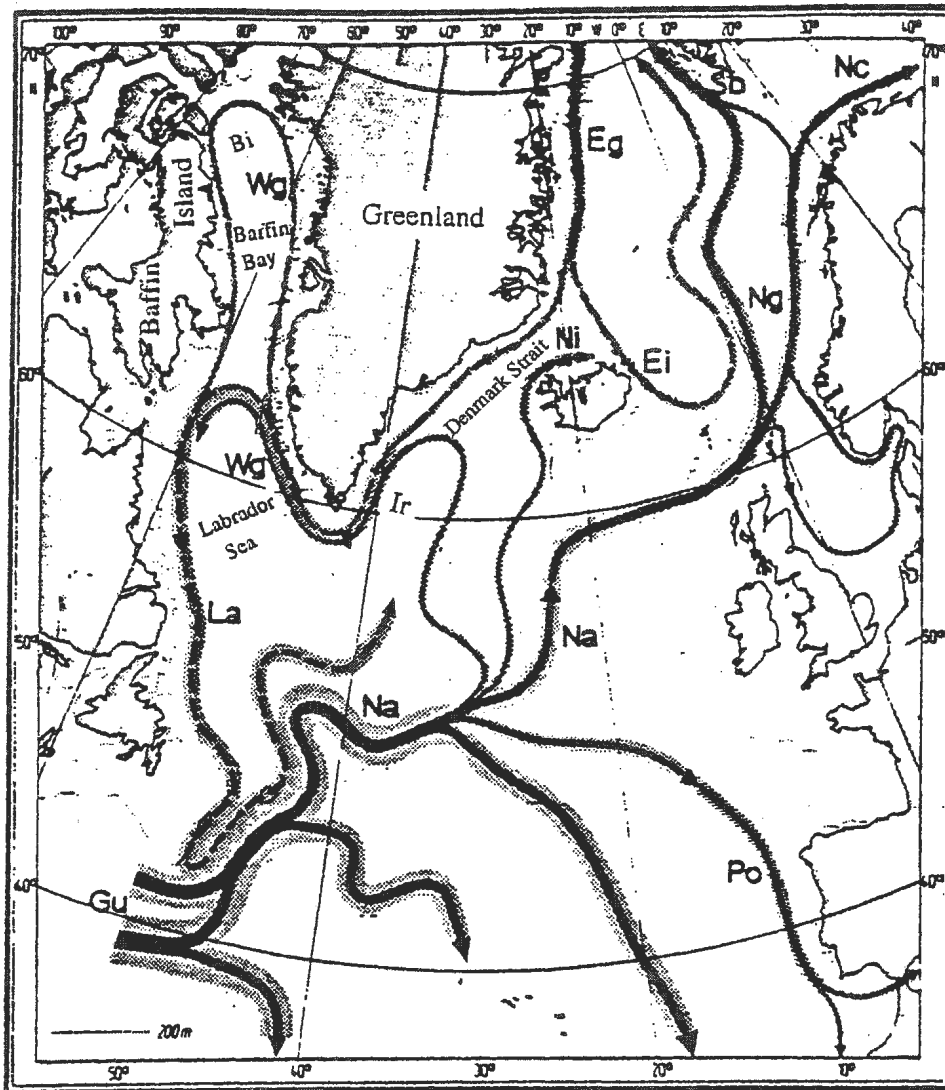


Figure 2.1: Surface currents in the northern North Atlantic Ocean in the summer of 1958 (Wegner, 1973). Bi: Baffin Island Current, Eg: East Greenland Current, Ei: East Iceland Current, Gu: Gulf Stream, Ir: Irminger Current, La: Labrador Current, Na: North Atlantic Current, Nc: North Cape Current, Ng: Norwegian Current, Ni: North Iceland Current, Po: Portugal Current, Sb: Spitsbergen Current, Wg: West Greenland Current. Solid current axes: relatively warm currents. Broken current axes: relatively cold currents.

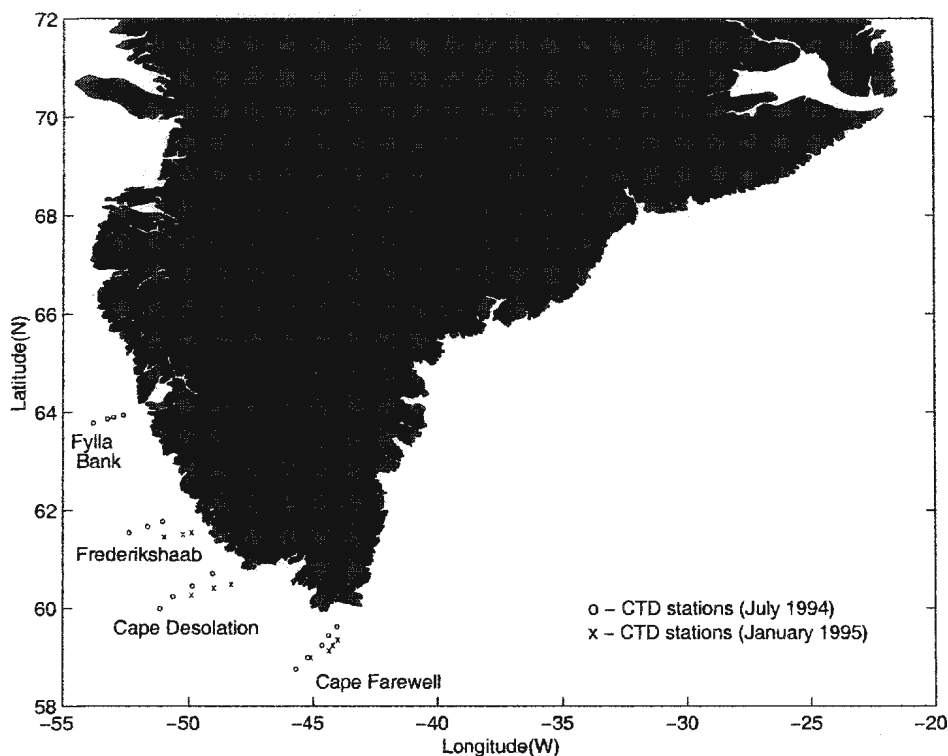


Figure 2.2: Locations of oceanographic sections and CTD stations off the coast of West Greenland in July 1994 and January 1995.

The vertical thermohaline structure on the Cape Farewell, Cape Desolation, Frederikshaab and Fylla Bank sections for July 1994 are shown in Fig. 2.3 to Fig. 2.6. Cape Farewell and Cape Desolation sections (Fig. 2.3 and Fig. 2.4) show the existence of a thermohaline front separating the East Greenland Current (cold and fresh) and Irminger Current (warm and saline), components of the West Greenland Current. Water colder than 4 °C and salinities less than 34.5 found at the surface in both the sections mark the outer edge of the East Greenland Current. Offshore of this, the Irminger Current water with temperatures greater than 4 °C and salinities greater than 34.5 extends to

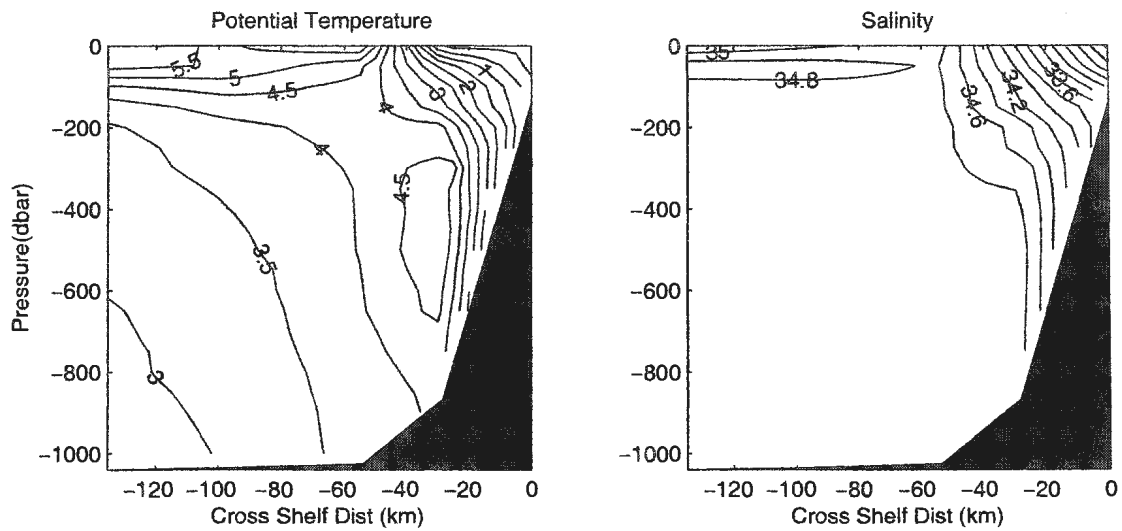


Figure 2.3: Potential temperature and salinity along the Cape Farewell section, July 1994.

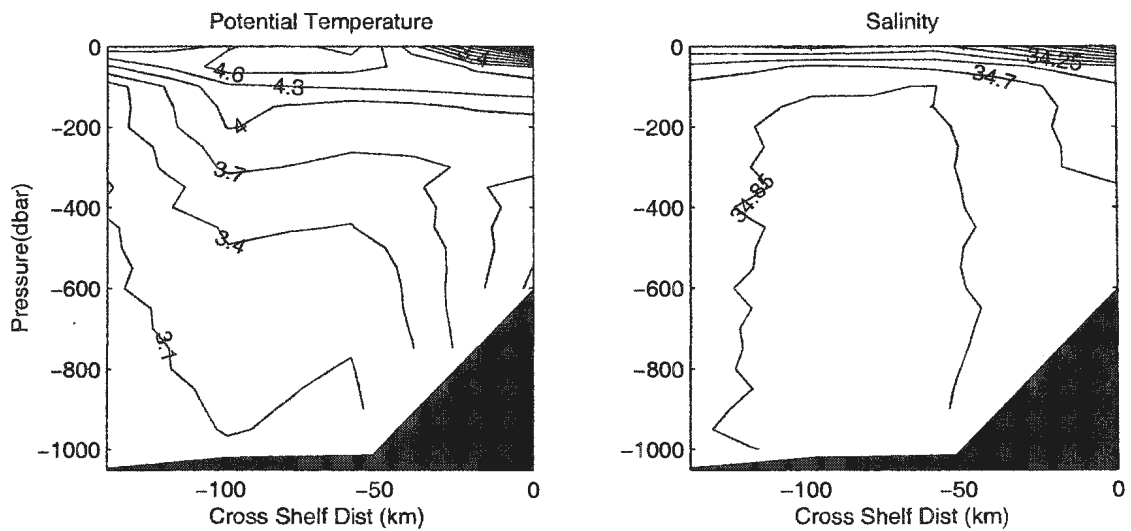


Figure 2.4: Potential temperature and salinity along the Cape Desolation section, July 1994.

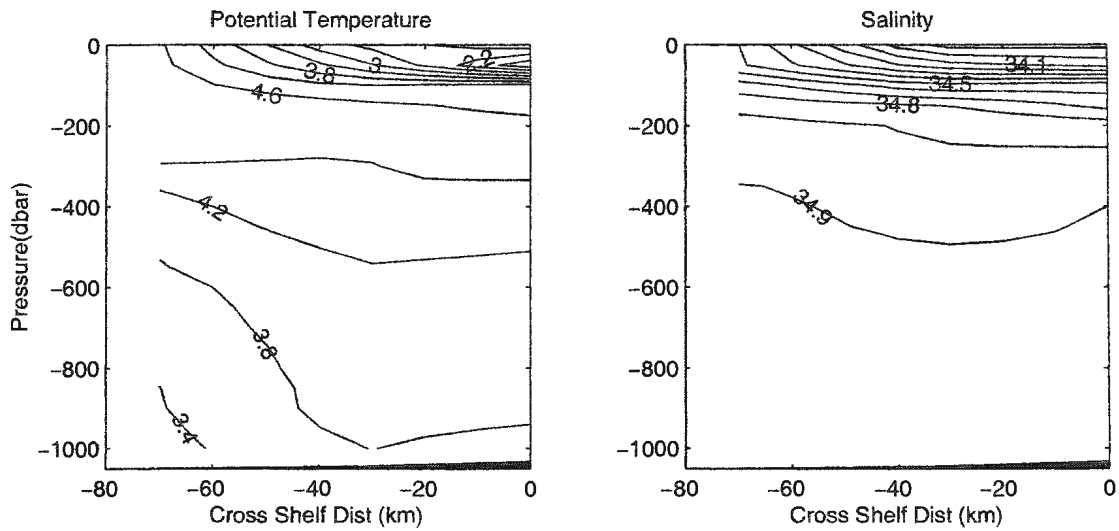


Figure 2.5: Potential temperature and salinity along the Frederikshaab section, July 1994.

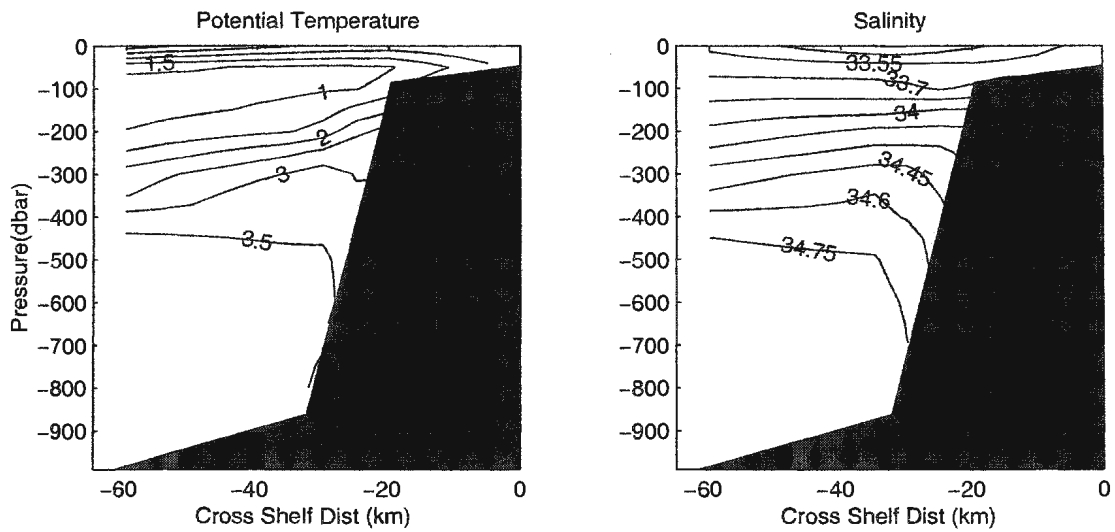


Figure 2.6: Potential temperature and salinity along the Fylla Bank section, July 1994.

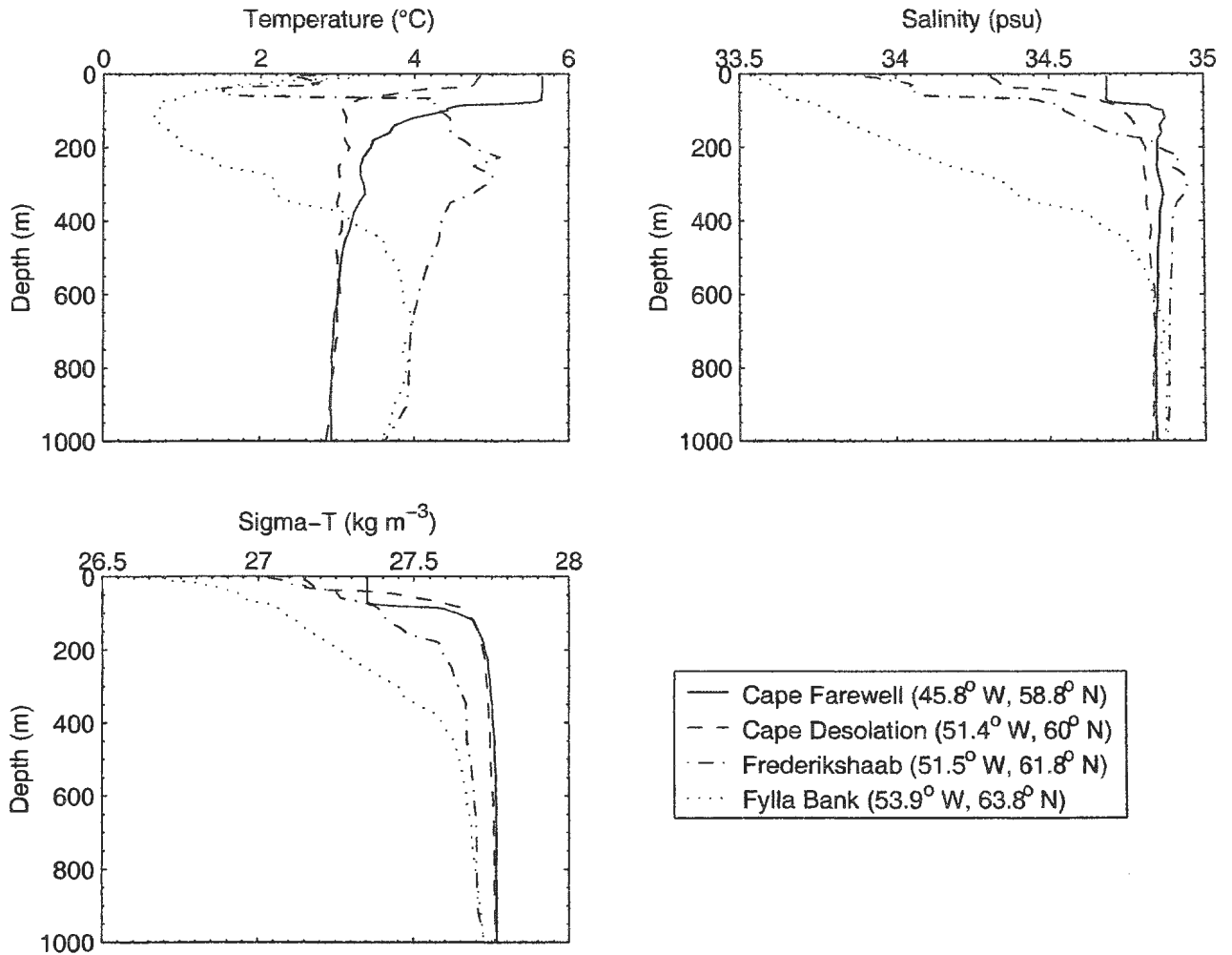


Figure 2.7: Vertical profiles of temperature, salinity and potential density for the farthest station of hydrographic sections off the coast of West Greenland (July 1994).

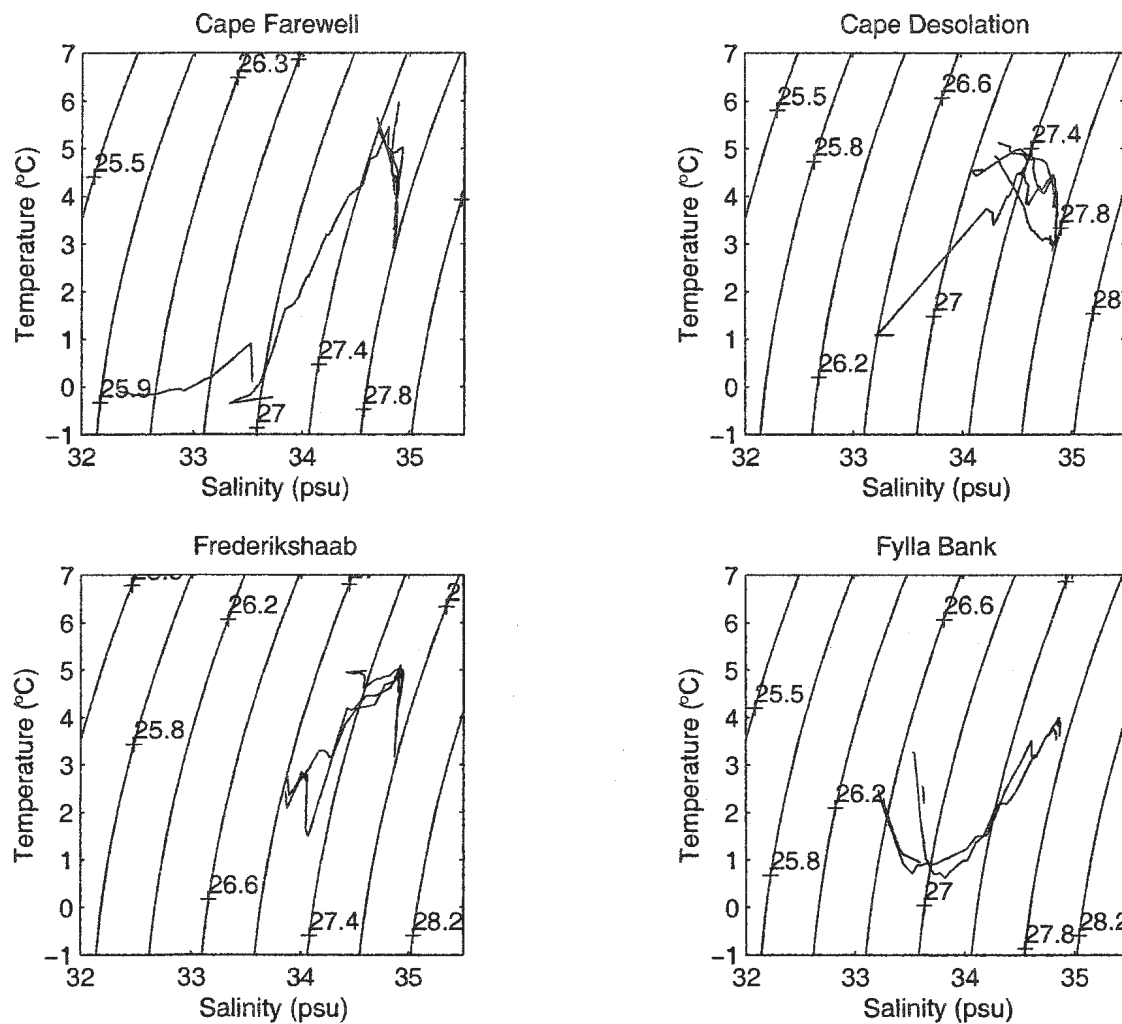


Figure 2.8: T-S diagrams for the hydrographic sections off the coast of West Greenland (July 1994).

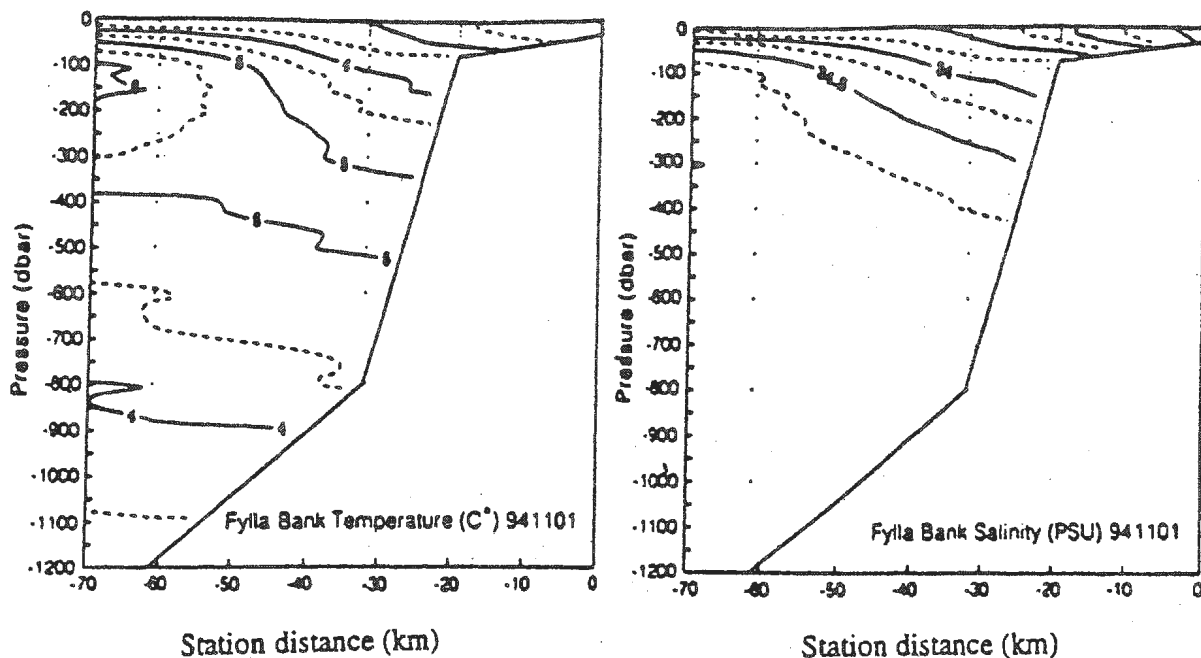


Figure 2.9: Potential temperature and salinity along the Fylla Bank section, November 1994 (Stein, 1994).

depths of 1000 m. The vertical distributions of temperature and salinity off Frederikshaab (Fig. 2.5) and Fylla Bank (Fig. 2.6) also indicate the presence of East Greenland Current water along the shelf, and Irminger water offshore. But, the depth at which the Irminger Current water is found in these sections is greater than that observed in the Cape Farewell and Cape Desolation sections. The effect of mixing during the northward passage of West Greenland Current can be seen in these sections with the reduction in temperature and salinity of the Irminger Current water compared to Cape Farewell section. The presence of Irminger Current water offshore at greater depths in these sections and effect of mixing are best illustrated in the vertical profiles of temperature, salinity

and potential density (Fig. 2.7) of the outermost station located off-shore and T-S diagrams (Fig. 2.8) of the hydrographic sections off the coast off West Greenland in July 1994. The positional (latitude and longitude) values of the stations chosen to illustrate the vertical profiles are also mentioned in Fig. 2.7. The thermohaline conditions along the Fylla Bank section (Fig. 2.6) during July 1994 indicates the presence of cold water with temperatures $1\text{ }^{\circ}\text{C}$ and salinity less than 34 between the depths of 100-200 m, an indication of the presence of Arctic water from the Baffin Island Current. The presence of this water of Arctic origin has also been observed and reported by Buch (1982) in their analysis of the temperature distributions along West Greenland. The hydrographic conditions as observed in November 1994 along the Fylla Bank section, adapted from Stein (1994), are shown in Fig. 2.9 for comparison with the conditions observed during July 1994 (Fig. 2.6). Fig. 2.9 shows the presence of warm ($> 4.5\text{ }^{\circ}\text{C}$) high saline (> 34.5) water (Irminger Component) at depths below 100 m. This indicates the dominance of Irminger Current water during November compared to July, and shows a mesoscale variability (semi-annual signals of the two current components) in West Greenland waters. This also agrees with the results of Buch (1982) and Stein and Buch (1985) who noted that the cold, near-coastal East Greenland Current component attains its maximum influence on the West Greenland Current in early summer (June), whereas the warm Irminger component has its maximum influence in late autumn (November).

The thermohaline conditions as observed during January 1995 on the Cape Farewell,

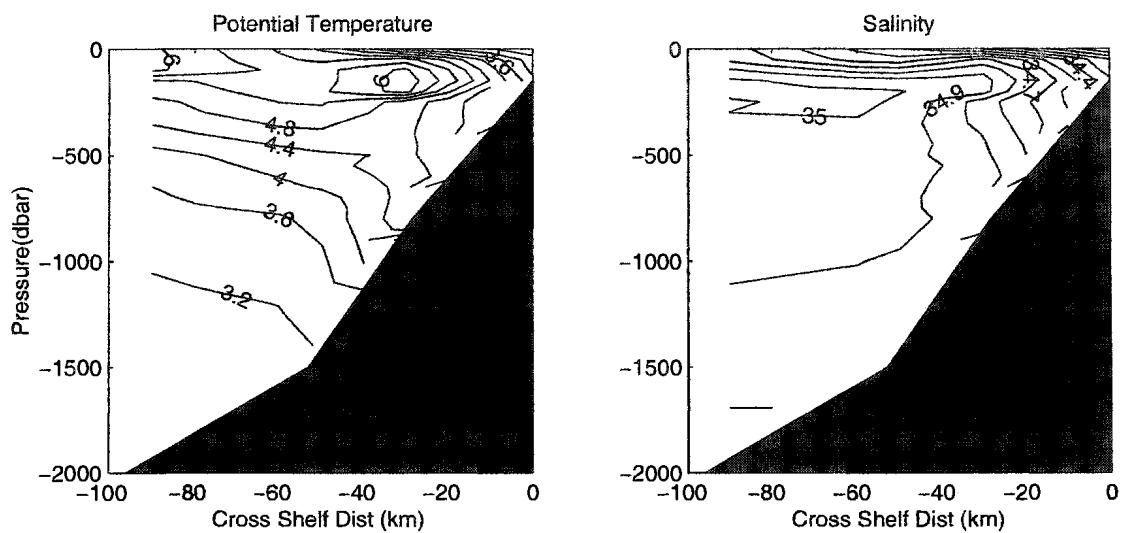


Figure 2.10: Potential temperature and salinity along the Cape Farewell section, January 1995.

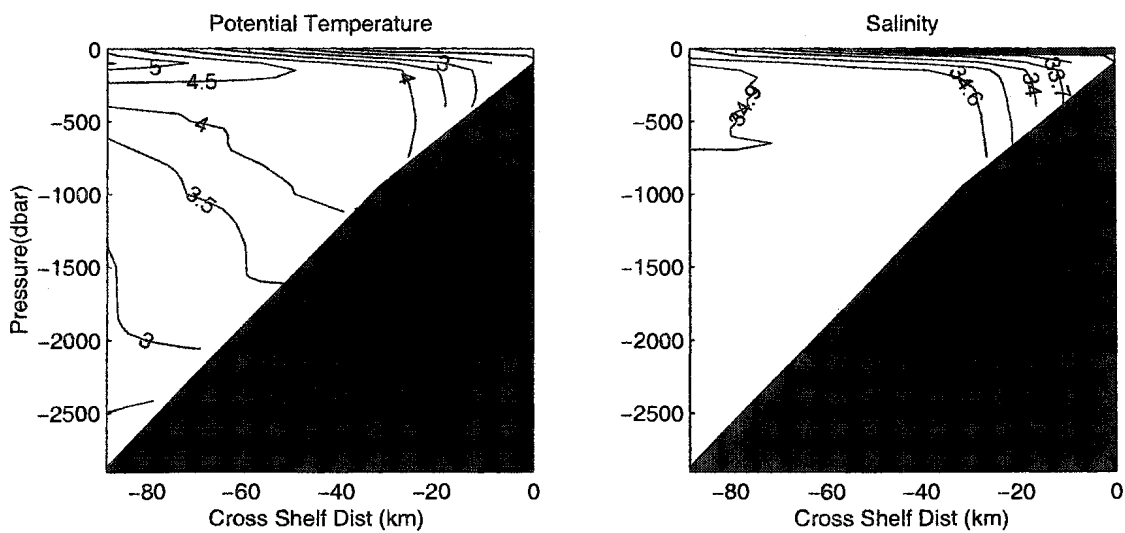


Figure 2.11: Potential temperature and salinity along the Cape Desolation section, January 1995.

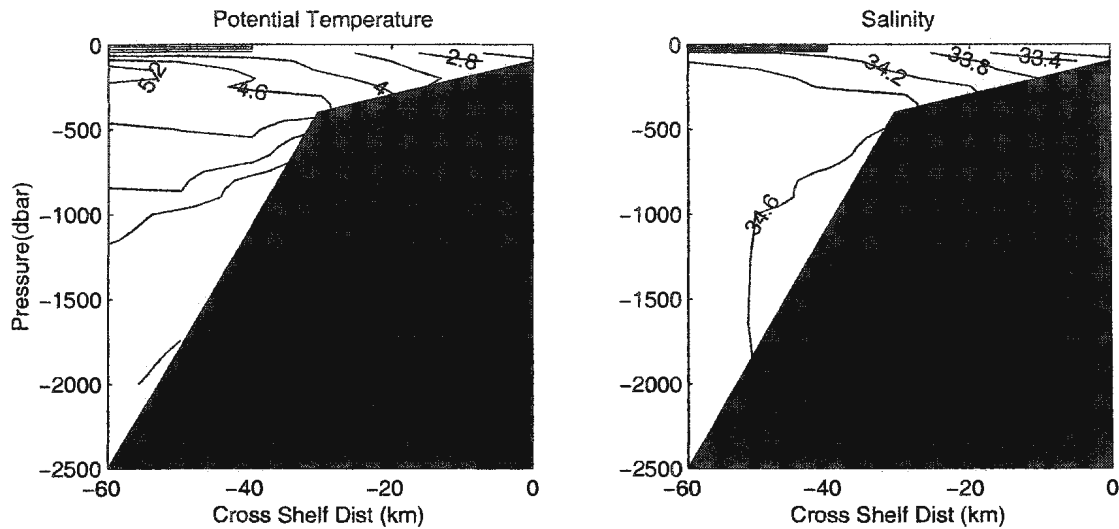


Figure 2.12: Potential temperature and salinity along the Frederikshaab section, January 1995.

Cape Desolation and Frederikshaab section are shown Fig. 2.10 to Fig. 2.12. The vertical distribution of temperature and salinity along these sections in January 1995 indicates the presence of Irminger Current water ($6\text{ }^{\circ}\text{C}$, 35) offshore and East Greenland Current water ($3\text{ }^{\circ}\text{C}$, < 34.5) along the shelf. But, the temperature and salinity values of the Irminger Current water observed along these sections during January 1995 are higher than those observed during July 1994. In the Cape Desolation and Frederikshaab sections (Fig. 2.11 and Fig. 2.12) there is a small decrease in the offshore salinity values, and both the sections indicate a front that separates cold diluted surface layer from the warm saline Irminger Current water. The vertical profiles of temperature, salinity and potential density of the outermost station located off-shore and T-S diagrams of the hydrographic sections off the coast off West Greenland in January 1995 are shown in

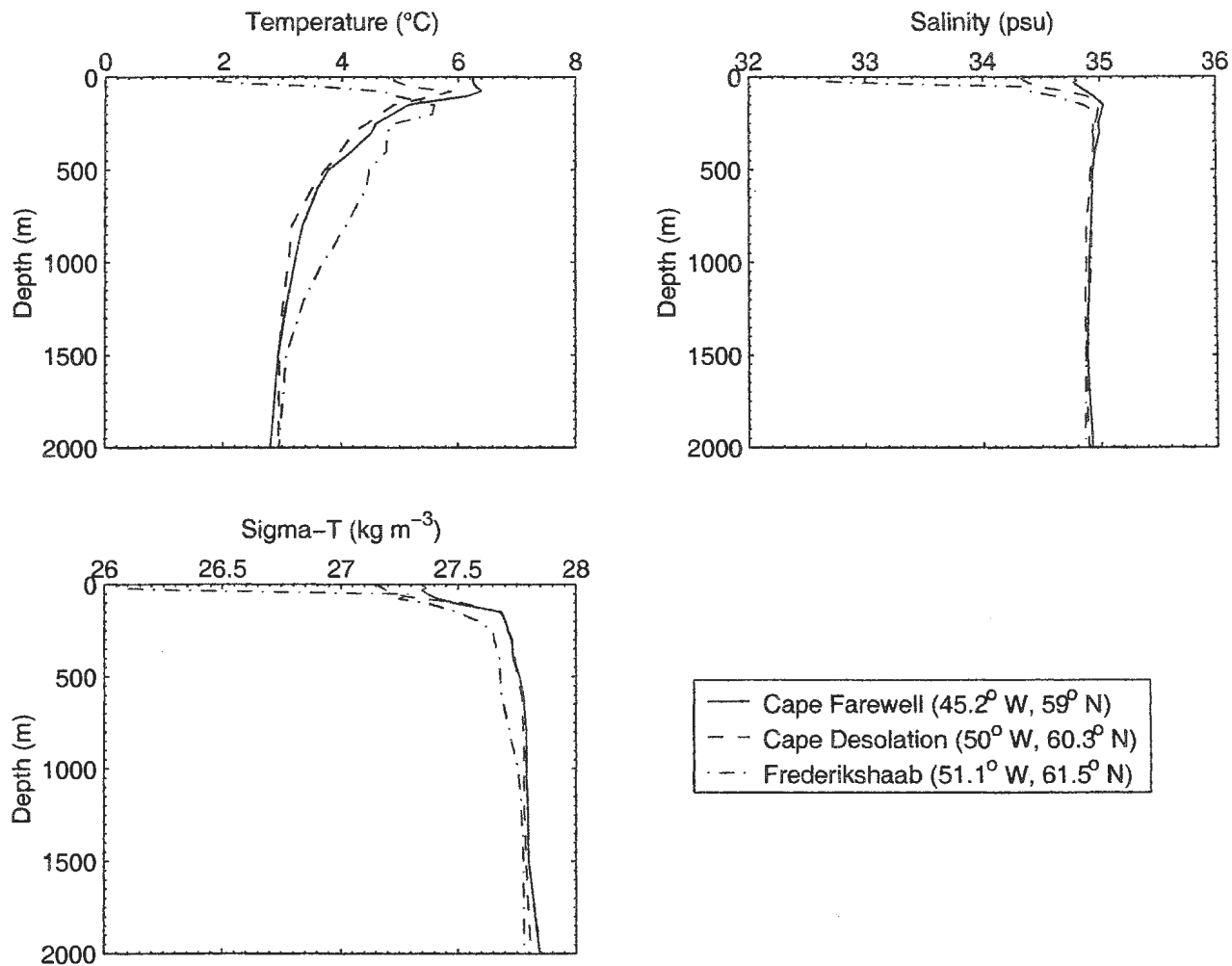


Figure 2.13: Vertical profiles of temperature, salinity and potential density for the farthest station of hydrographic sections off the coast of West Greenland (January 1995).

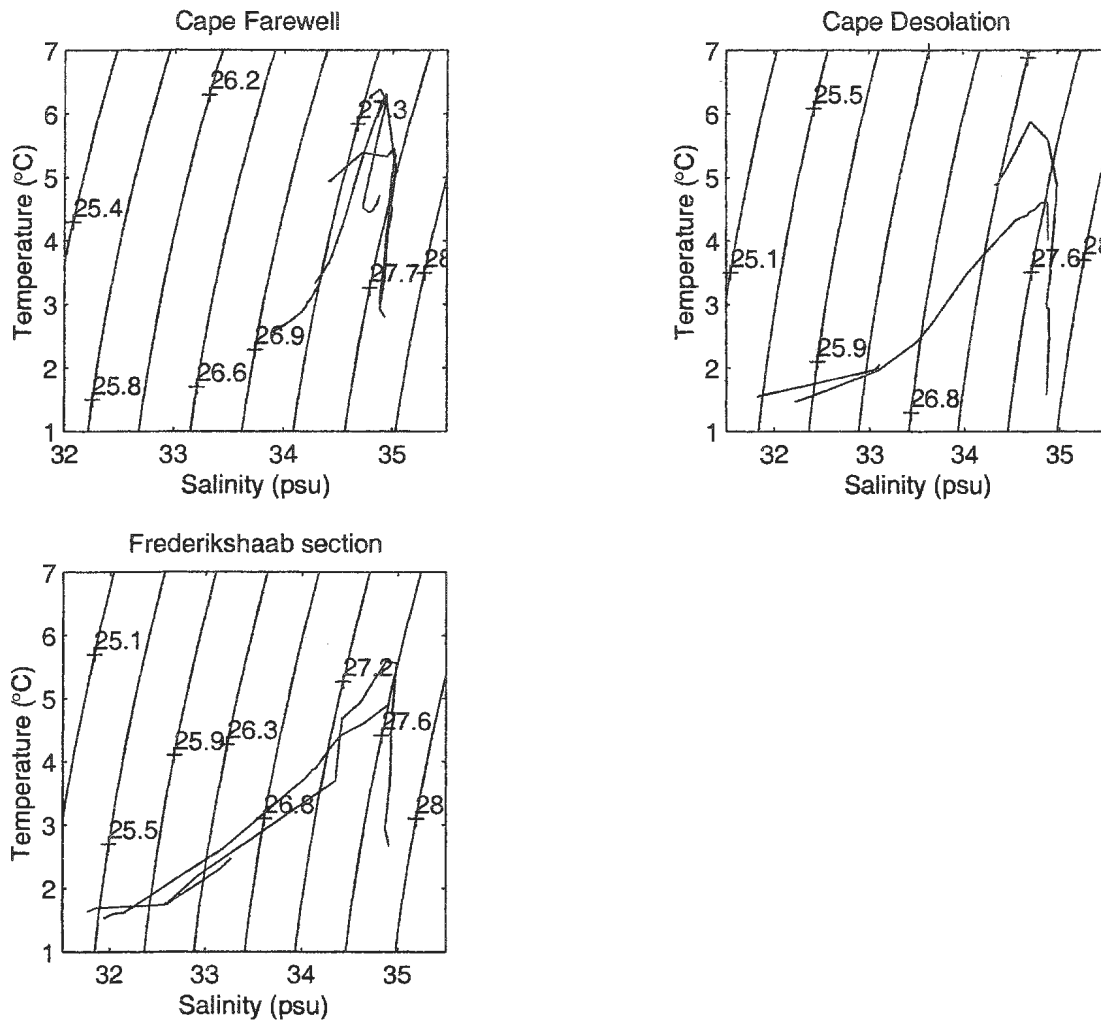


Figure 2.14: T-S diagrams for the hydrographic sections off the coast of West Greenland (January 1995).

Fig. 2.13 and Fig. 2.14. All three sections indicated the presence of Labrador Sea Water (with temperatures from 3 - 4 °C and salinity less than 34.9) at depths between 1500 and 2000 m. The Labrador Sea Water (LSW) develops its characteristics by convective formation in the central Labrador Sea (Lee and Ellet, 1967; Lazier, 1973; Talley and McCartney, 1982; Clarke and Gascard, 1983). Low salinity and high oxygen content are typical of this water mass which is found at mid-depth north of 40° N in the North Atlantic Ocean.

Chapter 3

Satellite Remote Sensing of the Marine Environment

3.1 The oceanographic capabilities of satellite sensors

Satellite remote sensing techniques depend on data collected from sensors onboard the polar-orbiting and geostationary satellites. The different information about the sea is carried by different frequencies of electromagnetic waves, with the result that suitable sensors that operate at particular frequencies have to be developed and mounted on satellites to retrieve information about particular oceanographic parameters. Satellite sensors have been developed to operate in the visible, infrared and microwave regions of the electromagnetic spectrum (Fig. 3.1). The choice of wavelength bands is governed firstly by the application and secondly by the atmospheric transmission spectrum. The approximate transmittance of electromagnetic waves through atmosphere depends strongly on wavelength (Fig. 3.2). The atmosphere (which consists of air, water vapour, other gases and aerosol particles) absorbs most radiation with a wavelength less than 400 nm. There is an atmospheric window (where the atmosphere is fairly transparent to electromagnetic radiation) in the visible wavelength range (400 - 750 nm), and also at select bands within infrared, thermal infrared and microwave wavelengths. These

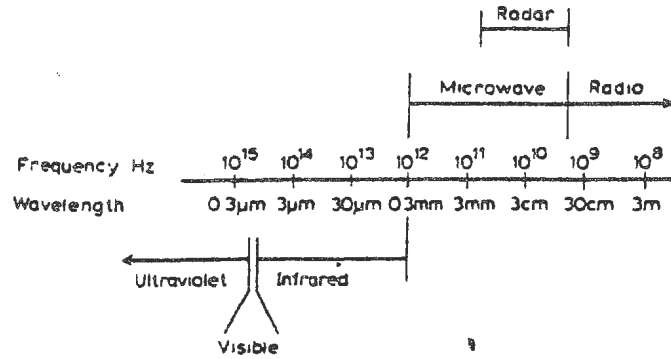


Figure 3.1: Sketch to illustrate the electromagnetic spectrum.

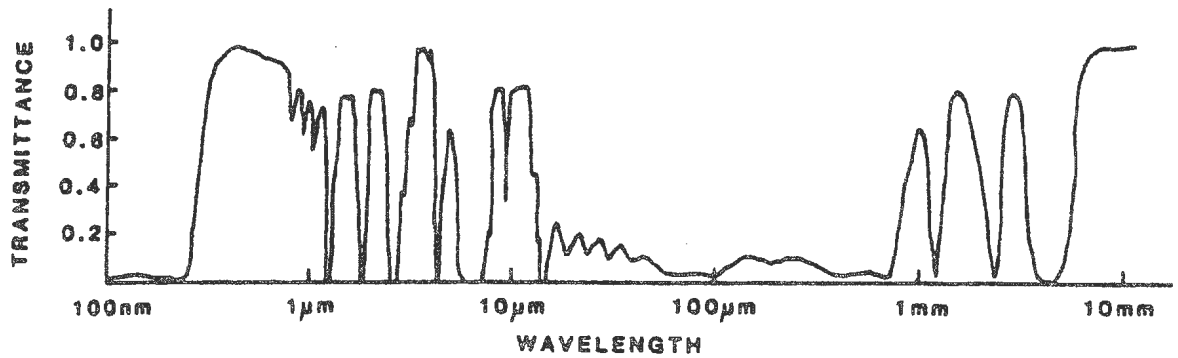


Figure 3.2: Approximate transmittance of electromagnetic waves through the atmosphere (Reeves, 1975).

wavelength bands have therefore been exploited for remote sensing. Past experience with the visible, infrared and microwave sensors flown on either an aircraft or a satellite, has shown that four basic sea surface properties (colour, temperature, slope and roughness) can be measured to useful accuracies. The ocean features (physical, chemical, biological or geological) must produce a surface signature in one of these four parameters if they are to be monitored from space.

Optical (visible) wavelength sensors are passive (meaning they rely on naturally occurring radiation), and depend on solar illumination as the initial radiation source. Fig. 3.3 illustrates the variety of possible pathways for light rays reaching a sensor flown on a satellite. The sunlight reaches the sea surface either directly or as skylight after being scattered by molecular and aerosol particles present in the atmosphere. After reaching the sea surface, some of the energy is reflected at the air-sea interface with the remainder absorbed by the ocean. The transmitted light is scattered or absorbed as it interacts with water molecules or encounters dissolved or particulate material present in the water. Part of the transmitted light is scattered in the backward direction (backscattering) and finds its way back into the atmosphere. If the sensor viewing angle is selected to avoid direct sun glitter, the radiation that comes from the backscattering processes at the sea surface can convey information regarding phytoplankton, suspended sediment or yellow substance (dissolved organic detrital material) in the water. As the visible light can penetrate several metres below the sea surface, the visible wavelength sensors are therefore

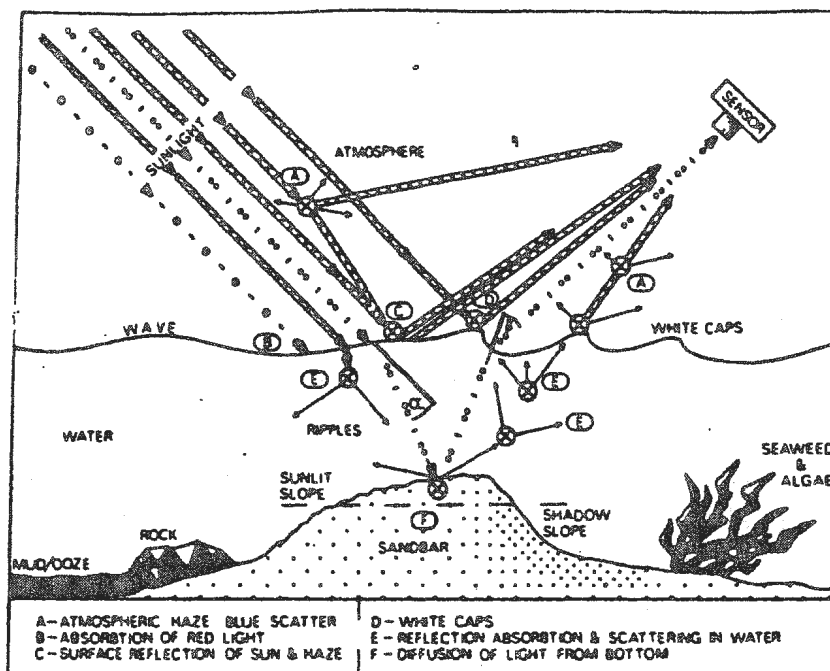


Figure 3.3: Optical pathways to a sensor (Bullard, 1983a).

Table 3.1: Satellite sensors used for oceanographic applications.

Sensor type	Examples	Satellite vehicle	Active /Passive	Measured physical parameter	General oceanographic applications	Possible retrievable oceanographic parameters
Visible and near IR radiometers	Multi Spectral Scanner (MSS) CZCS SeaWIFS	LANDSAT NIMBUS-7 SeaWIFS/ Seastar	passive	solar radiation backscattered from below and by the surface	ocean colour, water quality, bathymetry, bottom substrate sea-surface roughness, and surface slicks	near-surface suspended sediment and phytoplankton concentration, water depth in shallow clear seas
Thermal IR radiometers	AVHRR ATSR	TIROS/ NOAA ERS-1,2	passive	thermal emission from the sea and some solar reflection	sea surface temperature and sea surface thermal transfer conditions	sea surface temperature, surface heat flux
Microwave	SMMR	SEASAT NIMBUS-7	passive	sea-surface microwave emission, and reflected solar and atmospheric emission	Sea surface temperature emissivity and environmental factors controlling it, surface films and slicks	sea surface temperature and surface heat flux, salinity, sea state wind and wave conditions
Altimeter, Nadir-viewing radar	ALT	GOES SEASAT ERS-1,2 TOPEX/ POSEIDON	active	return time, shape and strength of pulse	height and slope of sea surface, surface roughness	ocean currents, tides, geoid information, significant wave height, sea state surface wind speed
Side-looking radar, Synthetic Aperture Radar	SCAT SAR	SEASAT ERS-1,2 RADARSAT	active	strength of return pulse in different view directions	surface roughness including directional information	surface wind speed and direction, directional wave spectra
High-resolution imaging radar	SAR	SEASAT ERS-1,2 RADARSAT	active	strength of return pulse from small areas of sea surface along with Doppler information	surface roughness	swell wave patterns, internal wave patterns and sea-bed topography

unique amongst remote sensing devices in being able to respond directly to conditions in the upper part of the water column. All other wavelengths can only reveal conditions at the surface or within a depth of less than a millimetre. In shallow seas (depths less than 20 m), light reflected at the sea bed can be seen from space provided the water is fairly clear. Thus these sensors can be used to identify bottom sediment and bathymetry. Visible sensors can also detect some surface features such as oil slicks, depending on their optical transmission properties. The Nimbus-7 satellite which was operational from 1979 to 1986 carried a visible wavelength radiometer, the Coastal Zone Colour Scanner (CZCS) designed primarily to observe ocean colour and to retrieve information on the concentration of phytoplankton. Recently, Sea-viewing Wide Field-of-view Sensor (SeaWiFS), was launched in August 1997 as a follow-on sensor to the CZCS to provide quantitative data on global ocean bio-optical properties, from which the concentration of phytoplankton can be estimated.

The near-infrared wavelength sensors are effectively complementary to the visible sensors, although the absorption in the sea rapidly increases, and 1 μm wavelength radiation penetrates only a few millimetres. This is in contrast to land applications where the reflected infrared radiation is a valuable remote-sensing indicator for identifying plant species or surface substrate types. The sensors that operate in the middle infrared wave band 3 - 4 μm , where the atmosphere is fairly transparent (Fig. 3.2), will record appreciable amounts of reflected solar energy in the day-time, but in the absence of solar

reflection at night-time will record radiation emitted by the sea surface itself. At 10 - 12 μm the emitted radiation dominates and the infrared sensors (thermal infrared sensors) are used for estimating the sea surface temperature. The Advanced Very High Resolution Radiometer (AVHRR) sensor mounted on the National Oceanic and Atmospheric Administration (NOAA) series of satellites had spectral bands in the near-infrared, infrared and thermal infrared wavelengths permitting determination of sea surface temperature. Passive radiometers such as Along-Track Scanning Radiometer (ATSR) and Satellite Multichannel Microwave Radiometer (SMMR) are also used for retrieving sea surface temperature. The emitted radiation depends also on the emissivity of the sea surface. If multichannel measurements are made across the infrared and microwave part of the electromagnetic spectrum it is possible in principle to extract information not only about temperature but also emissivity and the parameters on which it depends, including salinity and surface films, oil spills, etc. Some potential oceanographic applications of NOAA-AVHRR data are outlined in the next section.

Microwave sensors (active sensors) illuminate their target (the sea) with their own pulse of electromagnetic radiation and then observe the reflected signal. There is scope to measure not only the amplitude but also the phase of the reflected signal, and the travel time of the pulse, all of which can yield information about the sea surface when suitably analysed. By recording the return time for a pulse directed towards the satellite sub-point, the radar altimeter (ALT) measures the height of the sea surface relative to its

own position, and if this can be fixed then it is possible to determine the absolute height of the sea surface. Oceanographic applications of this information include the study of tides, ocean circulation and ocean topography. In addition, the deformation of the microwave pulse on reflection carries information about the significant wave height of the ocean waves. The scatterometer (SCAT) emits an oblique pulse of microwave radiation, and measures the intensity of the backscattered return. Since this backscattered intensity depends on the surface roughness at length scales comparable to the wavelength of the radiation, it carries information about the sea state over the illuminated area. Depending on the particular wavelength used, this can be interpreted in terms of the near surface wind magnitude, the surface wind stress, or the energy in the surface wave field. By viewing the same area of the sea surface from different directions, a measure of wind or wave direction can be achieved. The Synthetic Aperture Radar (SAR) operates essentially in a similar manner as the scatterometer, but it measures the timing and phase of the backscattered signal as well as its amplitude. Using suitable processing techniques it is possible to reproduce an image of the backscattering strength of the surface i.e., its roughness as seen by the radar. SAR achieves a very high spatial resolution, of order tens of metres, and the roughness it measures is due to small waves and ripples of a few centimetres in length. Oceanographic applications of SAR include images of swell patterns, ship wakes, slicks due to sea surface contamination by hydrocarbons or floating debris, internal waves and bottom topographical features. The radar altimeter, scatterometer and SAR can penetrate through the clouds and have been flown on satellites

such as SEASAT, ERS-1 and 2, TOPEX-POSEIDON and RADARSAT. The different types of satellite sensors discussed in this section, the satellite vehicles they were flown on, the physical parameters measured by them, and their oceanographic applications are summarized in Table. 3.1.

3.2 Some potential oceanographic applications of NOAA-AVHRR data

3.2.1 Fronts, meanders and eddies

Fronts in the ocean represent a boundary between two distinct water types, in which the temperature and/or salinity, and hence the density, have strong horizontal gradients. Fronts occur on spatial scales extending from fractions of a meter to tens of kilometres (Bowman and Iverson 1987), and are found in several situations in the ocean. The Gulf Stream, which separates cooler continental shelf water from warmer Sargasso water is an example of a large-scale front. Within mesoscale eddy systems, convergences may occur which steepen the horizontal density gradients leading to frontogenesis. Such fronts exist on length scales of few kilometres across the front and tens of kilometres along it. Fronts of this nature can develop instabilities along their length which finally lead to their break-up. Fronts are also found in the shallow seas (shallow sea fronts), formed in continental seas and estuaries, and around islands, banks, capes and shoals. These are commonly located in boundary regions between shallow wind and tidally mixed nearshore waters and stratified, deeper, offshore waters (Simpson *et al.*, 1977; Pingree *et al.*, 1974).

The study of fronts is important in ocean dynamics since they are regions where vertical advection and the exchange of momentum and other properties are locally intense. Large scale ocean fronts are important in air-sea interaction effects on the weather and climate. Oceanic fronts also have significant biological consequences. Frontal zones are regions of strong convergence of surface currents and relatively strong vertical motions. Upwelling in fronts can advect nutrients into the euphotic zone, and they are generally areas of high productivity for all the food chain from phytoplankton through fish and marine mammals. They are therefore regions that have been exploited heavily by fishermen. A clear understanding of the biological role of fronts is needed to construct general models of ocean productivity. The location of persistent nearshore frontal zones must be considered in the design of waste water discharge outfalls including those of municipal, industrial, radioactive and power plant effluents into the marine environment if we are to avoid excessive concentration and contamination of the shoreline. Frontal circulation affects the dispersion of oil spills and ocean dumped contaminants. Thus the study of coastal fronts must be incorporated into environmental monitoring and sampling design if we are to determine how pollutants are transported, concentrated and incorporated into marine food chain.

NOAA-AVHRR infrared images have been widely used for number of years to monitor and extract information on the general characteristics of oceanographic features such as fronts, meanders and eddies. Using NOAA-AVHRR infrared imagery, Apel (1980)

studied the evolution of meanders in the Gulf Stream east of Cape Hatteras. Richardson (1980) used NOAA images to draw the path of the Gulf Stream and of rings separated from the stream. Churchill and Cornillon (1991), using NOAA images and hydrographic data, traced a subtropical water mass crossing the stream and estimated its influence on the slope water north of the stream. Lee *et al.*, (1991) have used AVHRR imagery to study the meanders and eddies of Gulf Stream and the influence of the frontal eddy on the productivity of the Southeast U.S continental shelf. Kimura and Sugimoto (1993) observed that small amplitude meanders in the Kurushio develop into a large meander using AVHRR images. AVHRR images have been used to detect fronts, meanders and eddies in a variety of other currents including; e.g., the California Current by Randerson and Simpson (1993), Iceland-Faeroe front by Niiler *et al.*, (1992), East Greenland Current by Wadhams (1981) and Bruce (1995), Labrador current meanders by LeBlond (1982) and Ikeda (1987), and the coastal current in the Black sea by Oguz (1992) and Sur *et al.*, (1996).

3.2.2 Sea surface temperature

The measurement of sea surface temperature (SST) from space using AVHRR is the technique of marine remote sensing which has had the greatest impact in oceanography. SST is now considered as one of the main controllers and indicators of climate variability. The surface temperature of the ocean together with the air temperature regulates the transfer of long-wave radiant energy to the atmosphere as well as the latent and sensible

heat fluxes into the lower atmosphere thus playing an important part on the influence of the oceans on the atmosphere. The temperature of the uppermost layer of the ocean determines the heat content there and affects its biological activity. Early global data sets of SST were generated from ship measurements using bucket and engine intake thermometers, and the accuracy and coverage of these data sets are extremely poor. The maps of ship coverage for three decades (1951-1980) given by Bottomley et al., (1990) show no data in the southeast Pacific and the Southern ocean and limited data in the tropical Pacific. Recent high-quality measurements from drifting and moored buoys and better quality control of ship data have improved the data sets generated, but there are still many data voids in area not covered by shipping lanes. Over the last two decades the use of satellite data to provide global SST data sets has been gradually increasing, and these are now thought to be better than those derived from a combination of conventional *in situ* measurements (Barton, 1995).

In the past, geostationary satellites such as Meteosat, GOES, GMS, INSAT included a single thermal infrared channel for SST measurement which provided rough estimates of surface temperature. A great advance in the measurement of SST was made with the launch of the first AVHRR instrument on the polar orbiting TIROS-N satellite. This first instrument had an extra channel at $3.7 \mu\text{m}$ and thus allowed for a differential absorption technique to be used to derive a correction for water vapour absorption in the atmosphere.

Use of this technique was restricted to night time, as the short-wavelength channel included significant reflected solar contribution during the day. Later, five-channel AVHRR instruments on the NOAA meteorological satellites included the so-called "split-window" channels at $10.8 \mu\text{m}$ and $11.9 \mu\text{m}$, allowing SST determination during the day. These two channels have been used for SST determination over the last 15 years. The inclusion of split window channels centered near 11 and $12 \mu\text{m}$ in geostationary satellites makes it possible to use the techniques developed for AVHRR data to extract SST. The latest advance in the satellite measurement of SST is the launch of Along Track Scanning Radiometer (ATSR) on the European Remote Sensing (ERS-1,2) satellite (Barton, 1995). This instrument, specifically designed to measure SST, has state-of-the-art calibration techniques and low noise signals on the detectors. The extra advantage in this instrument is the dual-view scanning system that allows atmospheric correction using two different pathlengths as well as a multiwavelength capability. Global data sets of SST estimated from ATSR data are now being used by the research community in climate applications.

3.2.3 Ocean currents

Ocean surface currents play an important role in a number of ocean related activities such as containment of oil and toxic chemical spills, optimal ship routing, search and rescue operations, and the management and exploitation of living and non-living resources. The estimation of ocean surface currents using conventional *in-situ* measurement from

ships and drifters can only be made from one point at any particular time, and such measurements are expensive and time consuming. Because of limitations in the estimation of surface currents using conventional measurement techniques, remote sensing methods such as satellite feature tracking from sequential NOAA-AVHRR infrared images are now being used more extensively to obtain information on the ocean surface circulation. Remote sensing methods have a great advantage over ordinary velocity measurements taken by ships and drifters as they give a synoptic view of the velocity distribution over a large area of the ocean. The computation of sea surface velocities using the satellite feature tracking method is accomplished by measuring the displacements of selected surface thermal features in a time sequence of thermal infrared images that have been spatially aligned or coregistered. There are two methods for computing sea surface velocities from sequential satellite images. The so-called the subjective method uses displacements of visually identified surface thermal features (La Violette 1984; Vastano and Borders 1984; Vastano and Reid 1985; Cracknell and Huang 1988; Vastano *et al.*, 1985; Svejkovsky 1988a) to determine the movement of the thermal features. This method requires subjective selection and tracking of surface thermal features in the images, and is operator-dependent. The other method, called the objective method (maximum cross-correlation method) uses the cross correlations between the sequential images to compute surface velocities (Emery *et al.*, 1986, 1992; Wahl and Simpson 1990). The objective method is computationally intensive, and is not well suited for the detection and measurement of rotational motion

and motion along the surface front. Both subjective and objective methods are also limited by features undergoing deformation. Recently, an artificial neural network method (Côté and Tatnall 1995b) has been developed. This technique appears to provide superior performance to existing techniques for satellite feature tracking and is being used for sea surface thermal fronts tracking from sequential NOAA-AVHRR infrared images. The primary advantages of this method are its speed, low sensitivity to deformation, and its capacity to detect rotational motion.

3.2.4 Fisheries

Satellite remote sensing data have been used to assist commercial and sports fishermen in harvesting fish from the sea, to provide marine resource managers with information useful for assessing the survival of fish eggs and larvae to the juvenile stage within a given year class, and to provide indications of the onset of major interannual events (e.g. ENSO and associated midlatitude warming events) which can have potentially devastating effect on a local fishery (Svejkovsky 1988b; Peláez and McGowan, 1986; Simpson, 1987; Fielder, 1984). Sea surface temperature (SST) fields retrieved from NOAA-AVHRR infrared imagery have proven to be an important source of information to marine and fishery research for the management of fishing strategies in different areas of the world. Surface thermal fronts, mesoscale eddies and coastal upwelling processes (Vaughan and Downey 1988) which determine the availability, distribution and catchability of fishes that congregate in nutrient-rich waters in the vicinity of thermal fronts can be detected in real

time for fishing management through the surface manifestation of SST fields (Sund *et al.*, 1981; Maul *et al.*, 1984; Laurs *et al.*, 1984; Fiedler and Bernard, 1987; Ramos *et al.*, 1992). SST, ocean colour, and plant pigment front boundaries determined from NOAA-AVHRR and Coastal Zone Colour Scanner (CZCS) have been used in combination with estimates of SST using airborne infrared thermometers and optical spectrometer measurements to establish relationships between the distribution of tuna, sword fish and salmon fishing effort and oceanic environmental variability off western Canada (Borstad *et al.*, 1982). Aerial photographic surveys have been used successfully to estimate the number of fishes in schools for inshore herring (Messieh and Mcpherson, 1980), herring (Messieh, 1984), lobster (Canon and Maynard, 1983), and caplin (Nakashima *et al.*, 1989). Also AVHRR, CZCS, and wind field data have been used in combination to help locate commercial catches of tuna, swordfish, and salmon off the west coast of the United States (Montgomery *et al.*, 1986). Future efforts in fisheries are likely to be directed towards using ocean colour data and plant pigment concentrations retrieved from Sea-viewing Wide Field-of-view Sensor (SeaWiFS) in combination with SST fields estimated from NOAA-AVHRR data. For more details on the use of satellite remote sensing in fisheries one can refer to the article by Simpson (1994), which discusses the potential benefits that can be gained from the increased use of remote sensing in operational fisheries oceanography.

Chapter 4

The NOAA-AVHRR Image analysis

The Advanced Very High Resolution Radiometer (AVHRR) onboard NOAA polar-orbiting satellites measures radiation at visible/infrared wavelengths and transmits this information to ground-based satellite data receiving stations. The raw telemetry data acquired at these receiving stations has little resemblance to the contrast enhanced thermal infrared images and sea surface temperature (SST) maps that can be used to detect, monitor and extract spatial and temporal characteristics of thermal features such as fronts, meanders and eddies in the ocean. Several processing steps are required to convert the raw images to extract meaningful information related to oceanography. Since 1994 roughly four daily passes of NOAA-AVHRR data have been acquired each day at the Northwest Atlantic Fisheries Centre (NWAFC) satellite receiving station, St. John's, Newfoundland, Canada. The field of view of the NWAFC satellite receiving station covers all coastal and shelf waters of Newfoundland, Labrador and a large part of West/East Greenland. In this chapter, the details of NOAA-AVHRR satellite system, the characteristics of AVHRR and the various processing steps for AVHRR data collected at the NWAFC satellite laboratory are described. The processed images will then be used to study the spatial and

temporal characteristics of surface thermal features in the West Greenland Current.

4.1 The TIROS/NOAA Satellites and AVHRR characteristics

Since the end of 1970's, the advanced TIROS-N satellites of the National Oceanic Atmospheric Administration (NOAA), USA, which are labelled NOAA- A,-B, etc., before launch and NOAA- 6,-7, etc., after successful launch have been orbiting the earth. They provide operational coverage of the entire earth four times per day by using two satellites (at present NOAA-12 and NOAA-14). The NOAA satellite is 4.2 m long, 1.9 m in diameter, and carries a 2.4×4.9 m solar array for power (Cotter, 1990; Scwalb, 1990). The satellites were designed to operate in a near-polar, sun-synchronous orbit (the satellite will cross the equator at the same local time every day). The orbital period is about 102 min, which produces 14.1 orbits per day. Two nominal altitudes roughly between 800-900 km, have been chosen to permit concurrent operation of two satellites. The local solar time (LST) of equator crossing is usually 1400h or 1930h for ascending node and 0200h or 0730h for descending node. The instrument systems on the TIROS/NOAA satellites include: TIROS Operational Vertical Sounder (TOVS), ARGOS Data Collection and Platform Location System (DCLS), Space Environment Monitor (SEM), Search and Rescue System (SARSAT), Advanced Very High Resolution Radiometer (AVHRR). TOVS, a subsystem consisting of High-resolution Infrared Radiation Sounder (HIRS/2), Microwave Sounding Unit (MSU) and Stratospheric Sounding Unit (SSU) instruments provide temperature profiles of the atmosphere from sea level to 20 miles, water vapour

content, total ozone content and temperature profiles of the stratosphere. The DCLS, often referred to as the ARGOS data collection and location system onboard the NOAA satellites provides a means of collecting environmental data (e.g., temperature and pressure etc.) from instruments situated in difficult or inaccessible locations on the land or sea surface and for locating the position of fixed or moving platforms (e.g., buoys and icebergs). Platforms such as buoys, balloons, fixed or floating stations are equipped with a Platform Transmitter Terminal (PTT), which transmits data at a particular frequency to the satellite. At any given time one of the NOAA satellites can receive messages from platforms within a circle of diameter about 5000 km on the ground. The data acquired by DCLS are then transmitted to the satellite data receiving ground stations. Therefore, a user who has a satellite receiving ground station for receiving NOAA-AVHRR data may also receive the raw ARGOS data directly in real time from any platform that transmits while the satellite is above the horizon of the receiving station. The SEM, a three instrument multidetector unit is used to monitor solar particulate energies in the vicinity of the satellite.

The AVHRR is a five channel radiometer sensitive to visible, near infrared and infrared portion of the electromagnetic spectrum. Table. 4.1 lists its spectral characteristics and the primary uses of AVHRR, and Table. 4.2 provides a listing of the basic AVHRR parameters (Scwalb 1978, 1990). The average instantaneous field-of-view (IFOV) of 1.3 milliradians yields a ground resolution of approximately 1.1 km at the satellite nadir

Table 4.1: Spectral characteristics and primary uses of AVHRR.

Channel No.	Wavelength (μm)	Primary Uses
1	0.58 - 0.68	Daytime cloud/surface mapping
2	0.725 - 1.10	Surface water delineation, ice and snow melt
3	3.55 - 3.93	Sea surface temperature, night-time cloud mapping
4	10.3 - 11.3	Sea surface temperature, day and night-time cloud mapping
5	11.5 - 12.5	Sea surface temperature, day and night-time cloud mapping

from the nominal orbit altitude of about 850 km. The width of off-nadir pixels increases from 1.1 km to about 5 km at the most extreme viewing angle (i.e. at the edge of the 3000 km imaging swath). The maximum scan angle is 55.4° , and the sensitivity of thermal IR channels is 0.12 deg at 300 K. AVHRR data are transmitted in real time to both Automatic Picture Transmission (APT) and High-Resolution Picture Transmission (HRPT) users. The APT system transmits data from any two of the AVHRR channels and has a reduced resolution, typically by about a factor of 4 compared with HRPT data. The HRPT system transmits data from all AVHRR channels. The data consists of 10 bit/pixel and the transmission rate to the receiving satellite station is 665 Kbps (kilo bits per second), and its format can be found in the technical report by Lauritson *et al.*, (1979).

Table 4.2: The basic characteristics of AVHRR.

Parameters	Characteristics
Instantaneous field of view (IFOV)	1.3 mrad(\sim 1.1 km on the ground)
Sensitivity of thermal IR channels 3,4,5	0.12 deg K at 300 K
Scanning angle	-55.4° to $+55.4^\circ$ (\sim 2900 km on the ground)
Calibration	Visible, near IR: no calibration Thermal IR: deep space, blackbody
No. of digitisation levels	1024 (10-bit/pixel)

4.2 NOAA-AVHRR data processing

The AVHRR onboard the NOAA satellites measures radiation at spectral bands listed in Table. 4.1 and transmits this information in sequential form to ground based receiving stations. The various steps followed in processing the NOAA-AVHRR data are shown in Fig. 4.1. The first step in the AVHRR data processing is the detection of missing and corrupted scanlines in the raw data, and their replacement with blank scanlines.

4.2.1 Calibration of NOAA-AVHRR data

The second step in the NOAA-AVHRR data processing is radiometric calibration. AVHRR visible and near-infrared data (channels 1 and 2) may be converted to reflectance and the thermal infrared data (channels 3,4 and 5) may be converted to temperatures based

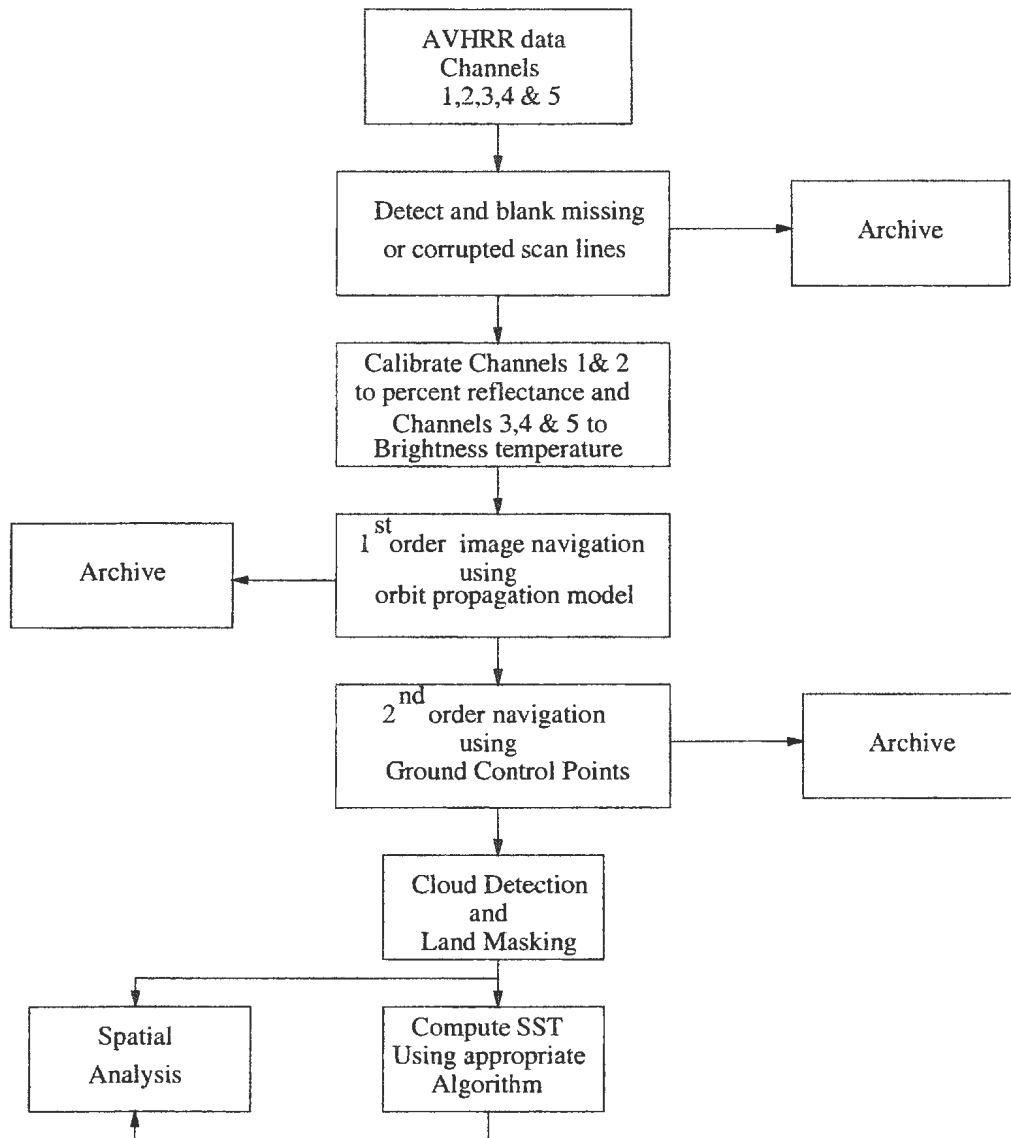


Figure 4.1: Processing steps for NOAA-AVHRR data collected at NWAFC satellite laboratory.

on calibration coefficients (NOAA, 1990). The calibration coefficients, consisting of slope and intercept values of the five channels must be appropriately scaled, and then are used to calibrate the AVHRR data. In this section, the calibration procedure of thermal infrared data is described and for the visual data calibration (which is very similar to the thermal procedure) the reader can refer NOAA (1990).

The scaled thermal channel slope values are in units of $\text{mW}/(\text{m}^2\text{-sr-cm}^{-1})$ per count and the intercept is in $\text{mW}/(\text{m}^2\text{-sr-cm}^{-1})$ (NOAA, 1990). The radiant energy measured by the sensor (channel i) is computed as a linear function of the input data values as follows:

$$E_i = S_i C + I_i \quad (4.1)$$

where E_i is the radiance value in $\text{mW}/(\text{m}^2\text{-sr-cm}^{-1})$, C is the input data value (ranging from 0 to 1023 counts), and S_i and I_i are respectively the scaled slope and intercept values. The equation to convert the digital numbers to their brightness temperature (temperature derived from measured radiances by inverting the Planck function) is

$$T_b(E) = C_2 \nu / [\ln(1 + C_1 \nu^3 / E)] \quad (4.2)$$

where T_b is the brightness temperature (K) for the radiance value E , ν is the central wave number of the channel (cm^{-1}), and C_1 and C_2 are constants ($C_1 = 1.1910659 \times 10^{-5} \text{ mW}/(\text{m}^2\text{-sr-cm}^{-4})$ and $C_2 = 1.438833 \text{ cm-K}$). Note that the temperatures obtained by this procedure are not corrected for atmospheric attenuation. The central wave number

(ν in Eqn. 4.2) values for channels 3,4 and 5 as a function of temperature for each NOAA satellite are provided in NOAA Polar Orbiter Data users guide (NOAA, 1990). In this study, instead of using the values given in the table, the central wave number is calculated to fit the temperature range to a linear equation and the newly computed value is used in Eqn. 4.2.

4.2.2 AVHRR image navigation

The image data from polar orbiting satellites such as NOAA, with a large swath, have distortions due to earth shape, earth rotation, variations in satellite orbit and satellite attitude (roll, pitch and yaw), and requires geometric correction to achieve a reasonable locational accuracy. There are essentially two different approaches to the problem of AVHRR image navigation. The first method assumes no orbital information, and relies on known geographic features clearly visible in the images, called the ground control points (GCPs), to correct for errors in earth shape, scan geometry, satellite orbit, and satellite attitude. The second method uses high quality satellite ephemeris data (orbital parameters) to locate the satellite as a function of time and only requires GCPs to correct for possible satellite attitude and timing (timing at the ground station where the data are collected and/or on the satellite that is transmitting the data) errors. A comprehensive review of the navigation of imagery from AVHRR is provided by Emery *et al.*, (1989). Recently, Rosborough *et al.*, (1994) have presented a systemized approach to highly accurate, or precise AVHRR image registration. The navigation system developed

by Rosborough *et al.*, (1994) is capable of producing images in either satellite perspective (forward navigation method) or registered to a specified geographic projection (indirect navigation method). In the forward navigation method, a map database (latitude, longitude position on the earth) is resampled to fit the satellite projection dictated by the satellite orbit and attitude. Since the forward navigation method excludes the possibility of comparing a sequence of images, the indirect navigation method, whereby the image is resampled to fit a preselected map projection of the target area, became more attractive. Both navigation methods require detailed orbital models for determining the satellite position, velocity and attitude with respect to an earth-fixed coordinate system. In the present study, a two step procedure for the navigation of AVHRR images acquired at the NWAFC satellite laboratory is used. First, the indirect navigation algorithm presented by Rosborough *et al.*, (1994) is used to correct for geometric distortions due to earth shape/rotation and satellite orbit variations (1st order navigation). Next, the errors due to satellite attitude and timing are corrected using GCPs (visible landmarks)(2nd order navigation). The geometry of the AVHRR sensor and the NOAA polar orbiting satellite, details of the orbital model, the indirect navigation algorithm and application of the two step procedure for navigating an image acquired at NWAFC satellite laboratory will now be discussed in detail.

(i) AVHRR scan geometry and orbit model

The NOAA polar orbiting satellites that carry the AVHRR sensor are deployed in nearly polar sun-synchronous orbits at altitudes ~ 850 km. The NOAA series satellites are three-axis stabilized and attempt to maintain a certain reference attitude at all times. This reference attitude corresponds to one axis pointing to nadir and another axis being maintained perpendicular to the inertial velocity vector of the satellite. AVHRR scans in the plane defined by these two axes. The orbital and scanning geometry of the NOAA satellites is shown in Fig 4.2 (labelled satellite position at time t). Let the position of the satellite be denoted by \vec{r} in an earth-fixed coordinate system and denote the surface location being imaged by \vec{R} in the same system. Then a position vector from the satellite to the surface is

$$\vec{d} = \vec{R} - \vec{r}. \quad (4.3)$$

The position vector (\vec{d}) is referred to as the look vector which can be thought of as the line-of-sight of the AVHRR. In the indirect navigation method, the surface position vector (\vec{R}) is specified, and the problem is to determine the satellite position (\vec{r}) such that the look vector (\vec{d}) lies in the scanning plane defined above. Once the location is determined, the look vector is known and the corresponding AVHRR image pixel is specified. To implement this geometric approach, it is necessary to provide detailed models for satellite position at any specific time with respect to the earth-fixed coordinate system. The position and velocity of the satellite at any specific time are determined from

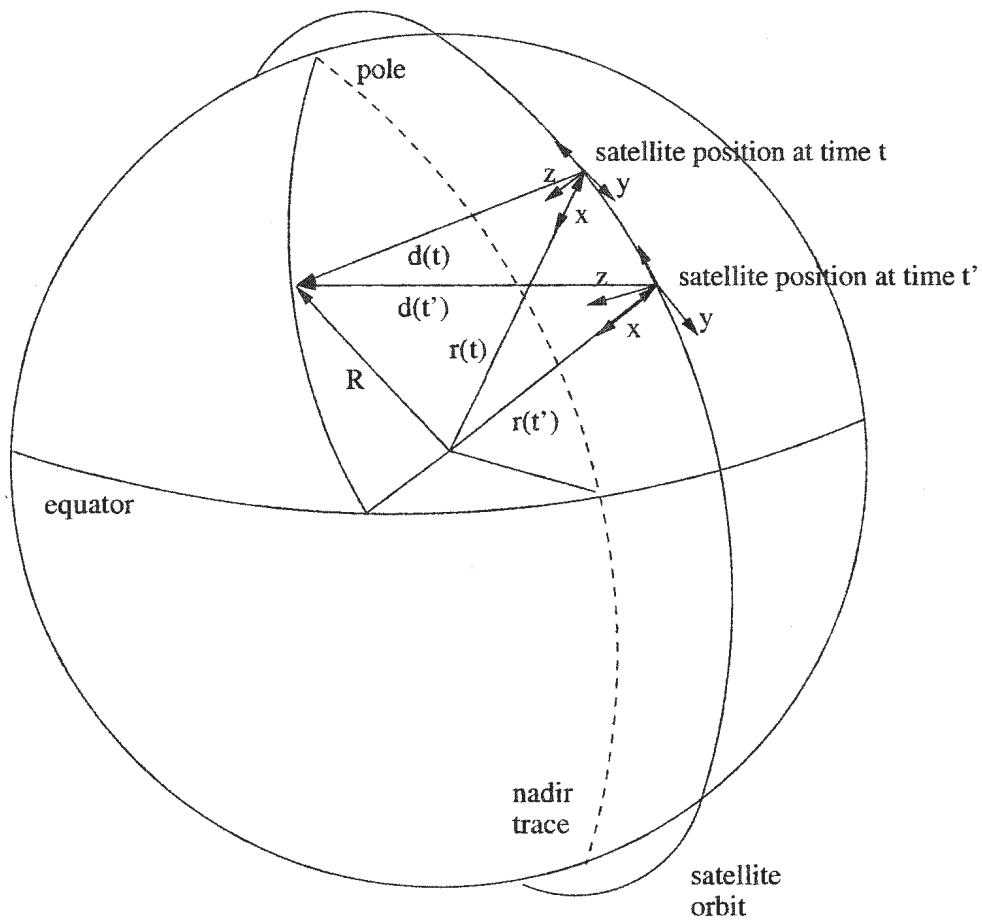


Figure 4.2: Orbital and scanning geometry at solution time t and intermediate time t' for indirect navigation.

the available ephemeris data (orbital parameters such as orbit number, semimajor axis, inclination and eccentricity etc.). The satellite ephemeris data generated by the North American Aerospace Defense Command (NORAD) are obtained from the Celestial World Wide Web (WWW) site (<http://celestrak.com>) where it is published and maintained. It is possible to obtain the position and velocity of the satellite at any specified time by interpolating the highly accurate satellite ephemeris data, if they are available at closely spaced times. If they are widely spaced (which is usually the case), then it is necessary to use an orbital model to determine the position and velocity at any intermediate time. In the following paragraphs, a general description of the orbital model that includes the features of the models used for the most commonly available ephemeris data is provided.

The orbital model is essentially a set of differential equations for the orbital elements (Kepler orbital elements) which describe the orbit. The orbital elements consist of the semimajor axis (a), eccentricity (e), inclination (i), argument of perigee (ω), longitude of the ascending node (Ω), and mean anomaly (M). A near-earth satellite can be thought of as having two types of orbital motion, the first being the long-term evolution of the orbit and the second being short-term variations superimposed on the long-term motion. The long-term motion is typically characterized by the mean orbital elements (Kepler orbital elements). If the orbital motion was that of an ideal two-body system, then the orbital elements would remain constant in time except for a mean anomaly, which would vary linearly in time. But, in reality the mean orbital elements of a near-earth satellite change

slowly in time, for example the semimajor axis and eccentricity vary approximately linearly in time due to atmospheric drag. The argument of perigee and the longitude of the ascending node vary linearly in time due to the earth oblateness, and they have a small quadratic variation in time due to the indirect effect of the changing semimajor axis. The inclination remains constant, and the mean anomaly has an additional linear variation in time due to earth oblateness, as well as an additional small quadratic variation due to the changing semimajor axis. The other forcing mechanisms such as earth and ocean tides, lunisolar effects, and solar radiation pressure produce negligible perturbations for most orbits (Straka *et al.*, 1989). Given the mean orbital elements at a particular time, the mean elements at a later or earlier time can be obtained using the relations of the form

$$\bar{a} = \bar{a}_0 + \dot{a}\Delta t \quad (4.4)$$

$$\bar{e} = \bar{e}_0 + \dot{e}\Delta t \quad (4.5)$$

$$\bar{i} = \bar{i}_0 \quad (4.6)$$

$$\bar{\omega} = \bar{\omega}_0 + \dot{\omega}\Delta t + \ddot{\omega}\Delta t^2 \quad (4.7)$$

$$\bar{\Omega} = \bar{\Omega}_0 + \dot{\Omega}\Delta t + \ddot{\Omega}\Delta t^2 - \omega_e\Delta t \quad (4.8)$$

$$\bar{M} = \bar{M}_0 + \dot{M}\Delta t + \ddot{M}\Delta t^2 \quad (4.9)$$

where Δt is the elapsed time from or until the reference time. The overbars indicate mean orbital elements and the zero subscript indicates the mean orbital elements at a particular time. In the computation of Ω , the earth rotation rate ω_e is applied so that the longitude of the ascending node is obtained. The mean orbital elements at the reference time and the rate of change of orbital elements are obtained from the ephemeris data. After obtaining the mean orbital elements at the desired time, the short period variations can be added to obtain the final osculating elements. The largest short period variations in the elements comes from the oblateness of the earth. Though the higher degree harmonics of the earth's gravity field produce substantial variations (Kaula, 1966), the commonly used formulation by Brouwer (1959) provides the dominant effects that need to be taken into account. Given the mean orbital elements, the short period variations (Δa , Δe , Δi , $\Delta \omega$, $\Delta \Omega$, and ΔM) can be directly computed, and the osculating orbital elements are then given by

$$a = \bar{a} + \Delta a \quad (4.10)$$

$$e = \bar{e} + \Delta e \quad (4.11)$$

$$i = \bar{i} + \Delta i \quad (4.12)$$

$$\omega = \bar{\omega} + \Delta \omega \quad (4.13)$$

$$\Omega = \bar{\Omega} + \Delta \Omega \quad (4.14)$$

$$M = \bar{M} + \Delta M. \quad (4.15)$$

Finally, the orbital elements are converted to satellite position and velocity in an earth-fixed coordinate system, which are then used in the indirect navigation algorithm. The accuracy of the osculating orbital elements depend on the accuracy of the orbital model used, as well as the accuracy of the original orbit determination that was performed using the satellite tracking data. In the present study, the orbital propagation model (SGP4) is used, and for a detailed description of the model the reader can refer to Spacetrack Report No. 3 (Hoots and Roehrich 1980).

(ii) Indirect Navigation Algorithm

Indirect navigation is the process that maps the geographic point (latitude and longitude position) on the earth to the satellite field of view which contains that point as compared to direct navigation which maps the field of view of the satellite to a latitude, longitude position on earth. The procedure for navigating an image using indirect navigation method begins with the specification of parameters such as the size, geographic projection and resolution that define the geometry of the image and assign earth locations to each image pixel. The indirect navigation algorithm is then used to map each image pixel to the appropriate measurement in the satellite data, thus combining georegistration and resampling in one step. The physical description of the indirect navigation algorithm follows.

The satellite orbital and scan geometry for indirect navigation is depicted in Fig 4.2.

The look vector \vec{d} from the satellite to the surface is given by

$$\vec{d} = \vec{R} - \vec{r} \quad (4.16)$$

where all quantities are assumed to be expressed in earth-fixed coordinate system. The surface position vector \vec{R} is specified in the indirect navigation method and the problem is to determine the satellite position (\vec{r}) when this point was imaged. Determining the satellite location effectively then specifies the pixel corresponding to the surface location (the satellite orbital location will specify the scan line and the look vector will specify the scan angle). It is important to note that since the location of the satellite is unknown, so too is the time when the point in consideration was sampled.

To express the look vector \vec{d}_b in the satellite-fixed coordinate system (X_b, Y_b, Z_b), the transformation from satellite-geodetic coordinate system to satellite-fixed system has to be carried out. Consider a coordinate system fixed to the satellite (X_b, Y_b, Z_b). These axes, respectively, correspond to the x,y and z axes of Fig 4.2 for the satellite position at time t. This system differs from the satellite-geodetic (satellite-centered geodetic reference frame) system (X_g, Y_g, Z_g) by small angles in all three axes. The transformation from the satellite-geodetic system to satellite-fixed system is carried out by three successive rotations. The first rotation is a rotation about the x-axis (yaw) and the angle of rotation is defined as ξ_y . A rotation is then made about new y-axis (roll) and is denoted by ξ_r . Finally, a rotation is made about the new z-axis (pitch), and is

denoted by ξ_p . All three rotation angles are measured in a positive sense with respect to the right-hand rule.

Let \vec{d}_g be a vector defined in the satellite-geodetic system. This vector represented in the satellite-fixed system \vec{d}_b is then given by

$$\vec{d}_b = A\vec{d}_g \quad (4.17)$$

where A is the attitude rotation matrix. This 3×3 attitude rotation matrix (Wertz, 1978) is given by

$$A = \begin{vmatrix} \cos \xi_p \cos \xi_r & \cos \xi_p \sin \xi_r \sin \xi_y + \sin \xi_p \cos \xi_y & -\cos \xi_p \sin \xi_r \cos \xi_y + \sin \xi_p \sin \xi_y \\ -\sin \xi_p \cos \xi_r & -\sin \xi_p \sin \xi_r \sin \xi_y + \cos \xi_p \cos \xi_y & \sin \xi_p \sin \xi_r \cos \xi_y + \cos \xi_p \sin \xi_y \\ \sin \xi_r & -\cos \xi_r \sin \xi_y & \cos \xi_r \cos \xi_y \end{vmatrix}$$

where ξ_y , ξ_r and ξ_p are the yaw, roll and pitch angles respectively. Making small angle approximations, that is replacing $\cos \xi \approx 1$ and $\sin \xi \approx \xi$ so that the attitude rotation matrix becomes

$$A = \begin{vmatrix} 1 & \xi_p & -\xi_r \\ -\xi_p & 1 & \xi_y \\ \xi_r & -\xi_y & 1 \end{vmatrix}$$

If \vec{d} is a vector in the earth-fixed coordinate system, then this vector in the satellite-geodetic system is

$$\vec{d}_g = T\vec{d} \quad (4.18)$$

where 3×3 rotation matrix T is given by

$$T = \begin{vmatrix} \vec{w}_x^T \\ \vec{w}_y^T \\ \vec{w}_z^T \end{vmatrix}.$$

\vec{w}_x^T , \vec{w}_y^T and \vec{w}_z^T are the unit vectors of the satellite-geodetic coordinate system. Substituting Eqn. 4.18 in to Eqn. 4.17, the look vector in the satellite-fixed system becomes

$$\vec{d}_b = AT\vec{d}. \quad (4.19)$$

If the attitude matrix is not known or it has not been solved for, it is set to the identity matrix for the initial navigation. The satellite-fixed look vector can then be used to navigate the satellite. Since the instrument scans in the $X_b - Z_b$ plane, the look vector will lie in this plane if the satellite is correctly navigated. The angle that the look vector makes with the positive X_b axis is the scan angle. The corresponding vector geometry is illustrated in Fig 4.2 when the satellite is in the position defined at time t . An initial guess is made for the location of the satellite, based on either an approximate latitude of the sub-satellite point or an approximate time from equatorial crossing. From this, the satellite position and velocity vector are computed in the earth-fixed system. Then the look vector (satellite to surface vector) is computed and is rotated into satellite-fixed coordinate system using Eqn. 4.19. The resulting look vector will not (in all likelihood) lie in the scanning $X_b - Z_b$ plane. The projection of the look vector into the $X_b - Y_b$ plane (which corresponds very nearly with the orbital plane) relates to the amount that

the satellite is either ahead or behind of where it should be. If the Y_b component of the look vector is positive, then the satellite is ahead of the required location. The satellite location is corrected by this amount and the procedure is repeated until some desired level of convergence is achieved. The vector configuration for some intermediate step in the iteration can be seen in Fig 4.2 when the satellite is positioned at time t' .

Let the look vector in the satellite-fixed coordinate system be written as

$$\vec{d}_b = d_x \vec{v}_x + d_y \vec{v}_y + d_z \vec{v}_z \quad (4.20)$$

where \vec{v}_x , \vec{v}_y and \vec{v}_z are the unit vectors of the satellite fixed coordinate system. Then, the angle that the look vector projected onto the $X_b - Y_b$ plane makes with the positive X_b axis is

$$\beta = \tan^{-1}(d_y/d_x) \quad (4.21)$$

For a correctly navigated image, this angle will be zero. The orbital angle (true anomaly correction) that will correct this angle toward zero is

$$\Delta\nu = \tan^{-1}[d_{xy} \sin \beta / (r_s - d_{xy} \cos \beta)] \quad (4.22)$$

where d_{xy} is the projection of the look vector onto the $X_b - Y_b$ plane ($\sqrt{d_x^2 + d_y^2}$) and r_s is the geocentric distance to the satellite. This required change in true anomaly can be converted to an equivalent change in time by using the satellite's mean motion. The

satellite new position and velocity are then recomputed at this new time. The process is repeated until the look vector lies in the scanning plane. The convergence criterion simply needs to be sufficient to correctly identify the scan line. This is equivalent to determining the location of the satellite on the orbit better than $1/6$ s of time, which corresponds to approximately 1.2 km of distance along the orbit. After convergence, the scan angle will be specified by the angle of the look vector with respect to X_b axis ($\tan^{-1}(d_z/d_x)$) and the along-track position of the satellite will also be known. This along-track position will serve to specify the scan line number and the scan angle will specify the pixel within the line.

The steps involved in the indirect navigation algorithm are summarized as follows.

1. For a given surface location (latitude and longitude position) and an assumed satellite position, calculate the satellite to surface look vector in the earth-fixed coordinate system (Eqn. 4.16).
2. Rotate the look vector to the satellite-fixed coordinate system (including the attitude rotation matrix if available)(Eqn. 4.19).
3. Calculate how much the look vector lies out of the scanning plane (Eqn. 4.21).
4. Determine how much the satellite should be advanced or retarded along the orbit in order to move the look vector into the scanning plane (Eqn. 4.22).
5. Compute the satellite position and velocity at the new location and repeat these steps until the satellite location converges to some desired level.

(iii) Application of indirect navigation algorithm

As stated in the earlier section on indirect navigation algorithm, the procedure for creating an image begins with the specification of output size of the image, the geographic projection type (i.e Mercator, conic etc), a center latitude and longitude of the output image and the latitude range of the image (from north border to south border). Each pixel in the output image is mapped to a latitude and longitude, which are then input into the indirect navigation algorithm to calculate the corresponding scanline and sample in the satellite data. The resolution of the output image is determined by the combination of the latitude range and the image size in pixels. The maximum resolution will be used if the vertical and horizontal image size in pixels is roughly 100 times the latitude range in degrees. For example, if an image with vertical and horizontal size 1024X1024 was specified then a latitude range of 10 degrees will result in approximately 1.1 km between each image pixel, which is the maximum resolution of the AVHRR data.

Now, the two step procedure for the navigation of an unregistered NOAA-AVHRR raw image (Fig. 4.3) acquired at NWAFC satellite receiving station is described. The image selected is a HRPT NOAA-14 channel 4 image that shows the Greenland region collected on August 15, 1995 at 0545 UTC. In the first step, indirect navigation algorithm is used to correct for errors due to earth shape/rotation and satellite orbit variations (1st order navigation). To navigate the selected image using indirect method, the following parameters were chosen: The output image size (vertical and horizontal) 900 X 900

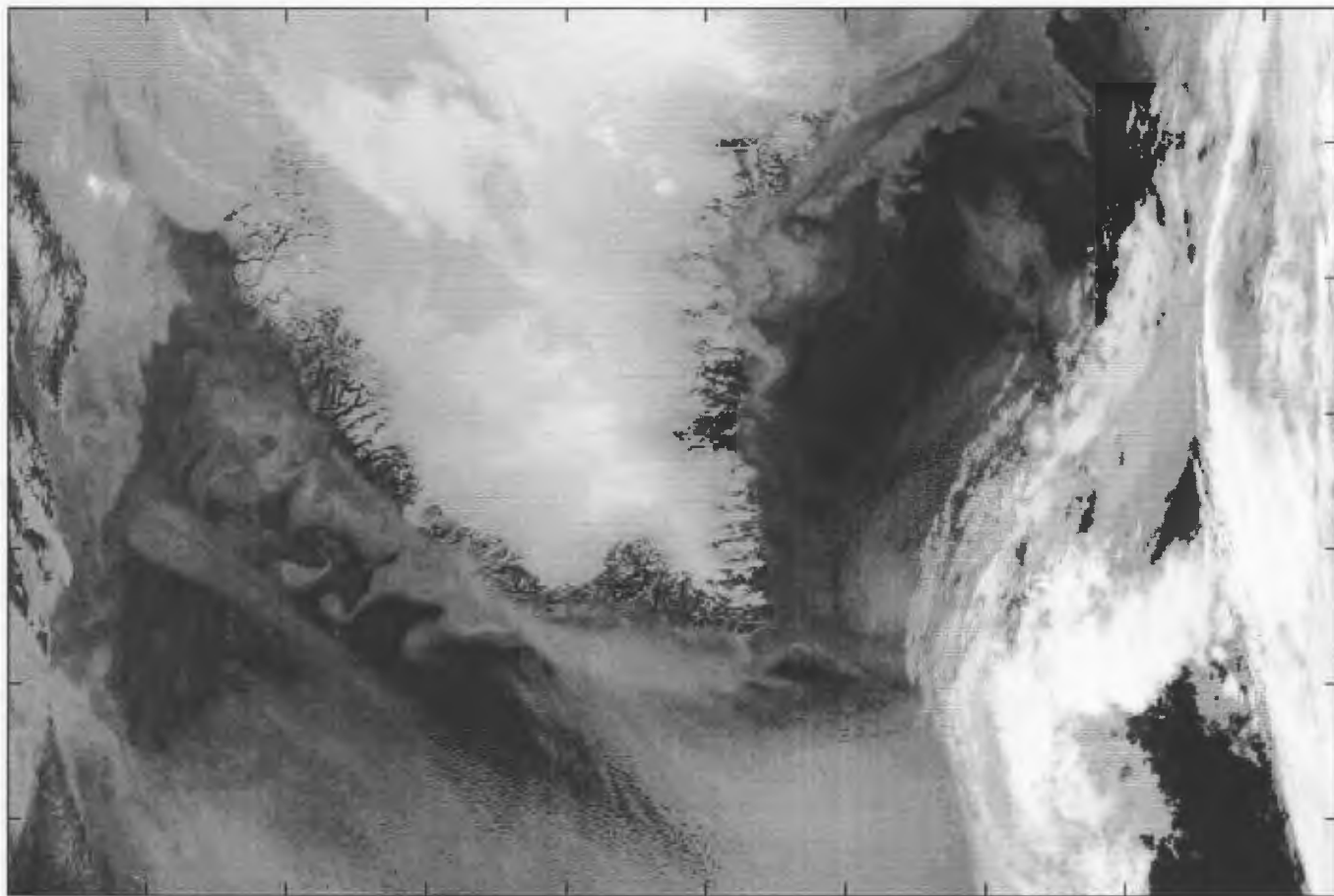


Figure 4.3: An unregistered raw image of Greenland region (Channel 4, NOAA-14, August 15, 1995, 0545 UTC).

pixel, center latitude and longitude (62° N, 52° W), Mercator geographic projection, and a latitude range (from north border to south border) of 10 degrees. A portion of the georegistered image that depicts the waters off the coast of West Greenland resulting from this first-step navigation is shown in Fig. 4.4. A geographic map overlay was created (Fig. 4.5) by coregistering a digital vector file (General Bathymetric Chart of the Oceans, GEBCO number 5.04) of the coastline of the West Greenland region with the navigated image using PCI image processing software. One can note the registration errors that are clearly displayed by the lack of correspondence between the navigated image and the coastline overlay map (Fig. 4.5). The offset of the image from the map overlay may be due to the errors caused by satellite attitude and timing. The second step is to correct these errors using ground control points (GCPs)(2^{nd} order navigation). We used the ground control points from the recognizable landmarks in the image and the corresponding landmarks of the map overlay. The Geometric Correction Program (GCP works module) of PCI image processing software was used to perform the 2^{nd} order navigation. The image resulting from this second step navigation is presented in Fig. 4.6.

4.2.3 Cloud detection and land masking

The greatest problem in using the AVHRR infrared images for the identification of sea surface thermal features and the estimation of sea surface temperature is the presence of liquid water in the atmosphere, in the form of clouds. Clouds absorb the sea surface signal completely and emits upward radiance which is a function of its own thermodynamic

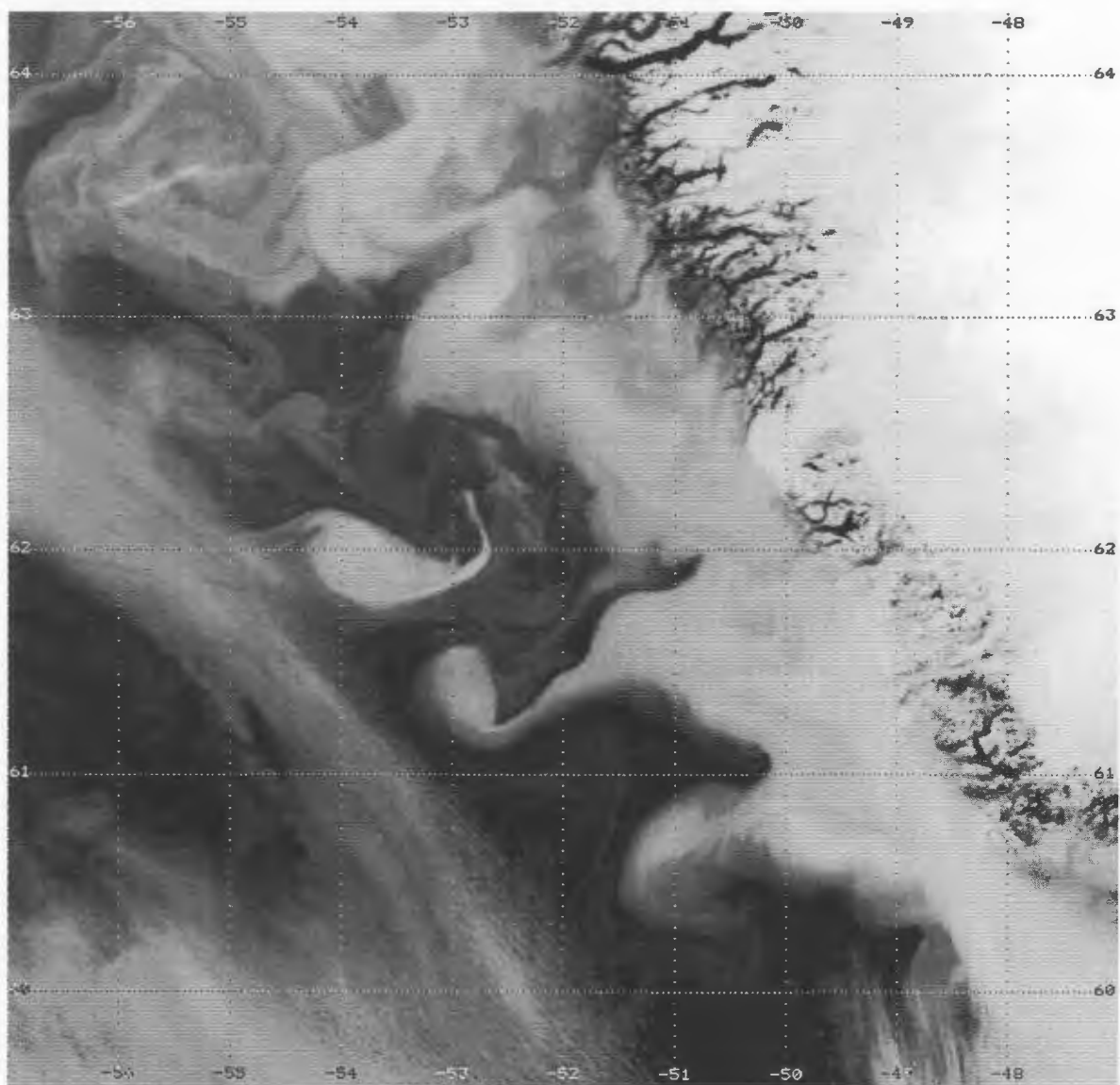


Figure 4.4: Georegistered NOAA-14 (Channel 4, August 15, 1995, 0545 UTC) image of West Greenland region created using indirect navigation method (1st order navigation).

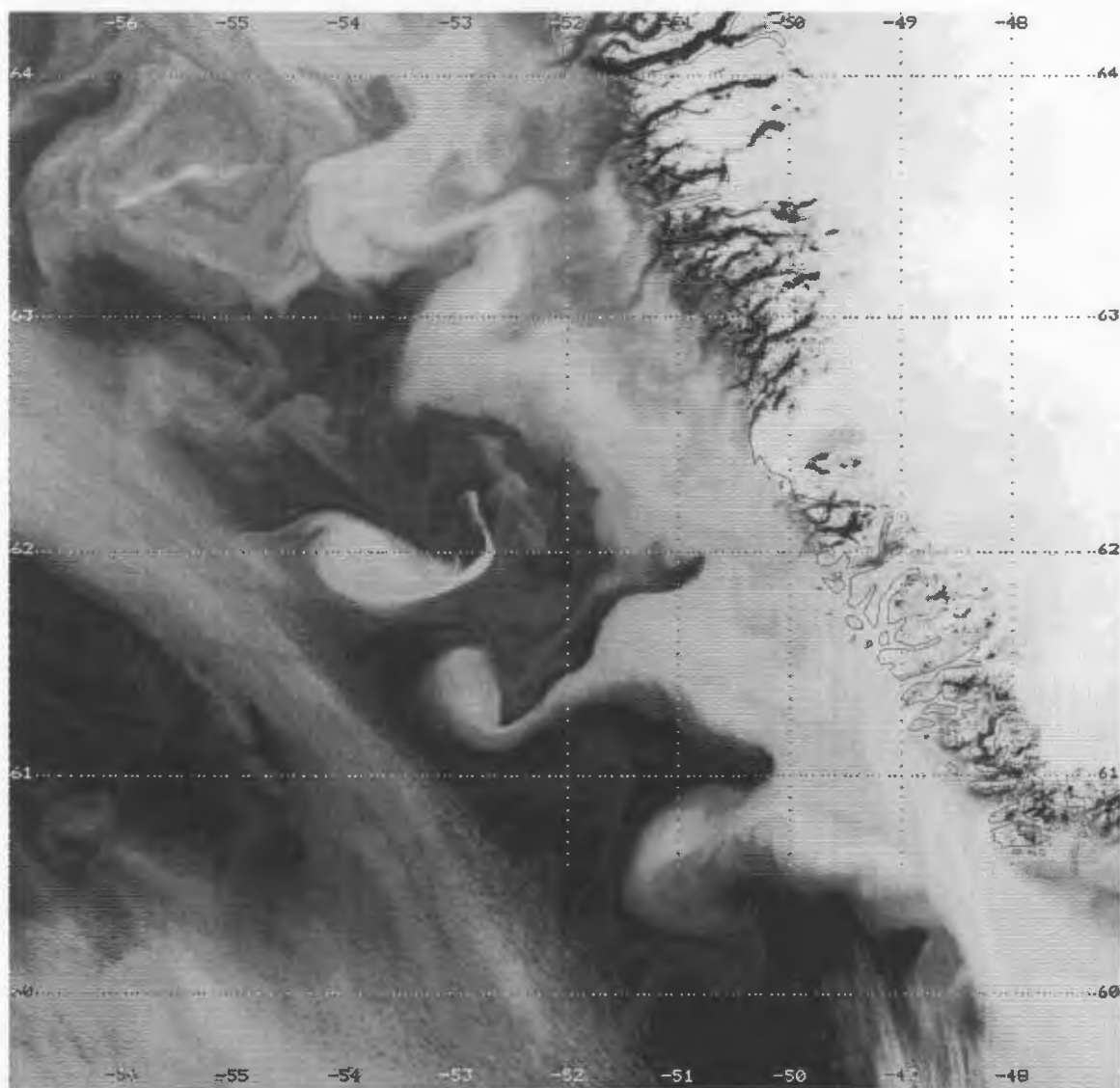


Figure 4.5: Georegistered NOAA-14 (Channel 4, August 15, 1995, 0545 UTC) image of West Greenland region with coastline map overlay.

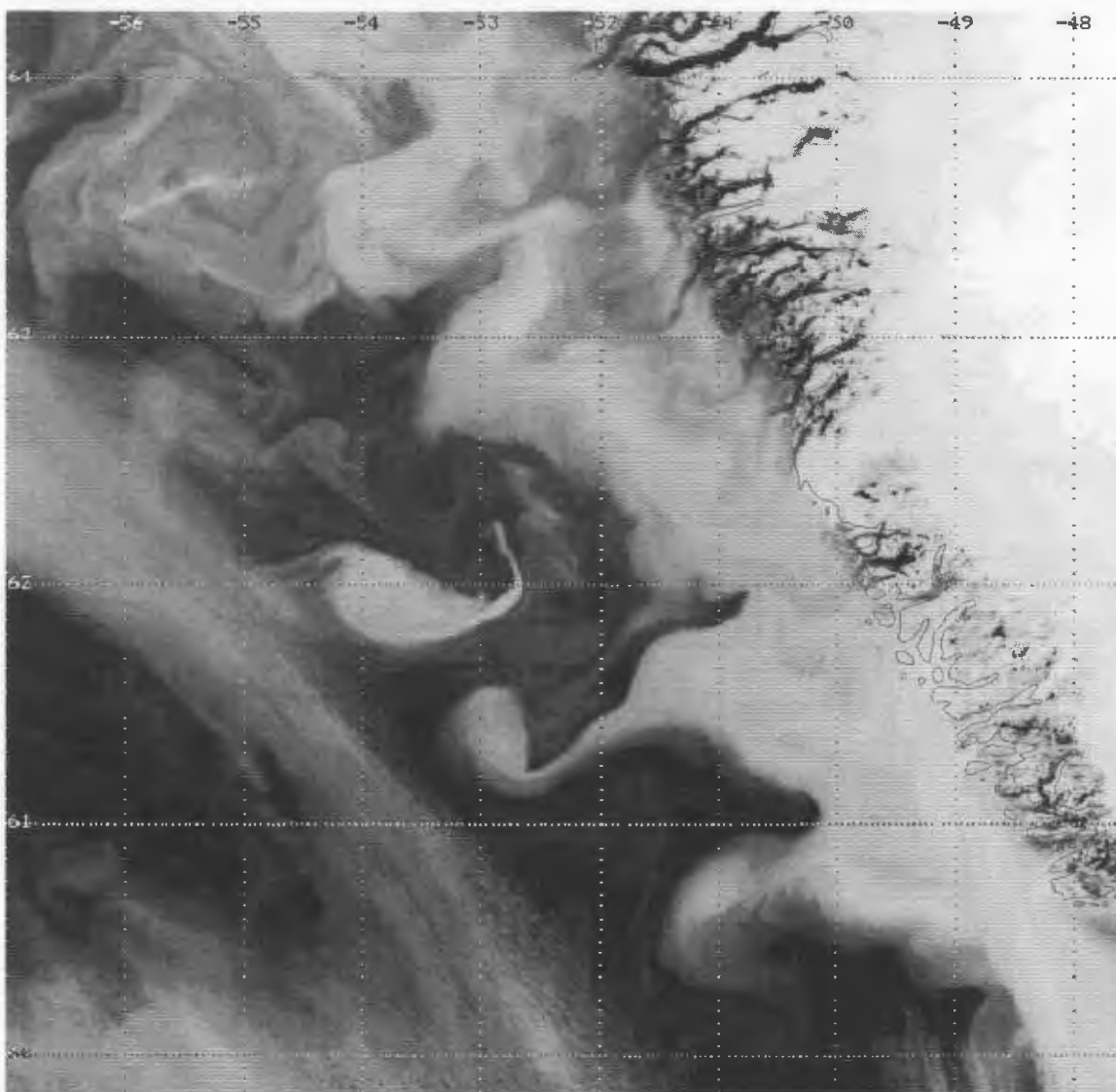


Figure 4.6: Georegistered NOAA-14 (Channel 4, August 15, 1995, 0545 UTC) image of West Greenland region with coastline map overlay (2^{nd} order navigation).

temperature and emissivity. In this study, the application of thermal infrared threshold is used for the detection of clouds. Clouds are identified by an algorithm which checks for radiance temperature values below some assigned threshold. This is based on the fact that there is a difference in temperature between the clouds and sea surface (clouds are generally colder than the sea surface) in thermal infrared channels. All pixels with brightness temperatures below a constant threshold of 270 K were considered to be cloud contaminated. After the detection of clouds, land masking was performed. This was carried out using a digital vector file of the coastline (GEBCO 5.04) of the West Greenland region. Polygons were created with the coastline file and then using PCI image processing software the land portion was masked out. Once the land mask was created, the overlay of bathymetry vectors (GEBCO 5.04) was carried out. Fig. 4.7 shows the image after the detection of clouds and land masking. After the detection of clouds and land masking the image can be used for spatial analysis of sea surface thermal features in the ocean and to compute sea surface temperature using appropriate algorithm. Barton (1995) provides a detailed review of the various algorithms used for deriving sea surface temperature from NOAA-AVHRR infrared data. Since, in this study, sea surface thermal features rather than absolute sea surface temperature are important, the infrared images that are selected and used for spatial analysis in the next chapter are not converted to temperature.

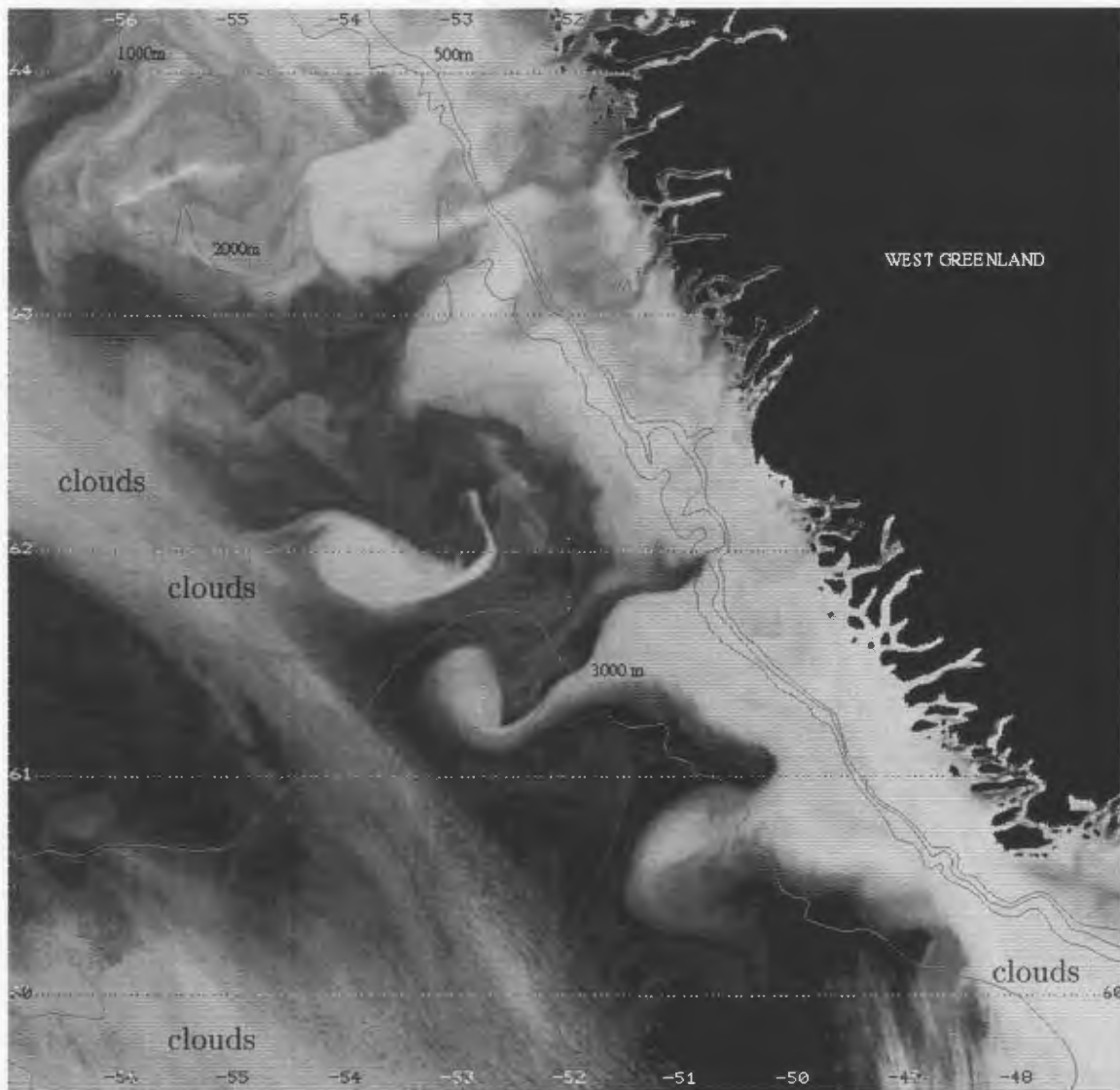


Figure 4.7: NOAA-14 (Channel 4, August 15, 1995, 0545 UTC) image of West Greenland region after cloud detection and land masking. Also shown are bathymetric contours (500 - 3000 m).

Chapter 5

Mesoscale features off the West Greenland coast observed in NOAA-AVHRR infrared imagery

5.1 AVHRR data selection and processing

Since 1994, roughly four passes of AVHRR data have been acquired each day from the available satellites NOAA-9,11,12 and 14 at the NWAFC satellite receiving station. The extensive database of archived AVHRR images were examined using a quicklook facility at the receiving station to select images that were relatively cloud-free and exhibited interesting oceanographic features off the coast of West Greenland. The day and time intervals between the images selected for the study acquired during 1995 and 1996 are listed in Table. 5.1 and Table. 5.2 respectively. Because of the presence of cloud over the West Greenland region, only the images listed in Table. 5.1 and Table. 5.2 that were relatively cloud-free representing summer and fall seasons could be selected for the study. The selected images were processed using the sequence of processing steps shown in Fig. 4.1 (Chapter 4). The details associated with each processing step are described in Chapter 4. We summarize them briefly here. First, the missing and corrupted scanlines in the raw archived data were detected and replaced with blank

Table 5.1: List of AVHRR thermal imageries for the year 1995.

No.	Satellite	Date	Time UTC
1	NOAA-12	30 June	21.46
2	NOAA-12	8 July	10.48
3	NOAA-12	29 July	11.31
4	NOAA-14	29 July	16.58
5	NOAA-12	30 July	11.09
6	NOAA-14	10 August	16.29
7	NOAA-14	11 August	06.29
8	NOAA-14	15 August	05.45
9	NOAA-12	15 August	10.22
10	NOAA-14	23 October	06.44
11	NOAA-14	21 November	16.21

scanlines. Second, radiometric calibration was performed to convert the thermal infrared data (channels 3,4 and 5) to brightness temperatures. Third, a two step navigation procedure was used to correct the images for distortions due to earth shape, variations caused by satellite orbit and deviation caused by satellite attitude. In the first step, the indirect navigation algorithm of Rosborough *et al.*, (1994) was used to correct for geometric distortions due to the earth's shape and rotation and satellite orbit variations. Next, the errors due to satellite attitude and timing were corrected using Ground Control Points. The images were all geometrically corrected to a fixed Mercator projection with a pixel resolution of approximately 1 km. The region covered by all the images presented in this chapter extend from 47° W to 57° W in longitude and 59° 24' N to 64° 06' N in latitude. After the completion of geometric correction, a simple cloud masking procedure

Table 5.2: List of AVHRR thermal imageries for the year 1996.

No.	Satellite	Date	Time UTC
1	NOAA-14	22 June	16.13
2	NOAA-12	16 July	21.26
3	NOAA-14	24 July	17.07
4	NOAA-14	27 July	16.34
5	NOAA-12	27 July	20.46
6	NOAA-12	10 August	20.41
7	NOAA-12	14 September	21.25
8	NOAA-12	15 September	11.09
9	NOAA-12	25 October	21.19

based on thermal infrared brightness temperature threshold (270 K) was used to eliminate the cloud contaminated pixels. The land masking was performed by masking out the polygons created using the digital vector coastline file (General Bathymetric Chart of the Oceans, GEBCO chart number 5.04). Finally, the images were contrast enhanced in order to get a good view of the features seen in them. They were then analysed to determine the spatial and temporal characteristics of oceanic features off the coast of West Greenland.

5.2 Results

In this section, the principal mesoscale circulation features observed off the West Greenland coast are described by choosing typical images from similar months representing summer and fall seasons in each year (1995 and 1996). Then, the results of the spatial

and temporal scale analysis of the mesoscale features are described. In all the images (Figures) that will be presented in this section, the darker shades represent warm water and the lighter shades represent cold water.

5.2.1 Observations of mesoscale surface circulation features

Fig. 5.1 and Fig. 5.2 show the surface conditions off the coast of West Greenland region on 29 July 1995 and 27 July 1996 respectively that represent the summer season in each year. The two images show similar surface circulation features. The principal features observed are the following: (i) a band of cold water (East Greenland Current) along the coast of West Greenland, (ii) adjacent to the cold water lies the warm or Atlantic component water (Irminger Current), (iii) a distinct front separating the warm and cold water, (iv) a wave-like pattern with mesoscale meanders along the front, (v) filaments extending seaward from the cold current, (vi) cyclonic tongue and/or hook-like feature (Fig 5.1) showing the development of a cyclonic eddy, and (vii) the presence of off-shore eddies.

The NOAA-AVHRR images obtained on 23 October 1995 and 25 October 1996 respectively off the coast of West Greenland (Fig. 5.3 and Fig. 5.4) represent the fall season. The most prominent feature observed in these images is the patch of warm water intruding shoreward across the West Greenland coast. Mesoscale features such as wave-like pattern and meanders observed in summer images are also observed in the images that represent the fall conditions. These images that show the surface conditions off the

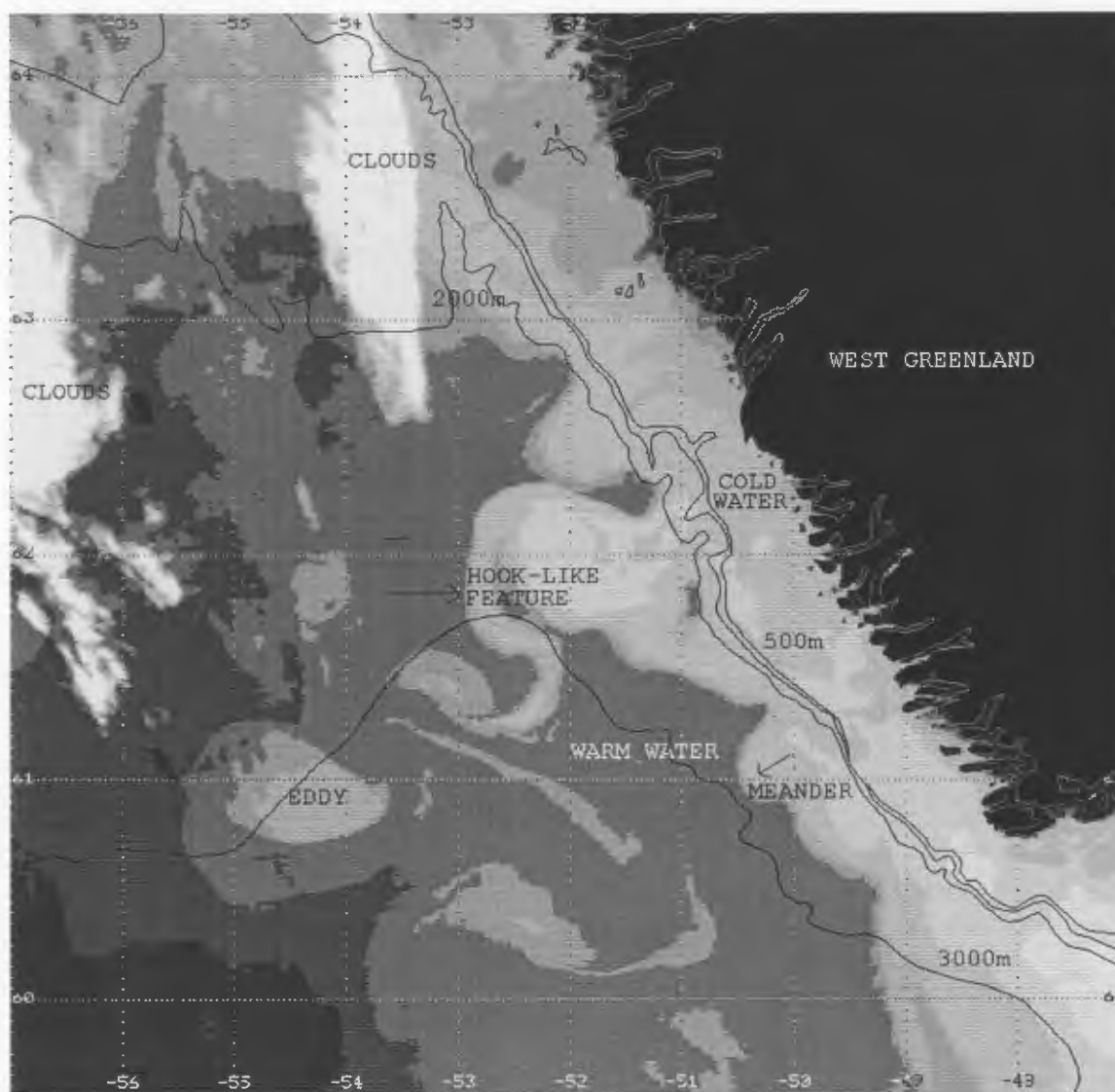


Figure 5.1: NOAA-14 AVHRR channel 4 image of the West Greenland region that show the surface conditions on July 29, 1995, 1658 UTC. Also shown are the bathymetric contours.

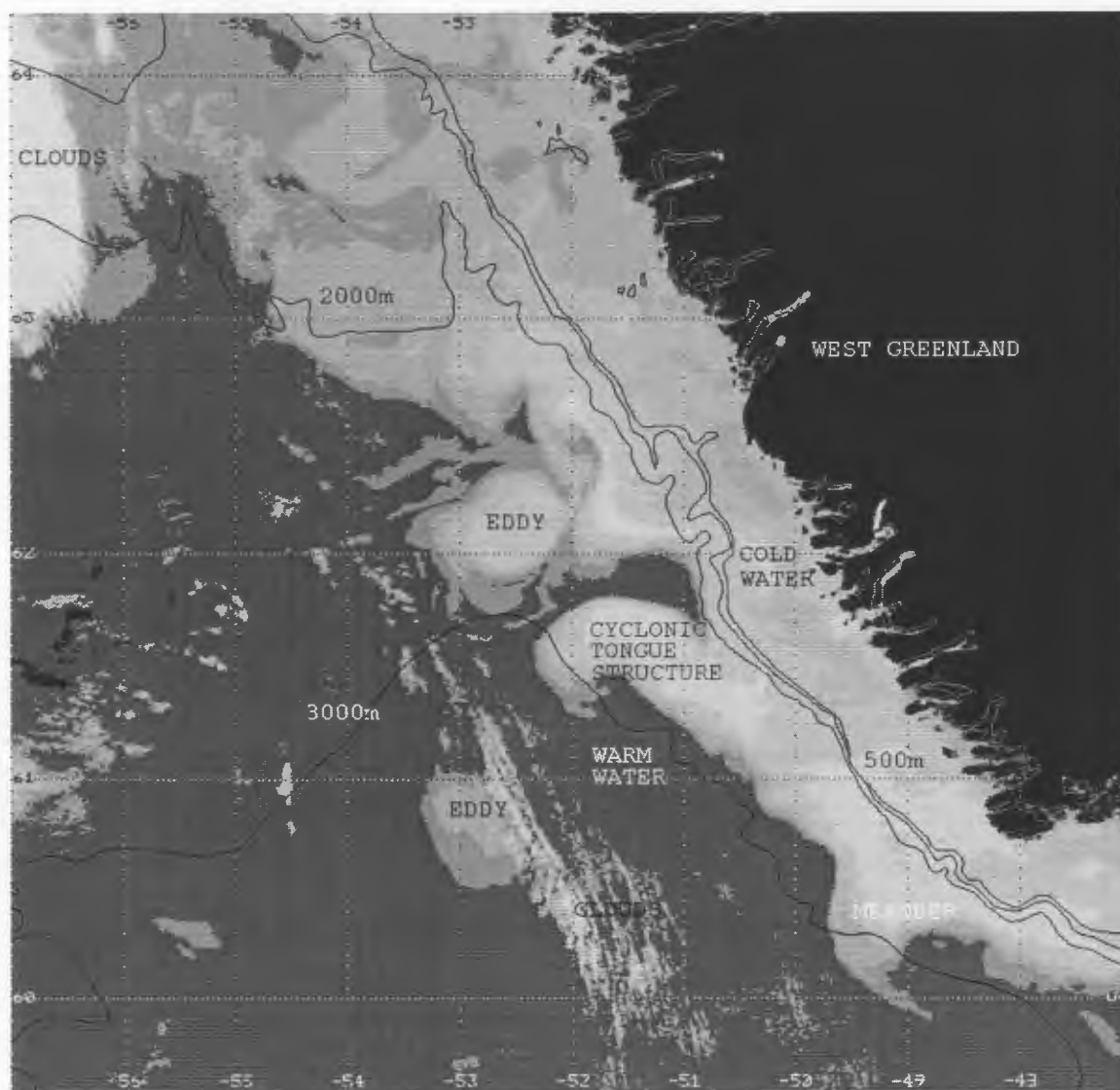


Figure 5.2: NOAA-14 AVHRR channel 4 image of the West Greenland region that show the surface conditions on July 27, 1996, 1634 UTC. Also shown are the bathymetric contours.

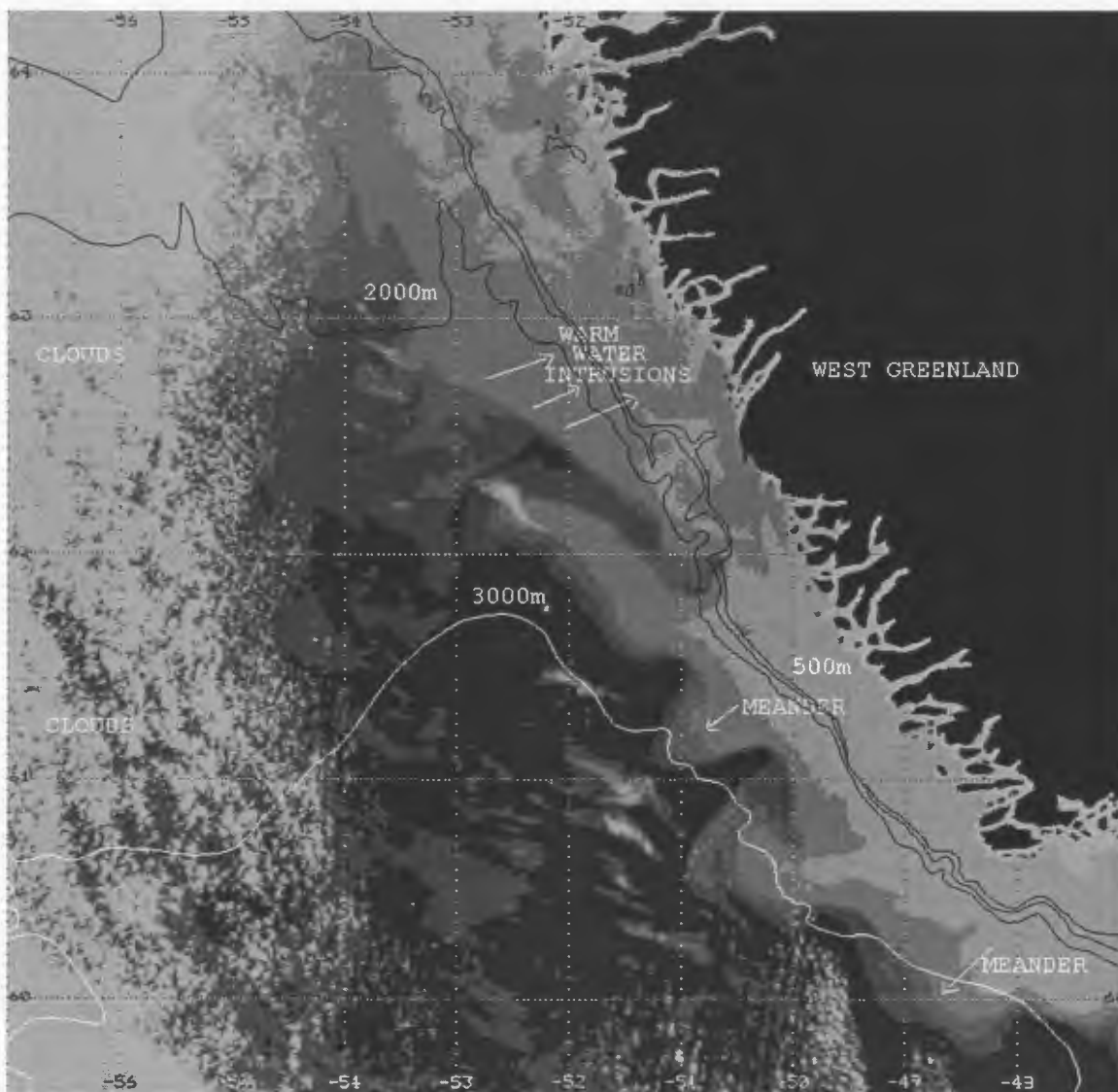


Figure 5.3: NOAA-14 AVHRR channel 4 image of the West Greenland region that show the surface conditions on October 23, 1995, 0644 UTC. Also shown are the bathymetric contours.

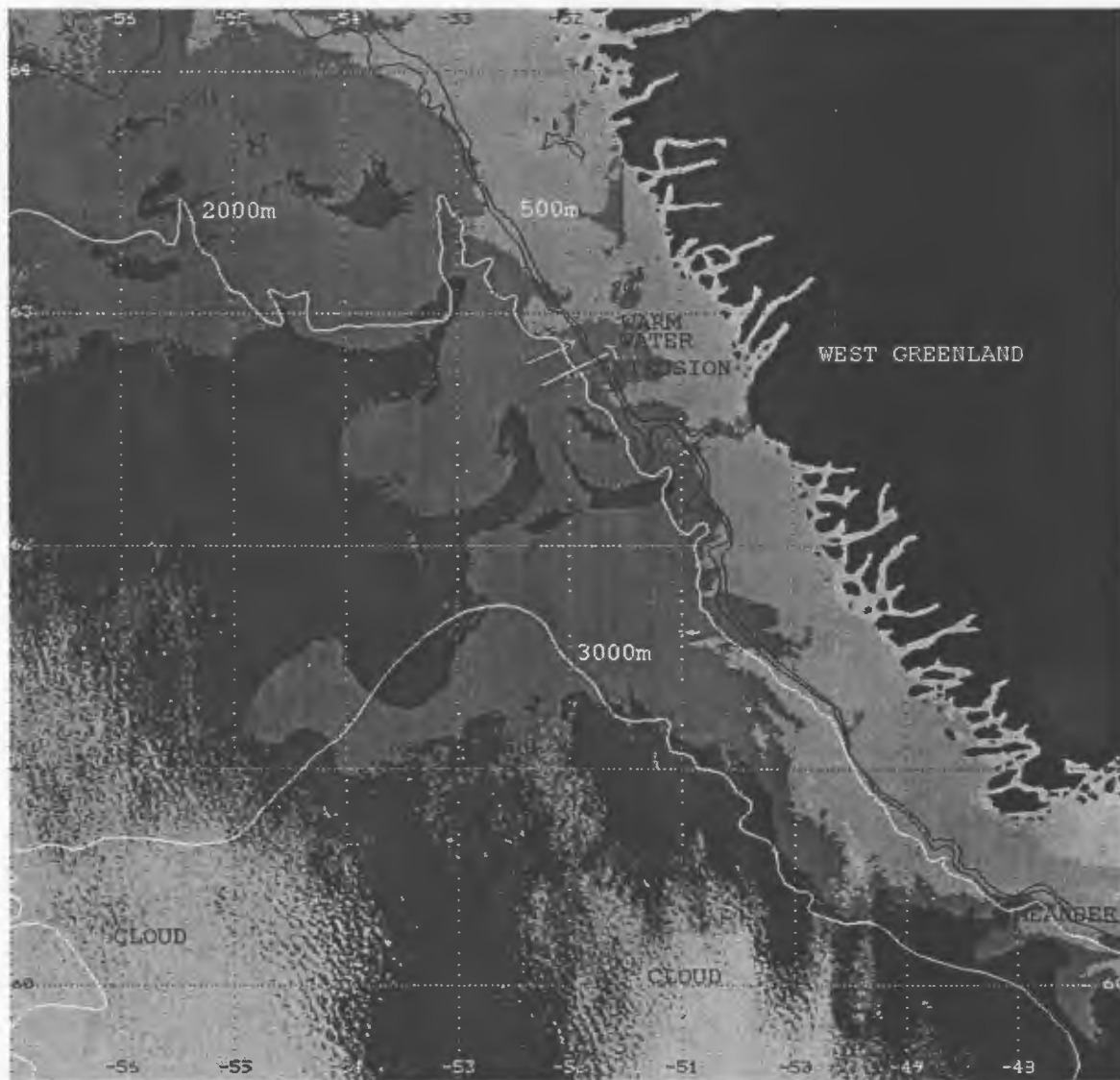


Figure 5.4: NOAA-12 AVHRR channel 4 image of the West Greenland region that show the surface conditions on October 25, 1996, 2119 UTC. Also shown are the bathymetric contours.

coast of West Greenland during summer and fall indicate the co-existence of cold East Greenland Current and the warm Irminger Current components of the West Greenland Current system. These mesoscale features (thermal front, meanders and eddies) of the West Greenland Current resemble similar features observed in the Norwegian Coastal Current (Johannessen *et al.*, 1989), the California Current (Mooers and Robinson, 1984) and in the Ushant frontal system (Pingree and Griffiths, 1978), and have significant ecological implications in that they may affect the nutrient supply and the dispersal of cod eggs and larvae. The principal mesoscale circulation features observed in the West Greenland Current and reported here during summer and fall seasons have never before been described using NOAA-AVHRR satellite imagery.

5.2.2 Spatial and temporal scale analysis of mesoscale features

In this subsection, we describe the spatial and temporal characteristics of mesoscale features observed in the NOAA-AVHRR infrared images (Table. 5.1 and Table. 5.2) acquired during 1995 and 1996. First, the results of the analyses of images obtained during 1995 are described. Figs. 5.5 - 5.13 show the NOAA-AVHRR channel 4 ($11\mu\text{m}$) images of the West Greenland region obtained between 30 June 1995 and 21 November 1995. Analyses of the images show interesting mesoscale features in the West Greenland Current. Although roughly four daily passes of NOAA-AVHRR data are acquired over this region at the NWAFC satellite laboratory, only the images listed in Table. 5.1 were sufficiently cloud free to be useful for the present study. Fig. 5.5 shows the NOAA-12

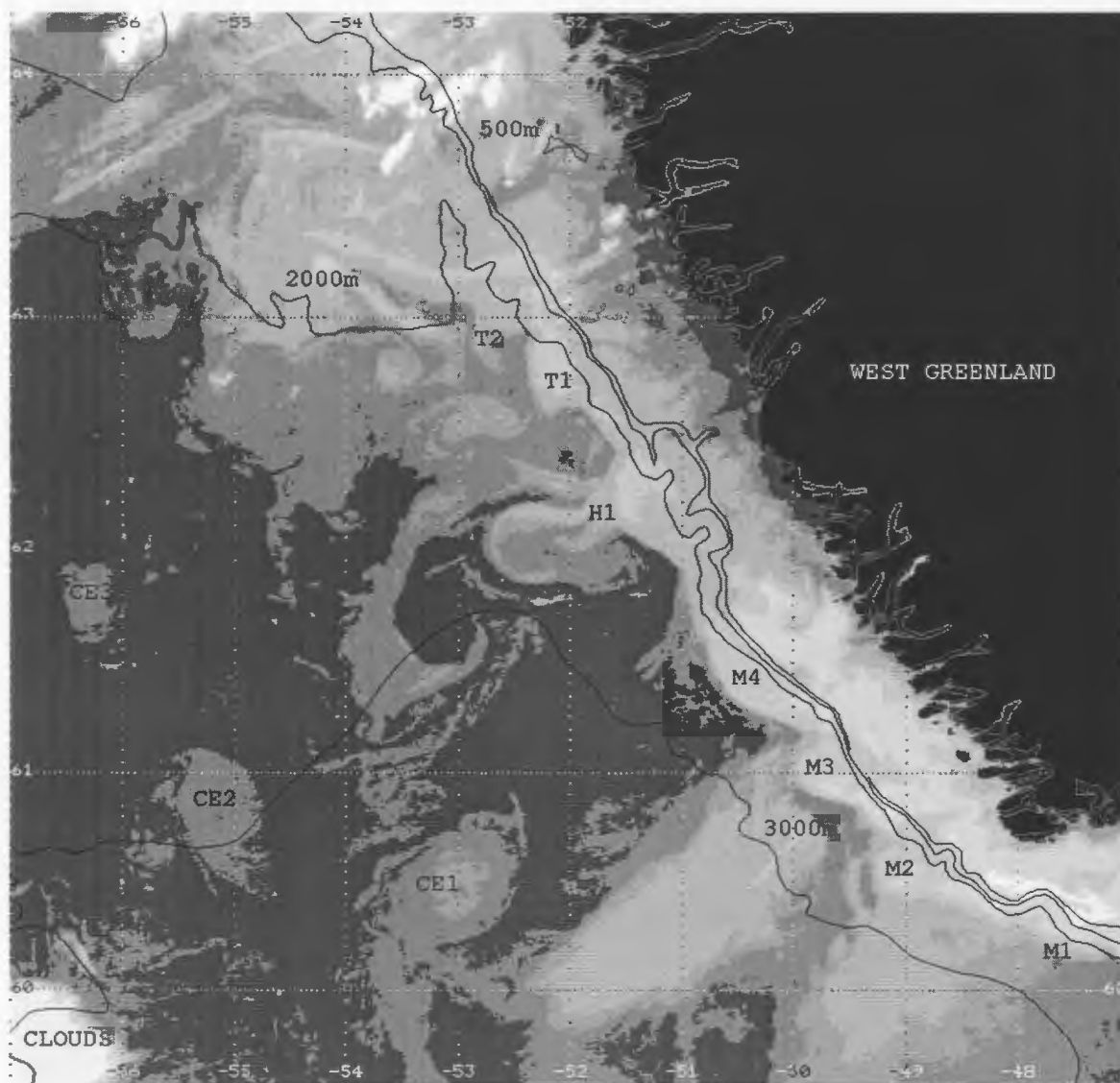


Figure 5.5: NOAA-12 AVHRR image, 30 June 1995, 2146 UTC. Also shown are the bathymetric contours.

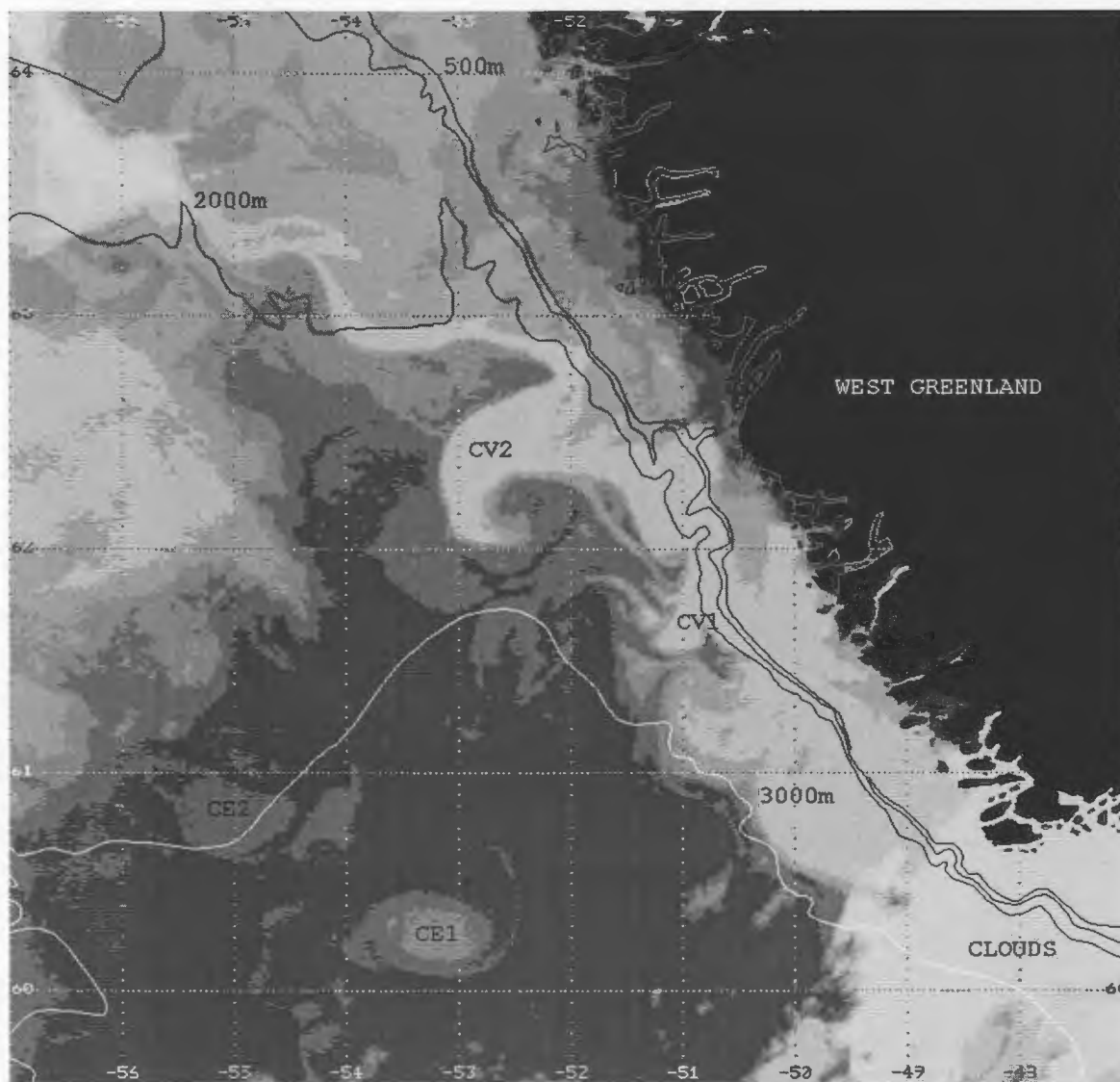


Figure 5.6: NOAA-12 channel 4 image, 8 July 1995, 1048 UTC.

AVHRR image acquired on 30 June 1995 at 2146 UTC. The interesting feature to note is the wave-like pattern with humps or meanders along the front that separates the cold inshore water from the warmer off-shore water. The meanders observed in the image are designated as M1, M2, M3 and M4 sequentially from south (along the front), and have length scales of ≈ 50 -100 km. Along the front (northwest of meander M4), hook-like (H1, Fig. 5.5) and cyclonic tongue (T1 and T2, Fig 5.5) features of cold water (lighter shade) are evident. The movement and elongation of cold water patches (northwest of M4, H1, T1 and T2) show the mixing across front between the cold and warm off-shore water. The features H1, T1 and T2 have length scales of ≈ 40 -50 km. Also the presence of three eddies (CE1, CE2 and CE3), enclosing cold water can be seen in Fig. 5.5. It is possible that these eddies would have pinched off from the front and drifted off-shore. Eddy CE1 is centered at $60^{\circ} 30' N$, $53^{\circ} W$, while eddies CE2 and CE3 are positioned at $60^{\circ} 52' N$, $55^{\circ} 10' W$ and $61^{\circ} 50' N$, $56^{\circ} 30' W$ respectively. They were found to be located off-shore and have diameters of about 30-60 km. The eddies CE1 and CE3 lie separated from eddy CE2 by a distance of about ≈ 120 km. The next sufficiently cloud-free image was available 8 days later at 1048 UTC 8 July 1995 (NOAA-12 image, Fig. 5.6). By 8 July 1995 (Fig. 5.6) these meanders have undergone a significant change from 30 June 1995 (Fig. 5.5). Two vortices designated as CV1 and CV2, enclosing cold water are readily noticeable in Fig. 5.6. The readily distinguishable hook in CV2 appears about to close to become a cyclonic eddy. The cyclonic eddies (CE1 and CE2 identified in Fig. 5.5) are seen centered at $60^{\circ} 15' N$, $53^{\circ} 15' W$ and $60^{\circ} 46' N$, $55^{\circ} W$ respectively. Between 30

June and 8 July 1995, the eddy CE1 has moved southwestward by a distance of 30 km, whereas the eddy CE2 has moved southeastward by a distance of 15 km. This suggests a displacement rate of the eddy center of approximately 3.5 km d^{-1} (0.04 ms^{-1}) and 0.9 km d^{-1} (0.01 ms^{-1}) for eddy CE1 and CE2 respectively. Also a wave-like pattern with meanders and cross-frontal mixing could be seen northwest of CV2 and south of CV1 (Fig. 5.6).

Fig. 5.7 shows the next available NOAA-12 AVHRR channel 4 image obtained on 29 July 1995, 1131 UTC. A distinct near-circular feature (NC1) of cold water centred about $61^{\circ} 52' \text{ N}$, $51^{\circ} 56' \text{ W}$ is apparent (Fig. 5.7). Also notable is the presence of meanders north and south of this feature. The near-circular feature with a readily distinguishable hook lies stretched seaward, and is in position to detach from the front to become an eddy. There is also evidence of entrainment of cold shelf water on the northern and southern boundaries of this feature, suggesting that the cold water patches are drawn seaward and northwestward in a cyclonic sense by the West Greenland Current flow as it enters the eddy. This is best illustrated in the image acquired a day later at 1109 UTC 30 July 1995 (Fig. 5.8). This image contained less cloud cover than the earlier image (Fig. 5.7), particularly the deep ocean region off the coast of West Greenland and northwestern portion of the image are clearly visible. An off-shore eddy (NC2) is centered at $60^{\circ} 48' \text{ N}$, $54^{\circ} 46' \text{ W}$, and a near-circular patch of cold water (NC3) is positioned at $62^{\circ} 45' \text{ N}$, $55^{\circ} 06' \text{ W}$ which appears to be in a position to get detached

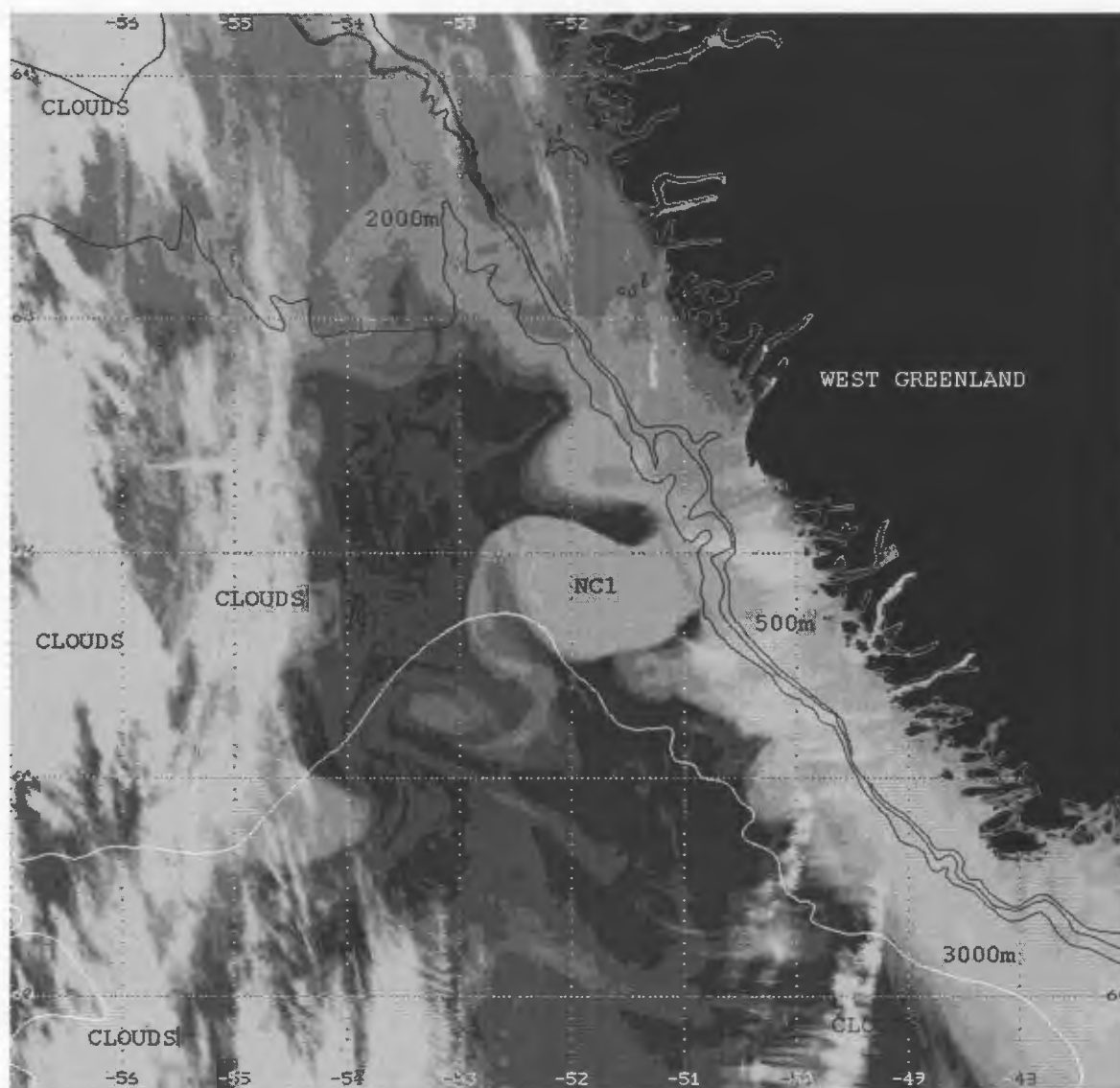


Figure 5.7: NOAA-12 channel 4 image, 29 July 1995, 1131 UTC.

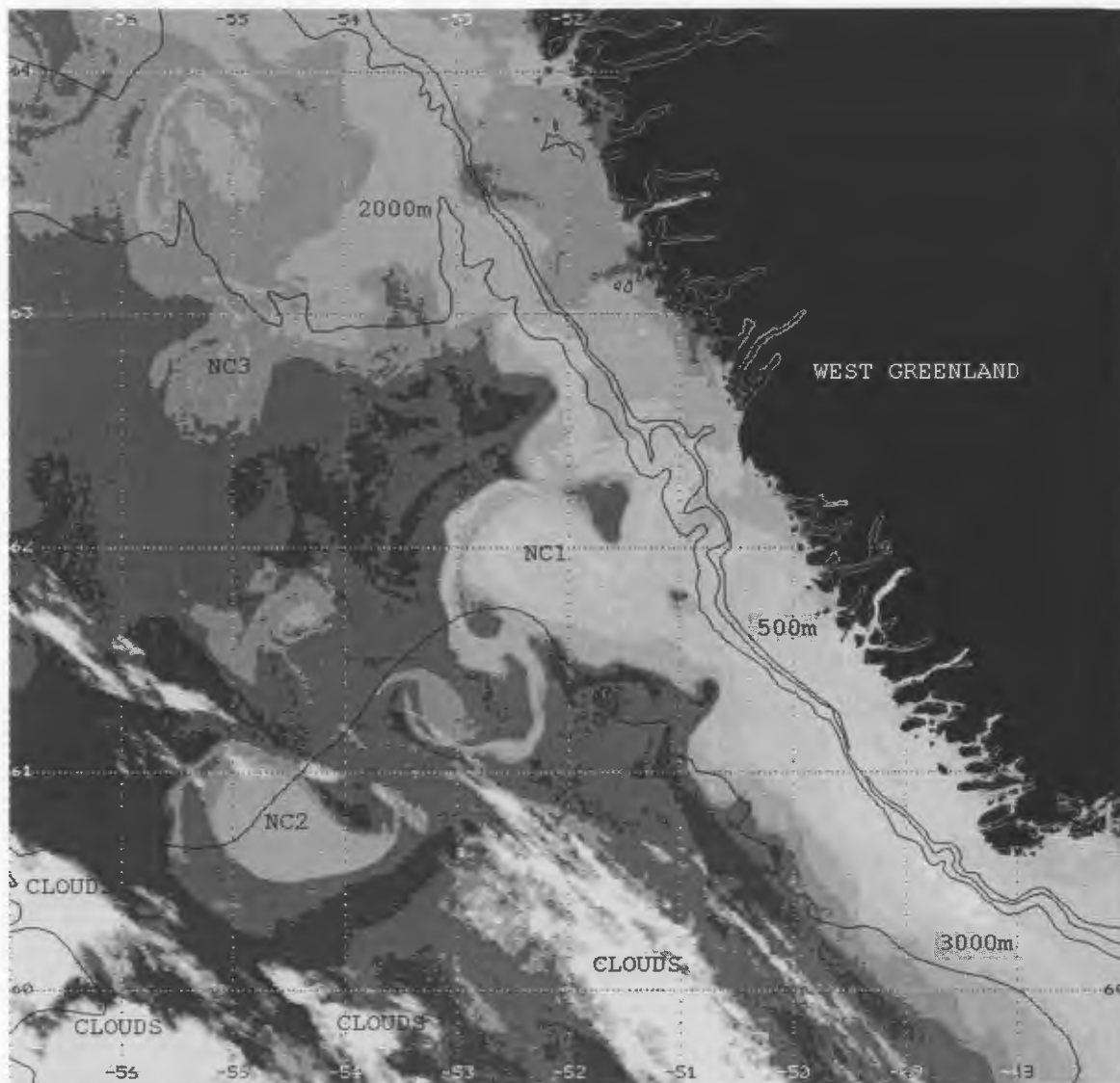


Figure 5.8: NOAA-12 channel 4 image, 30 July 1995, 1109 UTC.

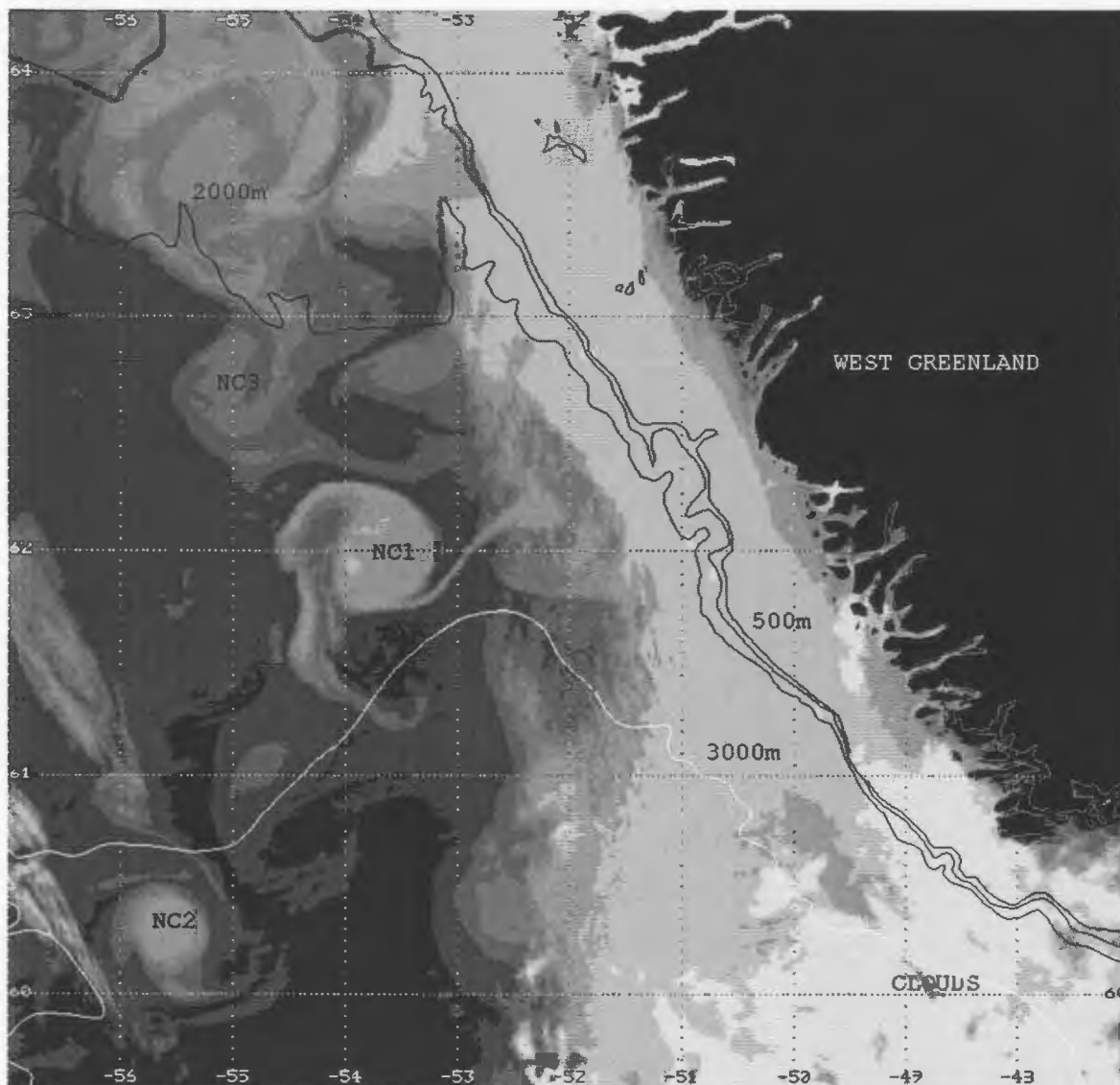


Figure 5.9: NOAA-14 channel 4 image, 10 August 1995, 1629 UTC.

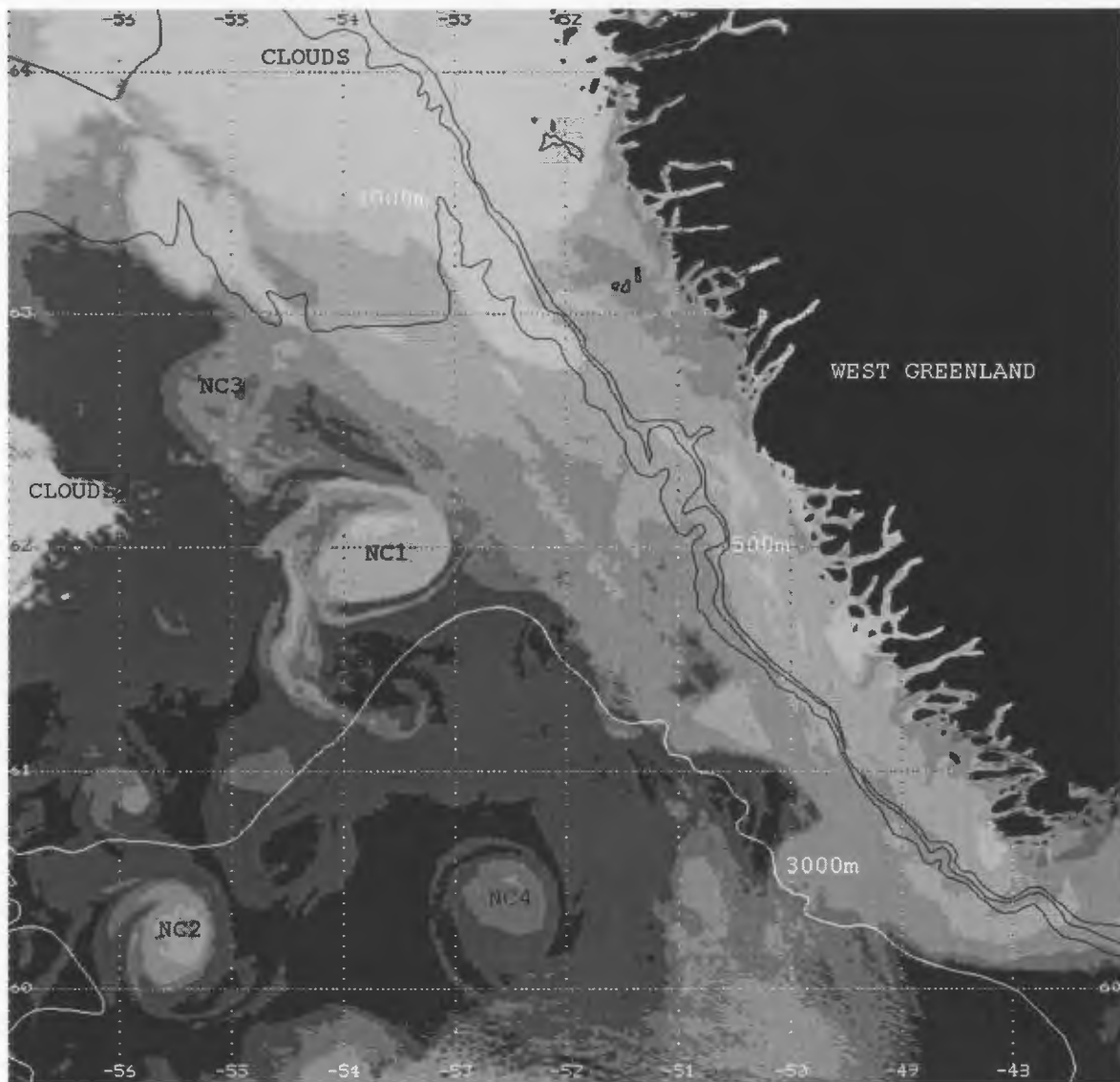


Figure 5.10: NOAA-14 channel 4 image, 11 August 1995, 0629 UTC.

from the front can be seen in Fig. 5.8. For the next ten days, excessive cloud cover over the West Greenland region made it difficult to monitor and track the features. The next available cloud-free NOAA-14 AVHRR image is for 10 August 1995, 1629 UTC (Fig. 5.9). The coastal region of West Greenland and the southeastern portion of the image are covered with clouds. The near-circular feature (NC1 seen in Fig. 5.8) developed into an eddy, detached and is clearly discernible centered at 62° N , $53^{\circ} 43'$ W. This eddy has a diameter of about 50 km, the distance it covered between 30 July and 10 August 1995 is approximately 75 km. This suggests a displacement rate of the eddy center of about 6.9 km d^{-1} (0.08 ms^{-1}). In addition to the eddy NC1, the eddy NC2 (seen in Fig. 5.8) can also be seen centred at $60^{\circ} 17'$ N , $55^{\circ} 30'$ W (Fig. 5.9). Eddy NC2 covered a distance of 70 km in 11 days, suggesting a displacement rate of the eddy center of about 6.0 km d^{-1} (0.07 ms^{-1}). The hook-like appearance (associated with feature NC1) looks similar to the feature observed in Ushant frontal system by Pingree and Griffiths (1978) in their study on cross-frontal mixing on the Northwest European continental shelf using satellite infrared images. Fig. 5.10 show the NOAA-14 image acquired on 11 August 1995, 0629 UTC. Though major portion of the image is covered by clouds, a good view of the off-shore region show the presence of an eddy (NC4) centered at $60^{\circ} 24'$ N , $52^{\circ} 35'$ W, in addition to NC1 and NC2.

Again for the next four days we did not obtain a cloud free image of the region off the coast of West Greenland and Fig. 5.11 (NOAA-14, August 15, 1995, 0545 UTC)

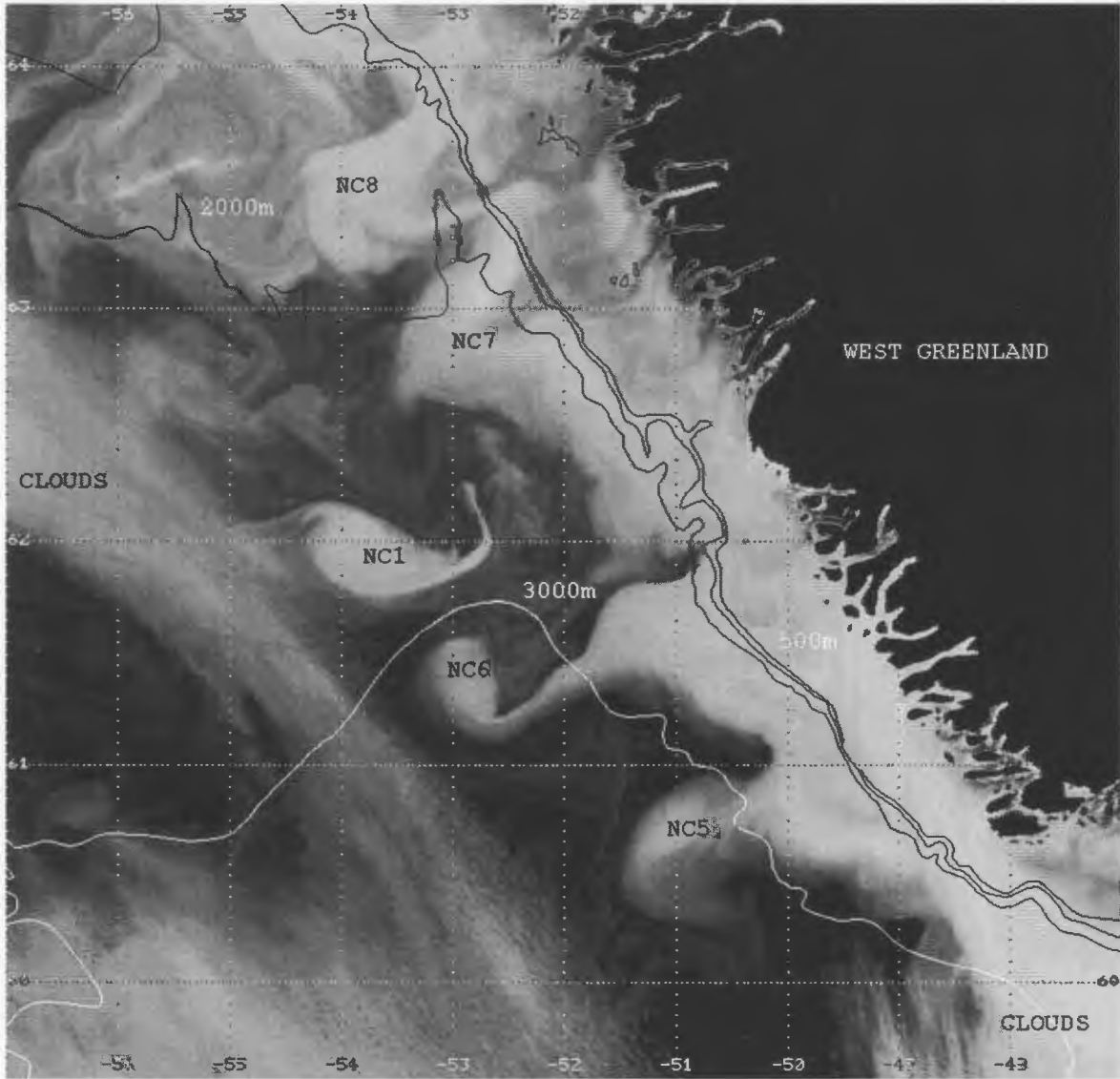


Figure 5.11: NOAA-14 channel 4 image, 15 August 1995, 0545 UTC.

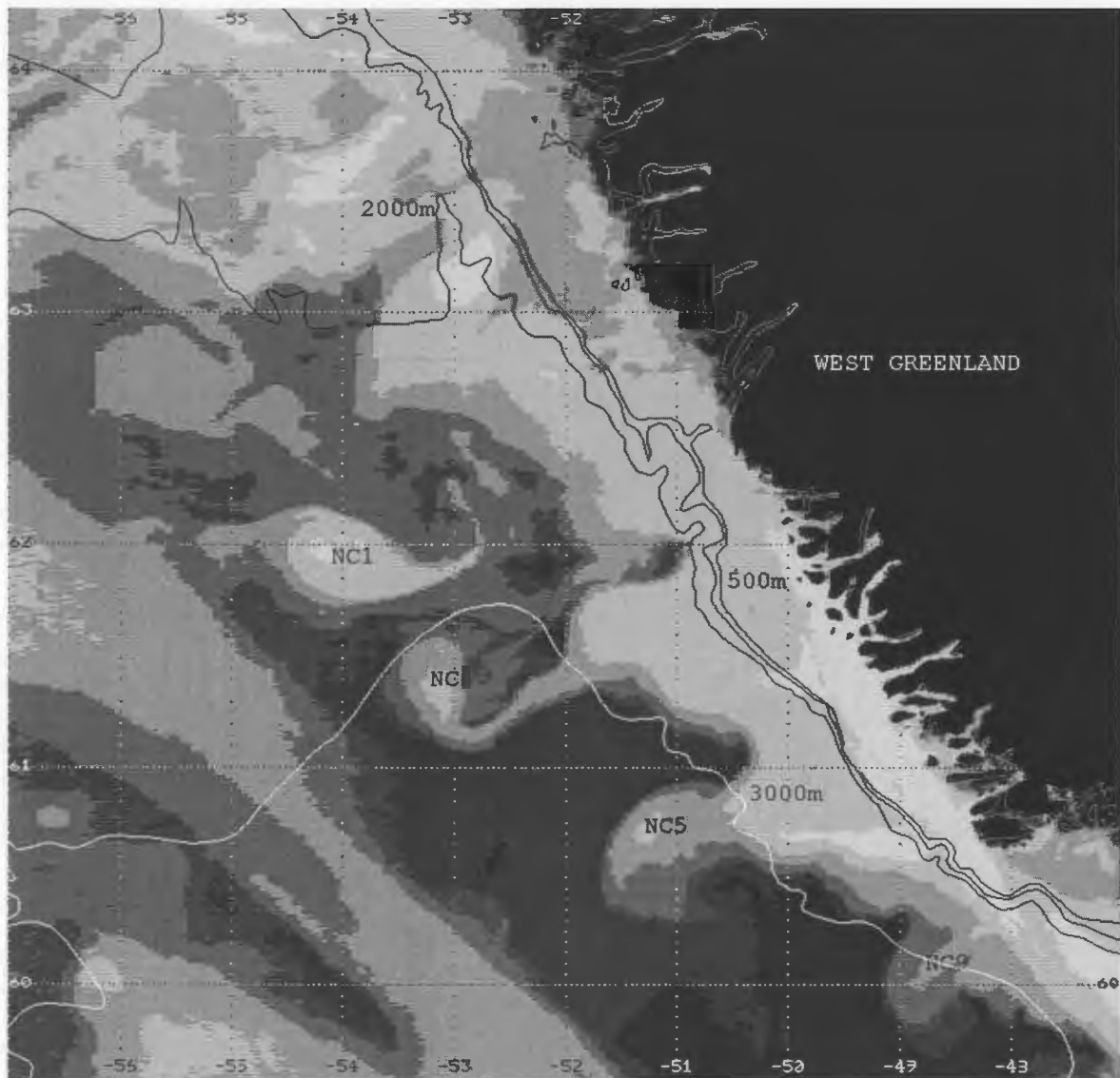


Figure 5.12: NOAA-12 channel 4 image, 15 August 1995, 1022 UTC.

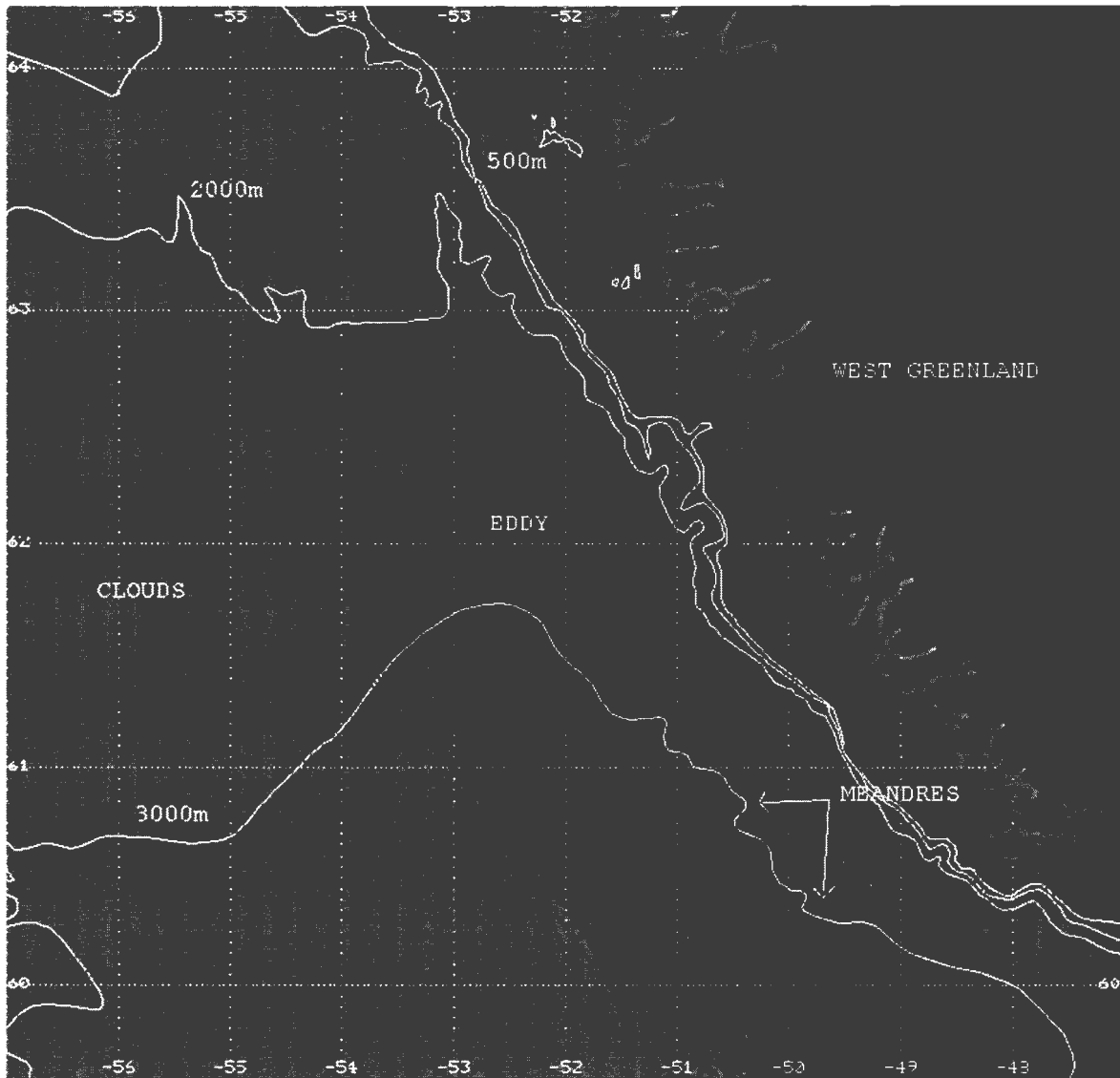


Figure 5.13: NOAA-14 channel 4 image, 21 November 1995, 1621 UTC.

shows the next sufficiently cloud free image available. Fig. 5.11 provides a good view of the eddy (NC1 seen in Fig. 5.9) with modified surface features. In addition, there are irregular eddies (NC5 and NC6) and meanders (NC7 and NC8) are seen south and north of NC1. Eddies NC5 and NC6 lie separated from each other by a distance of 120 km, while the distance between the meanders NC7 and NC8 is estimated to be 80 km. An image obtained 5h later at 1022 UTC 15 August 1995 (Fig. 5.12), shows another irregular meander southeast of NC5 designated as NC9. This was not seen in the earlier image (Fig. 5.11) as this portion was filled with clouds. NC9 lies 140 km southeast of NC5. Fig. 5.3 and Fig. 5.13 represent the NOAA-14 AVHRR images obtained on 23 October 1995, 0644 UTC and 21 November 1995, 1621 UTC respectively. These images represent the surface conditions off the coast of West Greenland during fall season. In both images the off-shore region is covered by clouds, but the coastal region of West Greenland is free of clouds. Similar surface features i.e., meanders and near-circular eddy like features could be observed in these images. The waters off the coast of West Greenland are warm (darker shade) and well mixed. The intrusions of warm water is evident in the images that represent fall season.

Figs. 5.14-5.20 represent the NOAA-AVHRR images obtained between 22 June 1996 and 25 October 1996 (Table. 5.2). The analyses of the images obtained in 1996 (that represent summer and fall conditions) exhibit similar mesoscale circulation features off the coast of West Greenland to those observed in the same seasons during 1995. Fig. 5.14

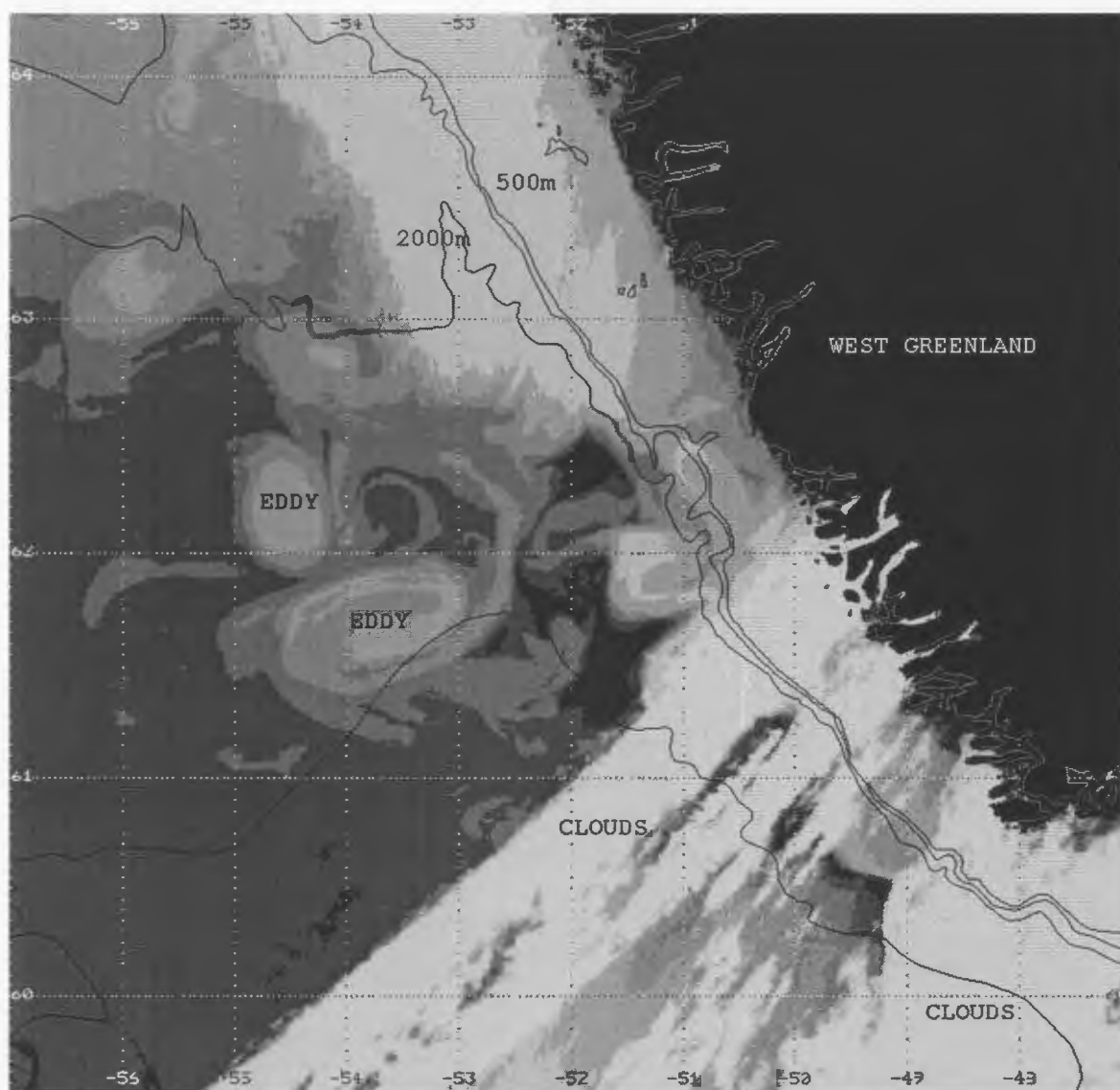


Figure 5.14: NOAA-14 AVHRR image, 22 June 1996, 1613 UTC. Also shown are the bathymetric contours.

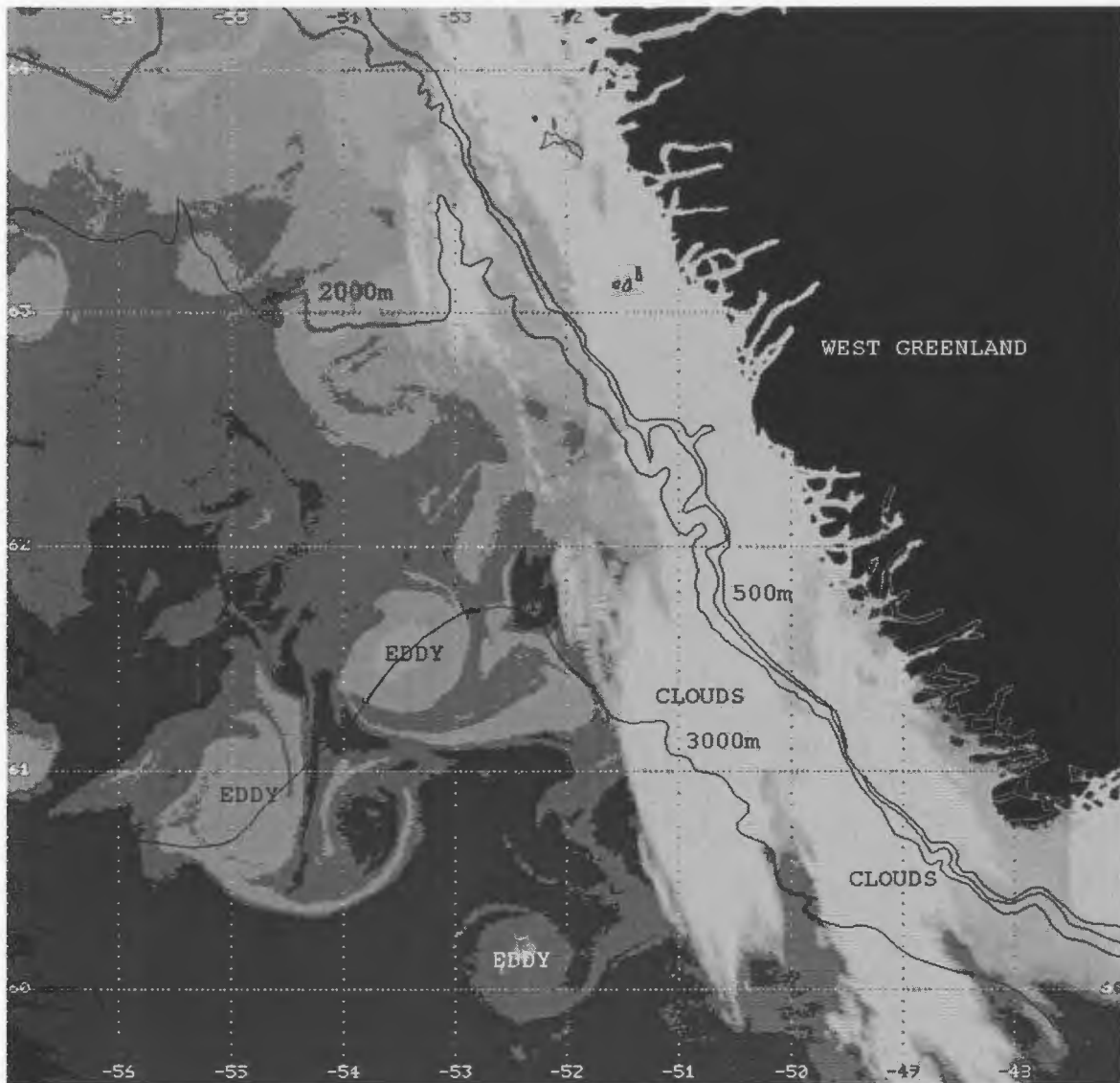


Figure 5.15: NOAA-12 channel 4 image, 16 July 1996, 2126 UTC.

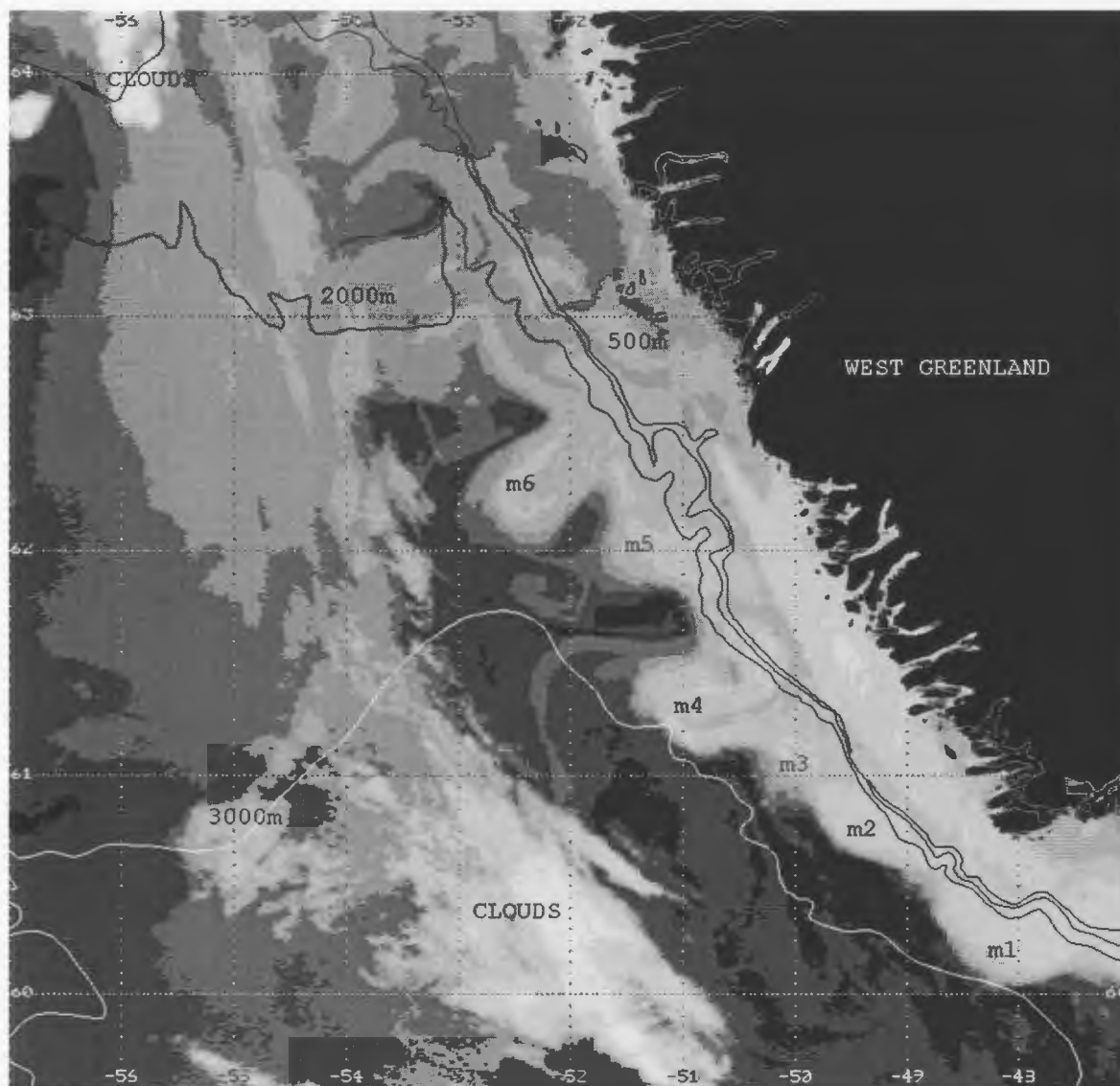


Figure 5.16: NOAA-14 channel 4 image, 24 July 1996, 1707 UTC.

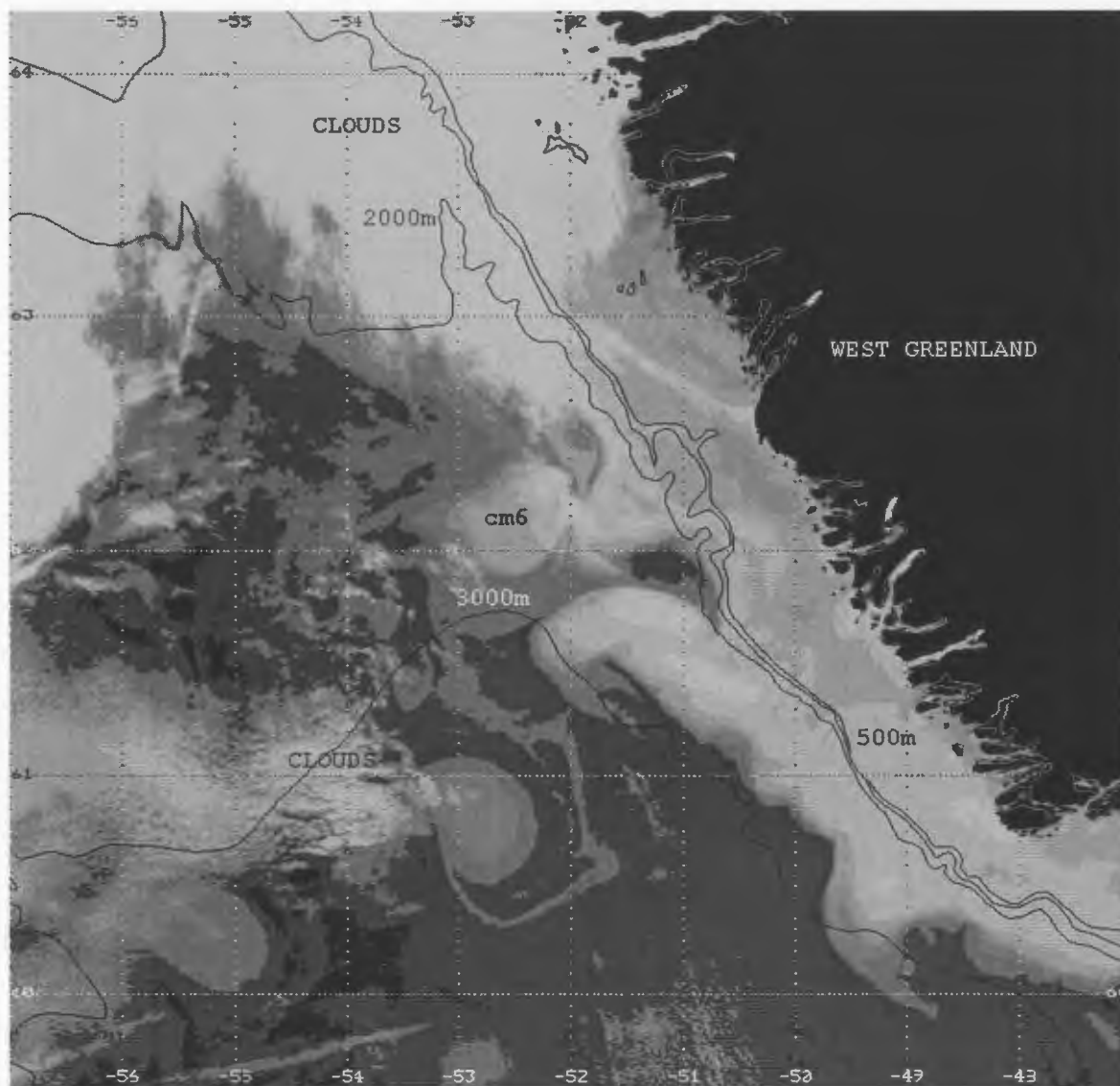


Figure 5.17: NOAA-14 channel 4 image, 27 July 1996, 2046 UTC.

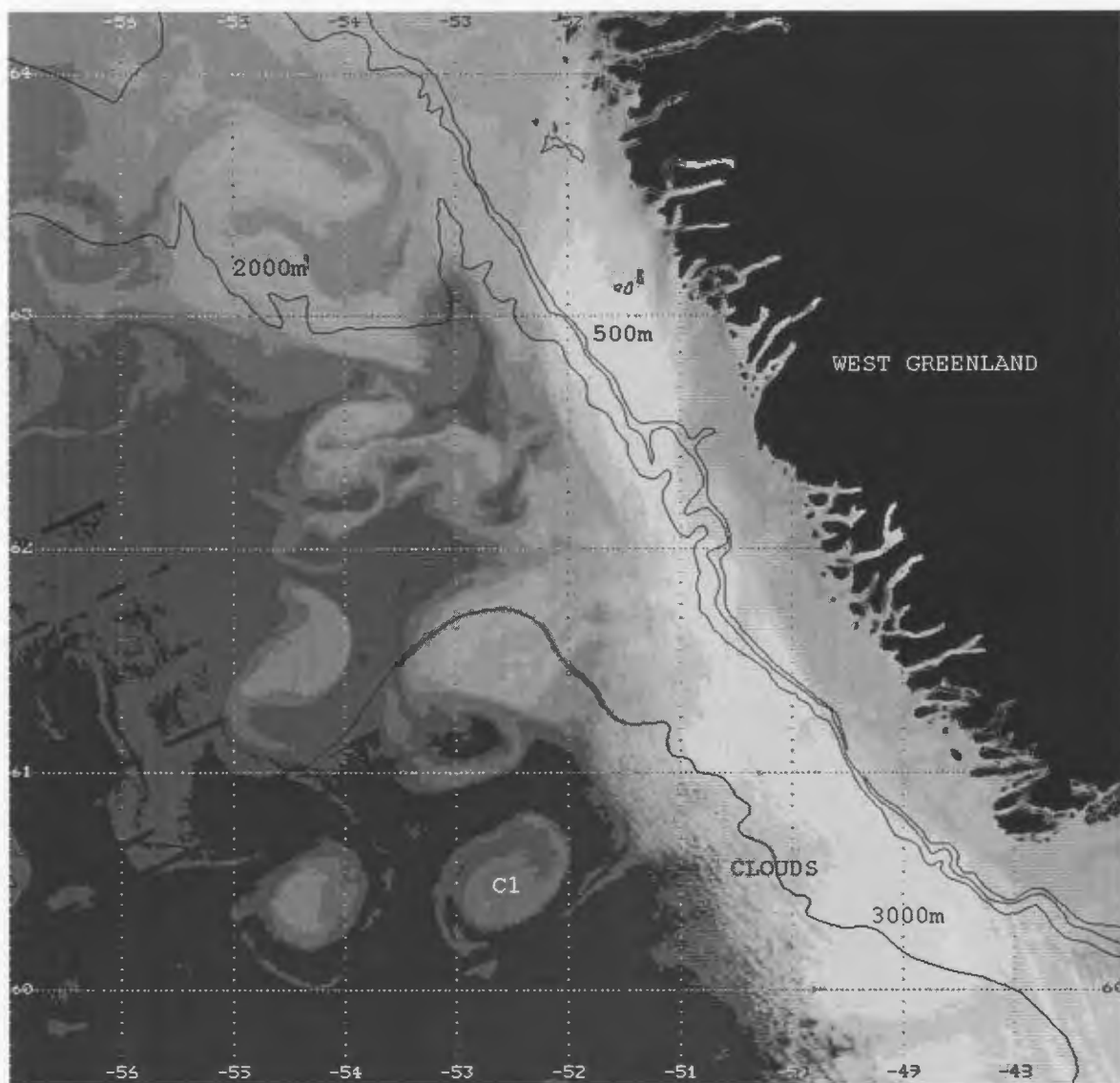


Figure 5.18: NOAA-14 channel 4 image, 10 August 1996, 2041 UTC.

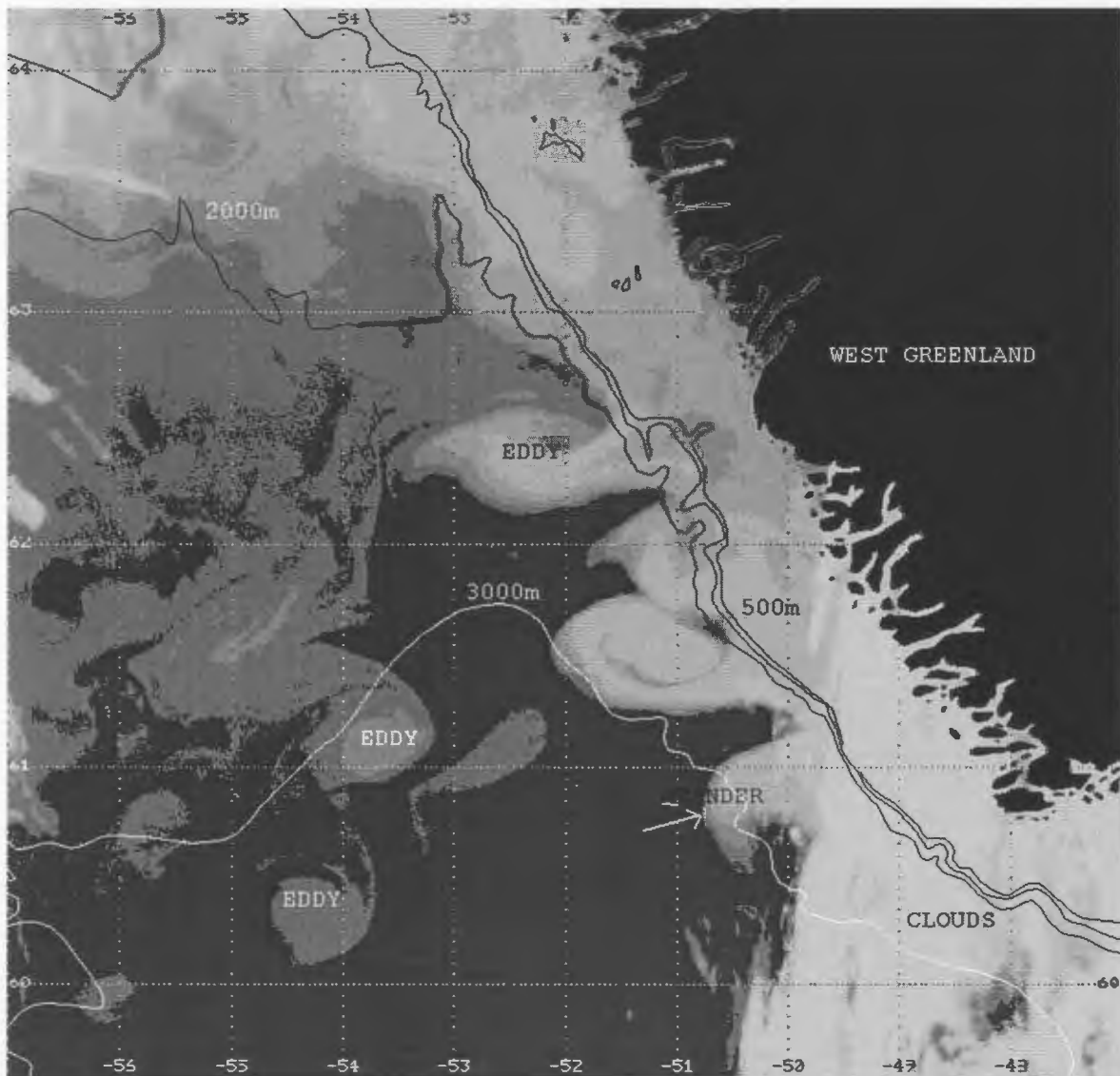


Figure 5.19: NOAA-14 channel 4 image, 14 September 1996, 2115 UTC.

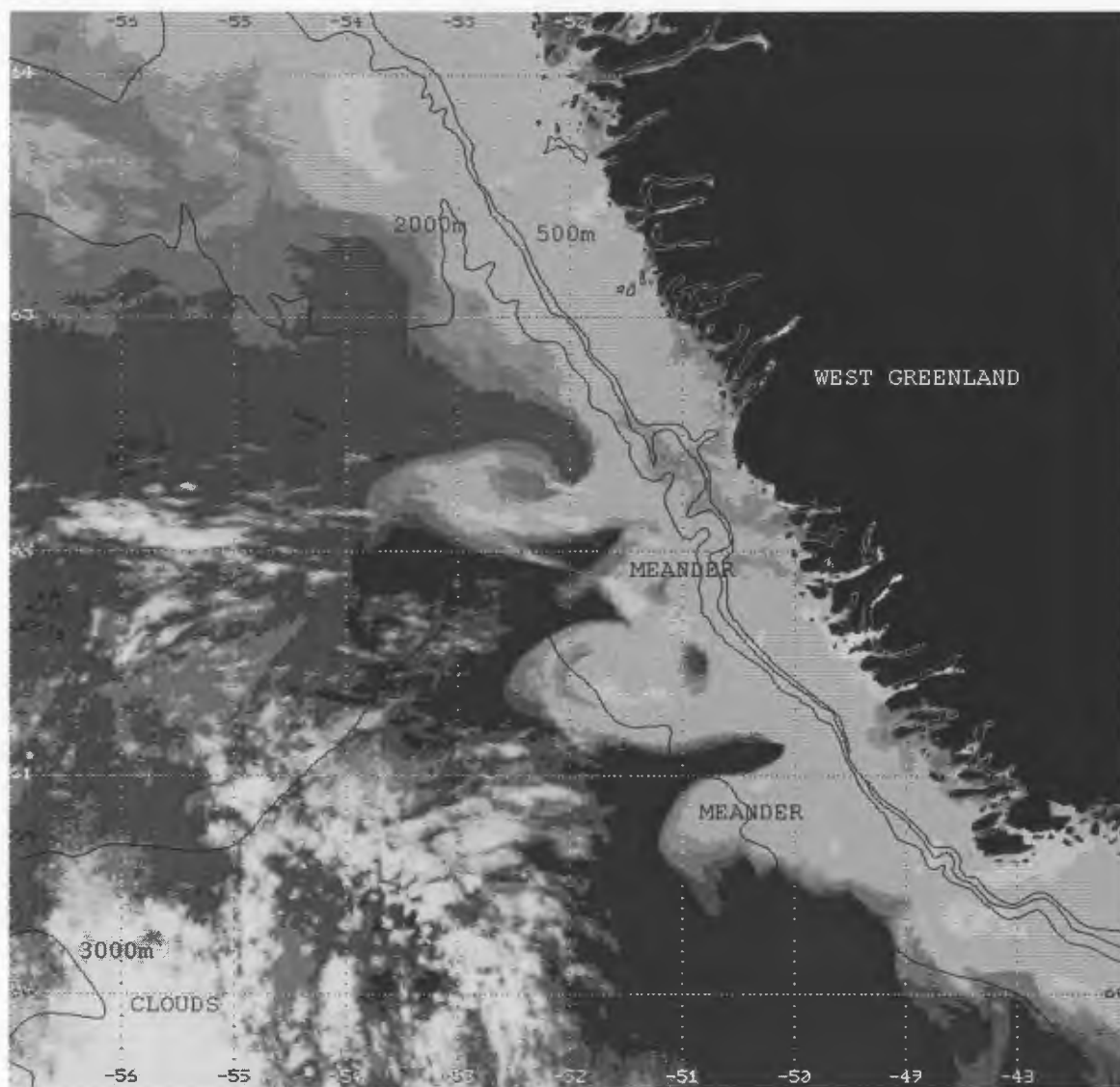


Figure 5.20: NOAA-12 channel 4 image, 15 September 1996, 1109 UTC.

and Fig. 5.15 show the contrast enhanced channel 4 AVHRR images obtained on 22 June 1996, 1613 UTC (NOAA-14) and 16 July 1996, 2126 UTC (NOAA-12) respectively. Though most areas of the two images were cloud covered, these images are presented to show the presence of several cyclonic eddies, enclosing cold water that lies off-shore. The surface features of these eddies were found to be very similar to the eddies identified in images obtained on 30 June and 8 July 1995 (Fig. 5.5 and Fig. 5.6). Fig. 5.16 and Fig. 5.17 represent the surface conditions off the coast of West Greenland observed on 24 July 1996, 1707 UTC and 27 July 1996, 2046 UTC respectively. The wave-like pattern with meanders similar to that observed in images obtained during 1995 in the same months could be seen in these images. The meanders (designated m1,m2,m3,m4,m5 and m6, Fig. 5.16) have length scales of about 40-80 km. Between 24 and 27 July 1996, the meanders grew, and the eddy (cm6) pinched off from m6 could be seen in Fig. 5.17. Fig. 5.18 represent the NOAA-14 AVHRR image obtained on 10 August 1996, 2041 UTC., which shows similar surface conditions as observed on 11 August 1995 (Fig. 5.10). The coastal region off the coast of West Greenland is cloud covered, but the off-shore area shows the presence of three well-defined cyclonic eddies. Fig. 5.19 and Fig. 5.20 show the NOAA-AVHRR images obtained on 14 and 15 September 1996 that represent the fall conditions. Both the images show interesting features. The image for 14 September shows the presence of off-shore eddies and meanders along the front. Unfortunately the southeastern portion of the image is covered by clouds. Fig. 5.20 (15 September 1996) gives a clear view of the coastal region and the presence meanders with larger

amplitude are seen clearly. The next cloud-free image that could be obtained over this region is given in Fig. 5.4 (NOAA-12, 25 October 1996, 2119 UTC). This image shows the intrusion of warm water which is similar to features observed in the image obtained for 23 October 1995. The above results of the analyses of images that represent the summer and fall seasons show the presence of mesoscale circulation features such as front, meanders and eddies off the West Greenland Coast. Also, the results suggest that the mesoscale variability in West Greenland waters is controlled by the two current components (the cold East Greenland current and warm Irminger Current) that together feed the West Greenland Current system.

5.3 Discussion

This chapter describes the results of the analyses of NOAA-AVHRR satellite infrared images of the waters off the coast of West Greenland. The images selected and presented were obtained from the NOAA-12 and 14 satellites. They represent the best sequences that could be found over this cloud prevalent region during summer and fall seasons of 1995 and 1996. The images obtained in each year show the presence of fronts, current meanders and eddies during both the seasons. This is the first time the spatial and temporal characteristics of mesoscale features present off the coast of West Greenland region is described using the NOAA-AVHRR infrared images. The images show distinct thermal front between cold and warm water components of the West Greenland Current. They also illustrate the presence of wavelike or meandering motions, development of

eddies and the presence of eddies offshore. The alongshore wavelength of meanders were between 50-100 km and 40-80 km in 1995 and 1996 respectively. The diameter of the eddies were estimated to be between 40 and 80 km.

Now, a discussion on the dynamical processes that could be responsible for the generation of current meanders and eddies observed in the satellite infrared images off the coast of West Greenland will be presented. The West Greenland Current consists of two components (cold inshore and warm offshore) that have different temperatures (and hence different densities). The exchange of water (cross-frontal mixing) and instabilities in the front which allow small departures from the geostrophic balance to grow at the expense of potential and/or kinetic energy could lead to the development of mesoscale features observed in the West Greenland Current. The irregularities with hooklike features and meandering motion observed in the infrared images often could curl up cold and warm waters together in a circular fashion to become an eddy that eventually gets detached from the front and moves offshore. In these hooklike and wavelike features maximum potential energy is released when the water gets exchanged in the frontal region, and this potential energy is converted into kinetic energy and this is used to drive the eddy motion. The instability mechanism which allows the eddies to grow with the energy supply that comes from the potential energy is called the baroclinic instability. The baroclinic instability is different from barotropic instability in which eddies may

be generated by shear in the mean flow and gain their energy from the mean flow kinetic energy. As there is no vertical variation of velocity in the barotropic flow, there can be no vertical shear and horizontal shear is required for the disturbances to grow. These processes of eddy generation are similar to the processes generating cyclonic lows (eddies) in the mid-latitude atmosphere which provide variable weather and storms of those latitudes. Marine meteorological conditions over the West Greenland region such as variability of winds (direction and speed), and currents generated by these systems could become unstable and lead to the formation of mesoscale features observed in the West Greenland Current. The topographic irregularities and coastline geometry could enhance the growth of instabilities.

There are numerous studies (Pedlosky, 1964; Orlanski, 1968; Blaeck *et al.*, 1988; Flament *et al.*, 1985; Turner, 1981) found in the literature on the dynamical processes that could be responsible for the generation, growth of meanders and eddies based on hydrographic observations, satellite infrared images and numerical modelling. LeBlond (1982), in his studies on Labrador Current using NOAA satellite visible images observed mesoscale ice-edge meanders off the Labrador Coast with alongshore wavelength between 30 and 100 km, and suggested that the meanders are related to the Labrador Current meanders and attributed baroclinic instability of the Labrador Current is the likely generation mechanism. Ice-edge meanders were also observed in the East Greenland Current

(Johannessen *et al.*, 1983; Wadhams and Squire, 1983 and Smith *et al.*, 1984). The baroclinic and barotropic instabilities together with the bottom topography variations were thought to be the generation mechanism for the meanders. Ikeda and Emery (1984) and Ikeda *et al.*, (1984a,b) and Haidgoval *et al.*, (1991) in their studies on the generation of meanders and eddies in the California Current suggest that the generative mechanism arises from the baroclinic and/or barotropic instability of the mean coastal California Current which, during upwelling season (April to September) that consists of the equatorward California Current overlying the poleward California Under Current. Thompson and Gower (1985) studied the relationship between a wind event and meander growth in the California Current System. Based on the spatial and temporal scales of the observed motions, they conclude that eddy growth arises through mixed barotropic-baroclinic instability of the wind-induced current. Ikeda (1987) used the idea of Thompson and Gower (1985) to study the links between wind and meanders, and also the influence of bottom topography in the generation of mesoscale ice-edge meanders off the Labrador coast. There are also studies in other current systems such as Gulf Stream (Robinson *et al.*, 1988), Norwegian Coastal Current (Ikeda *et al.*, 1989; Johannessen *et al.*, 1989), Kurushio (Kimura and Sugimoto, 1993) and Leewind Current (Pearce and Griffiths, 1991).

The vertical extent of the features and their relationship with the subsurface water can be drawn only from joint studies of hydrographic observations and satellite data.

Unfortunately no sea-truth data were available, coincident with the analysed NOAA-AVHRR images. A well-coordinated field experiment (combining *in situ* and remote sensing imagery) is needed for further analysis of the generation, growth, and decay of fronts and eddies in this region. In the next chapter, the dynamical processes that could be responsible for the generation of currents, meanders and eddies are studied using a three-dimensional primitive equation, regional ocean circulation model of the West Greenland.

Chapter 6

Modelling mesoscale circulation features of the West Greenland Current

Fronts are a common feature in the oceans, both over the continental shelf and in the deep ocean (Simpson, 1981; Stommel, 1966). They often exhibit transient wavelike or meandering motions, which can grow to large amplitude and eventually pinch off to form rings or eddies. These processes have been observed in laboratory models (Griffiths and Linden 1982; Stern *et al.*, 1982) where instabilities often develop at the front, and in the ocean (Pingree, 1978). In chapter 5, we presented a detailed description of the spatial and temporal characteristics of the mesoscale circulation features observed in the West Greenland Current using NOAA-AVHRR infrared images. Earlier attempts to model the meandering process were based on linear stability analysis (Killworth, 1983; Killworth *et al.*, 1984; Ikeda *et al.*, 1984a) and using quasi-geostrophic equations (Ikeda, 1981 ; Ikeda and Apel, 1981; Holland, 1978; Holland *et al.*, 1983). The studies using quasi-geostrophic equations provide important insights, but they preclude surface fronts and the primitive equations are necessary for a full dynamical description of frontal meanders. In this chapter, a three-dimensional primitive equation regional model that covers the waters off the coast of West Greenland is used to study the combined effects of wind and thermal

forcings on the generation of current meanders and eddies.

6.1 Model Description

The model used in this study is a three dimensional primitive equation model based on the pioneering work of Bryan (1969) in the latest version (NOAA Geophysical Fluid Dynamics Laboratory (GFDL) Modular Ocean Model (MOM2) - version 2) described by Pacanowski (1996). The model is governed by the Navier-Stokes equations on a β plane subject to Boussinesq, hydrostatic and rigid lid approximations along with a nonlinear equation of state which couples two active tracers, temperature and salinity, to the fluid velocity. The Boussinesq approximation assumes that the density is spatially uniform unless it is multiplied by gravitational acceleration. This approximation is justified on the basis of the relatively small variations in density within the ocean. The hydrostatic approximation implies that the vertical pressure gradients are due only to density, and is justified when the horizontal scales are much larger than the vertical scales. The rigid lid approximation includes pressure variations at the upper surface, but excludes the kinematic effects of surface variations (Gill, 1982). This approximation filters out external gravity waves which place a severe limitation on solving the equations numerically. The governing equations are:

$$u_t + \nabla \cdot (uV) - fv = -(p_x/\rho_0) + A_m \nabla^2 u + (k_m u_z)_z \quad (6.1)$$

$$v_t + \nabla \cdot (vV) + fu = -(p_y/\rho_0) + A_m \nabla^2 v + (k_m v_z)_z \quad (6.2)$$

$$T_t + \nabla \cdot (TV) = \nabla \cdot (A_h \nabla T) + (k_h T_z)_z \quad (6.3)$$

$$S_t + \nabla \cdot (SV) = \nabla \cdot (A_h \nabla S) + (k_h S_z)_z \quad (6.4)$$

$$\nabla \cdot V = 0 \quad (6.5)$$

$$p_z = -\rho \cdot g \quad (6.6)$$

$$\rho = \rho(T, S, P) \quad (6.7)$$

where $\nabla = (\hat{i}\partial/\partial x, \hat{j}\partial/\partial y, \hat{k}\partial/\partial z)$. In the above equations u , v , P , T , S and t denote the zonal x and meridional y velocities, pressure, temperature, salinity and time respectively. V is the three dimensional velocity field, including the vertical z motion. Subscripts x , y , z and t denote partial differentiation with respect to the appropriate parameter. The Coriolis parameter f is allowed to vary with latitude as $f = f_o + \beta y$, where f_o is the Coriolis parameter taken at the latitude of the southern end of the model domain, $\beta = \partial f/\partial y$ and positive y -direction represents north; g , ρ and ρ_0 are the acceleration due to gravity, potential density and a reference density respectively. k_m and k_h are vertical eddy viscosity and diffusivity coefficients (m^2s^{-1}), A_m and A_h are horizontal eddy viscosity and diffusivity coefficients (m^2s^{-1}).

The boundary conditions at the surface ($z = 0$) of the model ocean are

$$\rho_0 k_m \frac{\partial}{\partial z}(u, v) = (\tau^x, \tau^y) \quad (6.8)$$

$$\rho_0 k_h \frac{\partial}{\partial z} (T, S) = (F^T, F^S) \quad (6.9)$$

$$w = 0 \quad (6.10)$$

where τ^x and τ^y are the zonal and meridional components of surface wind stress, respectively. In the case of temperature and salinity, either surface fluxes of heat and salinity (F^T, F^S) can be specified, or the temperature and salinity fields themselves may be specified at the surface. Equation (6.10) at the surface is called the rigid lid approximation, which filters out external gravity waves with no distortion of the steady-state ocean circulation and very little distortion of low-frequency motions. Since external gravity waves move rapidly compared to other types of disturbances, the removal of high speed waves allows a longer time step in solving the equations numerically.

At the ocean bottom ($z = -H$), the boundary conditions are as follows:

$$\rho_0 k_m \frac{\partial}{\partial z} (u, v) = 0 \quad (6.11)$$

$$\rho_0 k_h \frac{\partial}{\partial z} (T, S) = 0 \quad (6.12)$$

$$w = -u \frac{\partial H}{\partial x} - v \frac{\partial H}{\partial y}. \quad (6.13)$$

In equations 6.11 and 6.12, the vertical fluxes of momentum, heat and salt are taken to be zero, and equation 6.13 implies the velocity at the ocean bottom is required to parallel the slope. The boundary conditions at the lateral walls (boundaries) on velocity,

temperature and salinity are,

$$u, v, T_n, S_n = 0 \quad (6.14)$$

where subscript n denotes a local derivative with respect to the coordinate normal to the wall.

Equations (6.1) - (6.7) constitute a closed system of seven scalar equations and seven unknowns, u, v, w, T, S, p and ρ . The variables u, v, T , and S are prognostic variables whose time rates of change are predicted from equations (6.1) - (6.4) respectively. Although, the diagnostic variables w, p , and ρ can be determined from equations (6.5) - (6.7) respectively, the choice of the rigid lid boundary condition imposes additional constraints on p and w . The vertically integrated pressure can no longer be obtained by integrating the hydrostatic equation (6.6) for the free surface. Further, the vertically integrated horizontal velocity is constrained to be nondivergent. Integrating the continuity equation (6.5) with respect to z ,

$$w(0) - w(-H) = - \int_{-H}^0 \left(\frac{\partial u}{\partial x} + \frac{\partial v}{\partial y} \right) dz + u(-H) \frac{\partial H}{\partial x} + v(-H) \frac{\partial H}{\partial y} \quad (6.15)$$

and applying the vertical boundary conditions equations (6.10) and (6.13) we get

$$\int_{-H}^0 \left(\frac{\partial u}{\partial x} + \frac{\partial v}{\partial y} \right) dz = 0 \quad (6.16)$$

For any quantity \mathbf{u} , let its vertical average be denoted by \bar{u} and its departure from the mean (vertical shear) be denoted by u' . From equation (6.16), the vertically averaged

components (\bar{u}, \bar{v}) can be written in terms of a volume transport stream function ψ for the vertically integrated flow:

$$\bar{u} = \frac{1}{H} \int_{-H}^0 u dz = -\frac{1}{H} \frac{\partial \psi}{\partial y} \quad (6.17)$$

$$\bar{v} = \frac{1}{H} \int_{-H}^0 v dz = \frac{1}{H} \frac{\partial \psi}{\partial x} \quad (6.18)$$

A prediction equation for the volume transport stream function ψ which does not include the unknown surface pressure is obtained by forming vertical averages of equations (6.1) and (6.2) and taking curl of the these and using (6.17) and (6.18)

$$\begin{aligned} \frac{\partial}{\partial t} \left[\frac{1}{H} \left(\frac{\partial^2 \psi}{\partial x^2} \right) + \frac{1}{H} \left(\frac{\partial^2 \psi}{\partial y^2} \right) + \frac{\partial \psi}{\partial x} \frac{\partial H^{-1}}{\partial x} + \frac{\partial \psi}{\partial y} \frac{\partial H^{-1}}{\partial y} \right] = & - \left[\frac{\partial}{\partial x} \left(\frac{f}{H} \frac{\partial \psi}{\partial y} \right) - \frac{\partial}{\partial y} \left(\frac{f}{H} \frac{\partial \psi}{\partial x} \right) \right] \\ & - \left[\frac{\partial}{\partial x} \left(\frac{g}{H \rho_0} \int_{-H}^0 \int_z \frac{\partial \rho}{\partial y} dz' dz \right) - \frac{\partial}{\partial y} \left(\frac{g}{H \rho_0} \int_{-H}^0 \int_z \frac{\partial \rho}{\partial x} dz' dz \right) \right] \\ & + \frac{\partial}{\partial x} \left(\frac{1}{H} \int_{-H}^0 G dz \right) - \frac{\partial}{\partial y} \left(\frac{1}{H} \int_{-H}^0 F dz \right) \end{aligned} \quad (6.19)$$

where G and F represent the collected contributions of the nonlinear and viscous terms in (6.1) and (6.2). The vertical shear current (u', v') is predicted from equations (6.1) and (6.2) after subtracting the vertical mean. The equations are

$$\frac{\partial u'}{\partial t} = \frac{-1}{\rho_0} \frac{\partial p'}{\partial x} + f v' + A_M \nabla^2 u' + k_m \frac{\partial^2 u'}{\partial z^2} + F - \bar{F} - \frac{\tau^x}{\rho_0 H} \quad (6.20)$$

$$\frac{\partial v'}{\partial t} = \frac{-1}{\rho_0} \frac{\partial p'}{\partial y} - f u' + A_M \nabla^2 v' + k_m \frac{\partial^2 v'}{\partial z^2} + G - \bar{G} - \frac{\tau^y}{\rho_0 H} \quad (6.21)$$

In equations (6.20) and (6.21), p' , which represents the departure from the vertical average, is expressed in terms of ρ using equation (6.6) as

$$p' = \int_z^0 \rho g dz' - \frac{1}{H} \int_{-H}^0 \left(\int_z^0 \rho g dz' \right) dz \quad (6.22)$$

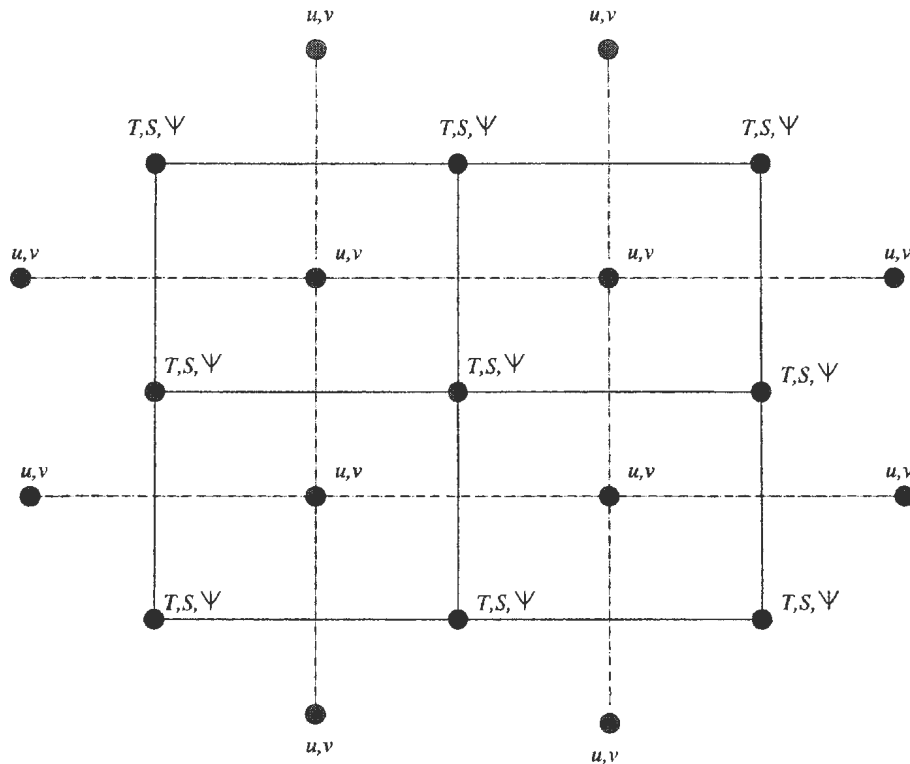


Figure 6.1: The arrangement of variables in the horizontal plane for a grid with equal grid spacing in both directions.

where z' is a dummy variable representing vertical coordinate.

The method of solution consists of predicting the variables ψ , u' , v' , T and S from equations (6.19), (6.20), (6.21), (6.3) and (6.4), respectively. The total current is then obtained by adding the vertical average part to the vertical shear part after the former is obtained from ψ using equations (6.17) and (6.18). The variables ρ , w and p' are obtained from equations (6.7), (6.16), and (6.22), respectively. The prediction equations are solved by dividing the ocean into a three dimensional lattice of rectangularly shaped cells of arbitrary size, discretizing the equations within each cell, and solving all equations

by finite difference techniques. The finite difference grid used is the Arakawa-B type, in which tracer points T , S and stream function points ψ are placed in the center of the cells and the horizontal velocity components u and v are situated at the corners. The arrangement of variables in the horizontal plane is shown in Fig. 6.1. In the vertical, T , S , u and v are located in the center of the cell. The details of the finite difference formulation and time stepping method of the prediction equations will not be described here, for a detailed description on this technique see Bryan (1969), Semtner (1986) and Pacanowski (1996).

6.2 Numerical Experiments

In this section, the details and the results of the numerical experiments performed to elucidate the dynamical processes involved in modelling the current meanders and eddies are described. As the model (MOM2) chosen for the study is the latest version, first a numerical experiment was carried out to test and verify the satisfactory behaviour of the model to chosen initial and open boundary conditions. Next, a numerical experiment was carried out to study the combined effects of wind and thermal forcings on the generation of current meanders and eddies.

6.2.1 Experiment 1: Test Case Run

The experimental set up for the test case experiment was motivated by the work of Hsieh and Gill (1984) and Stevens (1990). The model domain extends from 42° W to

60° W in longitude and 57° N to 67° N in latitude (centred at 62° N), with eastern and western boundaries closed and northern and southern boundaries open. This area roughly represents the waters off the coast of West Greenland. A rectangular flat-bottomed ocean with constant depth (2700 m) is used for this experiment. The grid size is $1/6^\circ$ in the zonal direction and $1/6^\circ$ in the meridional direction, giving a grid spacing of about 9 km and 18 km in the east-west and north-south directions respectively at 62° N. In the vertical there are 6 levels, the grid size varies from 50 m at the surface to 900 m at the bottom and the time step is 900 seconds. The horizontal mixing coefficients A_m and A_h are chosen to be $10^4 \text{ m}^2\text{s}^{-1}$ and $500 \text{ m}^2\text{s}^{-1}$ respectively and the vertical mixing coefficients k_m and k_h are both chosen to be $10^{-4} \text{ m}^2\text{s}^{-1}$. The large value of A_m is chosen for computational stability (see Bryan *et al.*, (1975) and Killworth *et al.*, (1984) for details) to inhibit the computational mode caused by centred differencing. No surface forcing is used in this experiment. At the open boundaries, a passive boundary condition (Stevens, 1990) is applied in which there is no forcing, and phenomena generated within the domain can propagate outward without disturbing the interior solution. The baroclinic velocities on the open boundaries are calculated using the linearized form of the horizontal momentum equations (6.1 and 6.2) with only the advective terms omitted. Heat and salt are advected out of the domain if the normal component of the velocity at the boundary is directed outward. Along the lateral boundaries (side walls), the no-slip and no flux of tracer conditions are applied. A simple Orlanski radiation condition (Orlanski, 1976) is applied to the the stream function solution. The model is started from rest, but the northern

Table 6.1: Temperature, salinity and density in the model domain.

Level	Depth metres	Southern half			Northern half		
		Temperature °C	Salinity	Density kgm ⁻³	Temperature °C	Salinity	Density kgm ⁻³
1	25	6.29	34.793	27.3518	1.99	32.769	26.1853
2	150	5.14	35.031	27.6836	5.59	34.870	27.5017
3	500	3.78	34.938	27.7598	4.47	34.930	27.6801
4	1100	3.15	34.901	27.7922	3.53	34.908	27.7610
5	1850	2.86	34.905	27.8222	3.01	34.867	27.7781
6	2700	2.80	34.977	27.8852	2.66	34.909	27.8433

and southern halves of the model domain are filled with fluid of different densities. The temperature and salinity data used are based on hydrographic observations collected in January 1995 off the coast of West Greenland (Chapter 2, Fig. 2.2) and obtained from the Institut für Seefischerei, Hamburg, Federal Republic of Germany. For the northern half of the model domain, the CTD data from the station (61° 30' N , 51° 6' W) of the Frederikshaab section is used, and for the southern half, the CTD data from the station (59° N , 45° 12' W) of the Cape Farewell section is used. The temperature, salinity and density profiles of both these stations are shown in Chapter 2 (Fig. 2.13), and their values at model levels in the vertical are outlined in Table. 6.1. It should be noted that the water is denser in the southern half than the northern half, and it is primarily due to the higher salinity values.

In modelling and observational studies of mesoscale processes such as current meanders, fronts and eddies, the Rossby radius of deformation is an important quantity in

the determination of the horizontal scales. The Rossby radius of deformation is a fundamental horizontal length scale in fluids that are affected by both gravity and rotation of the Earth. It is the length scale at which the rotation effects become as important as buoyancy effects. In transient problems with an initial disturbance at a scale small compared to the Rossby radius, the adjustment to equilibrium process is about the same as would occur in the nonrotating system. However, if the disturbance has a length scale comparable to the Rossby radius, the Coriolis acceleration becomes as important as the pressure gradient term and causes a response that is different from the non-rotating case. There are two types of Rossby radius: external or barotropic Rossby radius and internal or baroclinic Rossby radius. In a homogeneous layer of fluid the barotropic Rossby radius (L) is a function of depth and latitude, and is given by ($L = c/f$), where c is the gravity wave propagation speed (\sqrt{gH}), g is the acceleration due to gravity and H is the water depth. The baroclinic Rossby radius depends, in addition on vertical stratification and is similarly computed except that c is now wave speed of the n^{th} baroclinic mode as would be found in the normal mode decomposition of the system. The baroclinic Rossby radius is the natural scale in the ocean associated with boundary phenomena such as boundary currents, fronts and eddies. The first mode baroclinic radius is typically around 10-30 km in the ocean (Gill, 1982).

Both external and internal Rossby radii have been calculated and reported in the literature as parts of various regional and dynamical studies. For example, Emery *et*

al., (1984) have calculated the internal Rossby radius using temperature and salinity profiles for the North Atlantic and North Pacific, and according to them the internal Rossby radius of deformation of first mode decreases from approximately 75 km at 15° N to less than 10 km at 60° N in the central North Atlantic between 30° W and 40° W. Krauss *et al.*, (1990) studied the relationship between the Rossby radius and eddy scales in the Eastern and Northern North Atlantic between 35° N and 60° N using satellite infrared images and satellite tracked buoys, and suggested that the eddy scales decrease northward from the subtropical North Atlantic and that they were closely related to the Rossby radius of the first baroclinic mode. They also concluded that if the eddy field is produced by baroclinic instability, then the eddy size must be proportional to the Rossby radius.

In this study, the temperature and salinity profiles measured at (60°30' N, 51°6' W) of the Frederikshaab section are used to compute the potential density from which the internal Rossby radius was computed for the first baroclinic mode. The computed density profile at (60°30' N, 51°6' W) gives $\rho_1 = 1026.1 \text{ kgm}^{-3}$, $\rho_2 = 1027.3 \text{ kgm}^{-3}$ and H_1 (the thickness of the first layer) $\simeq 150 \text{ m}$, the internal Rossby radius for the top layer is,

$$L = \sqrt{\frac{(\rho_2 - \rho_1)gH_1}{\rho_2 f^2}} \simeq 11 \text{ km} \quad (6.23)$$

where g is the acceleration due to gravity and $f = 1.2 \times 10^{-4} \text{ s}^{-1}$ is the Coriolis parameter. The Rossby radius value obtained here falls within the range of 10 - 30 km suggested by Gill, (1982) for the first baroclinic mode.

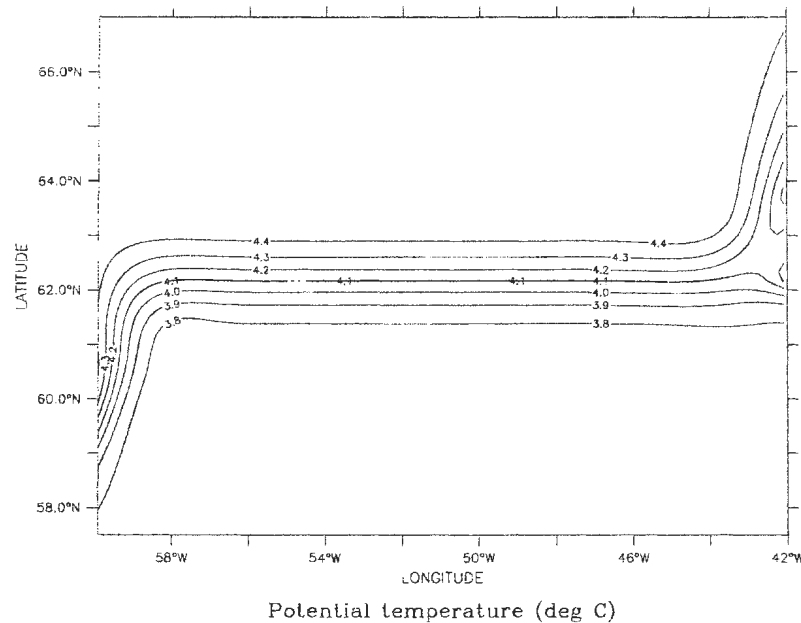


Figure 6.2: Level 3 (500 m) temperature after 23 days.

The grid spacing chosen for the experiment is 9 km in the zonal direction and 18 km in the meridional direction, thus resolving the Rossby radius in the zonal direction. According to Hsieh and Gill (1984) the finite difference effect due to the grid spacing larger than the baroclinic Rossby radius (L), together with the large values of A_m and A_h chosen for computational stability leads to a baroclinic Kelvin wave with a much greater width than L and a much lower phase speed. Davey *et al.*, (1983) and Hsieh *et al.*, (1983) have studied the effects of lateral and vertical viscosity on the Kelvin wave and the behaviour of the Kelvin wave in finite-difference models respectively. To illustrate

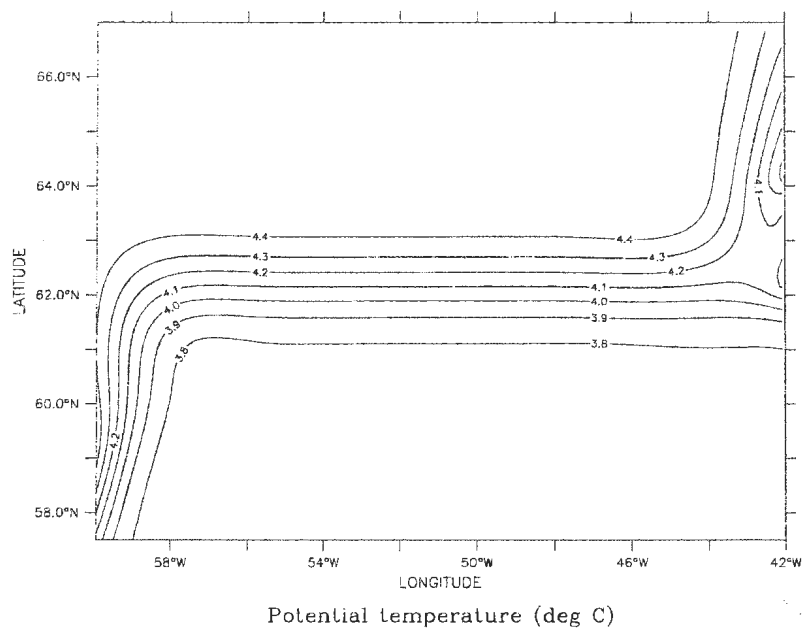


Figure 6.3: Level 3 (500 m) temperature after 53 days.

results and the behaviour of the model, the temperature field at level 3 (500 m) after 23 and 53 days of model run are shown in Fig. 6.2 and Fig. 6.3 respectively. Also the velocity fields at level 1 (25 m) and at level 5 (1850 m) at the end of 23 days are shown in Fig. 6.4 and Fig. 6.5 respectively. The presence of coastally trapped Kelvin waves can be seen in these figures. The velocity vectors (Fig. 6.4 and Fig. 6.5) show that the direction of velocity at level 5 is opposite to the direction at level 1, indicating the waves are baroclinic. The baroclinic Kelvin waves, one travelling north along the eastern boundary and another travelling south along the western boundary should be able to propagate out

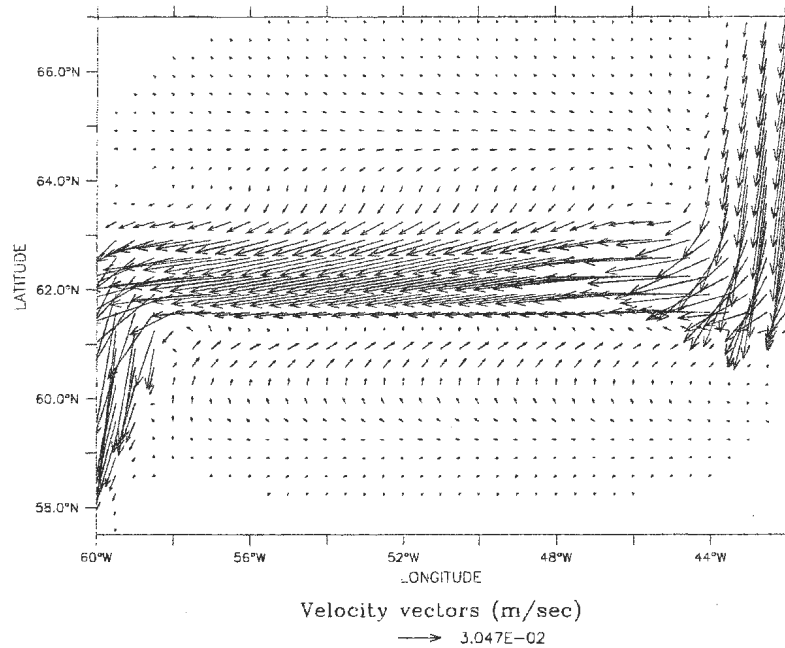


Figure 6.4: Velocity vectors at level 1 (25 m) at the end of 23 days.

of the region without being reflected or modified according to the chosen passive open boundary condition. Fig. 6.2 shows the front of the Kelvin wave about reach the open boundaries of the model domain. After 53 days (Fig. 6.3), the Kelvin wave appear to have successfully passed through the open boundaries of the model. As the aim of carrying out this numerical experiment is to learn the setup, test and verify the behaviour of the model to the chosen initial and boundary conditions and to elucidate the importance of the Rossby radius in modelling the mesoscale features, the adjustment to equilibrium will not be explored here. For a detailed study of the Rossby adjustment problem in a

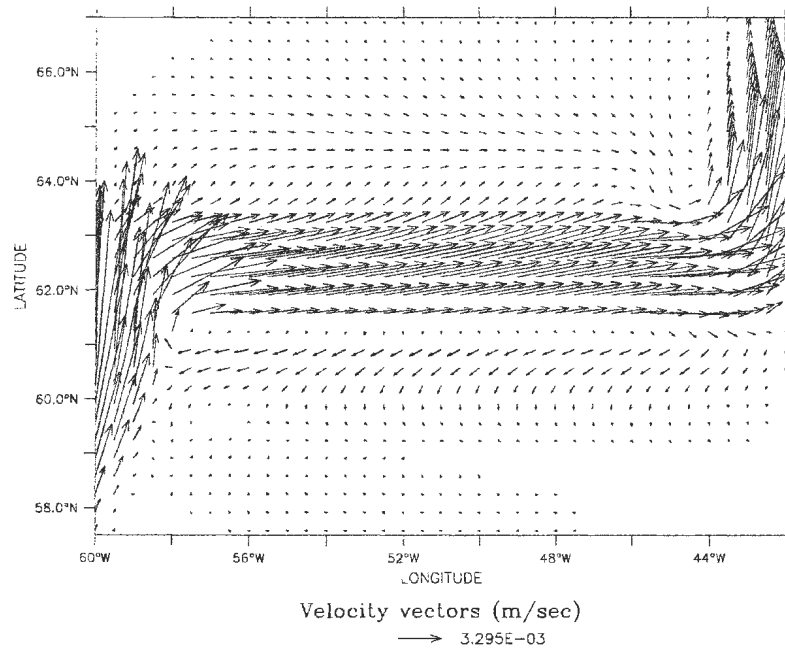


Figure 6.5: Velocity vectors at level 5 (1850 m) at the end of 23 days.

rotating stratified channel with and without topography, the reader can refer to Hsieh and Gill (1984).

6.2.2 Experiment 2: Role of wind and thermal forcings in the generation of current meanders and eddies

In this section, the results of the numerical experiment carried out to investigate the effects of wind and thermal forcings in the generation of current meanders and eddies are presented. The model domain extends from 45° W to 60° W in longitude and 57° N to 67° N in latitude (centred at 62° N), with eastern and western boundaries closed and

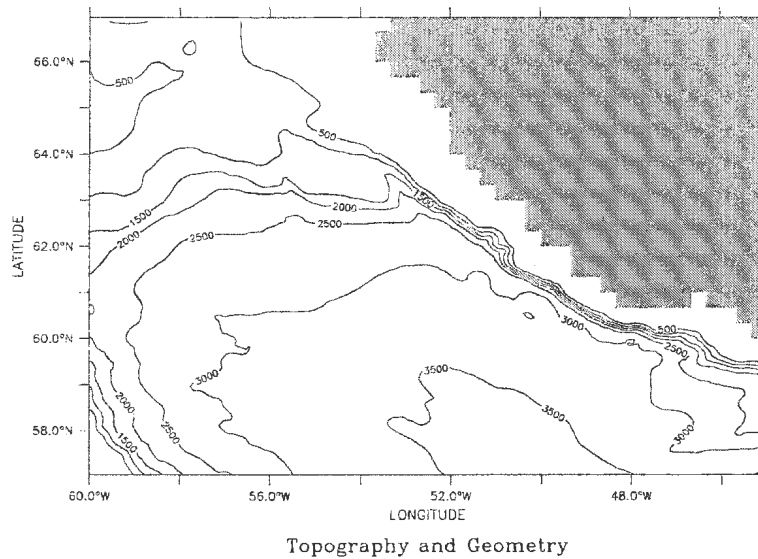


Figure 6.6: ETOPO5 bottom topography (depth in metres).

northern and southern boundaries open, and uses the realistic ETOPO5 (Fig. 6.6) bottom topography. The grid size is $1/12^\circ$ in the zonal direction and $1/12^\circ$ in the meridional direction, giving a resolution of about 5 km and 9 km respectively, adequate to resolve the internal Rossby radius of deformation in both directions. The surface wind forcing (Fig. 6.7a) and thermal forcing (Fig. 6.7b) are based on the zonal averages of annual means of Hellerman and Rosenstein (1983) and Levitus (1982) data respectively. The model is started at rest with an idealized temperature distribution depending on latitude and depth based on the zonal averages of annual means from the Levitus (1982) data. A constant salinity value of 34.9 is maintained throughout the experiment. All other model

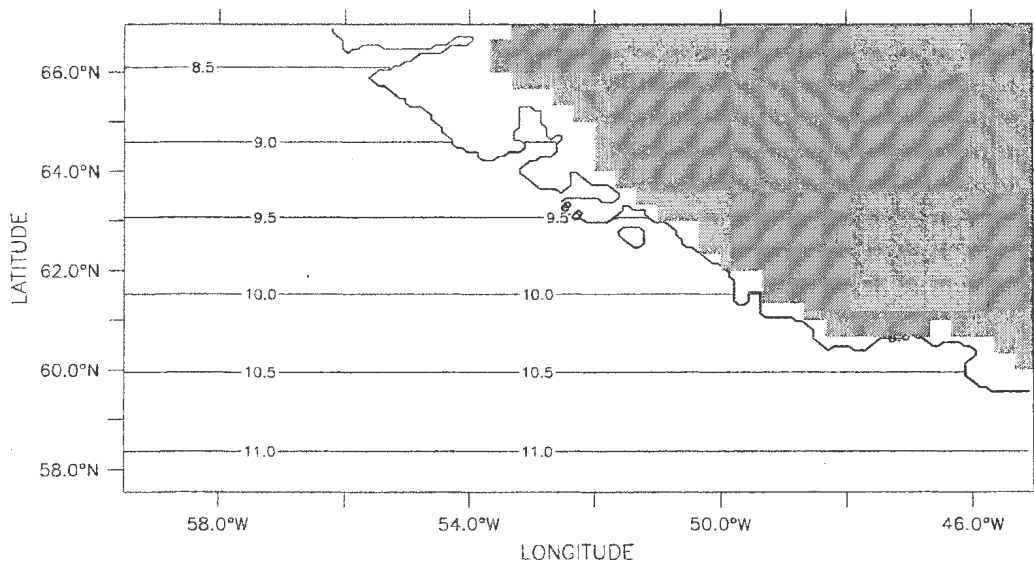
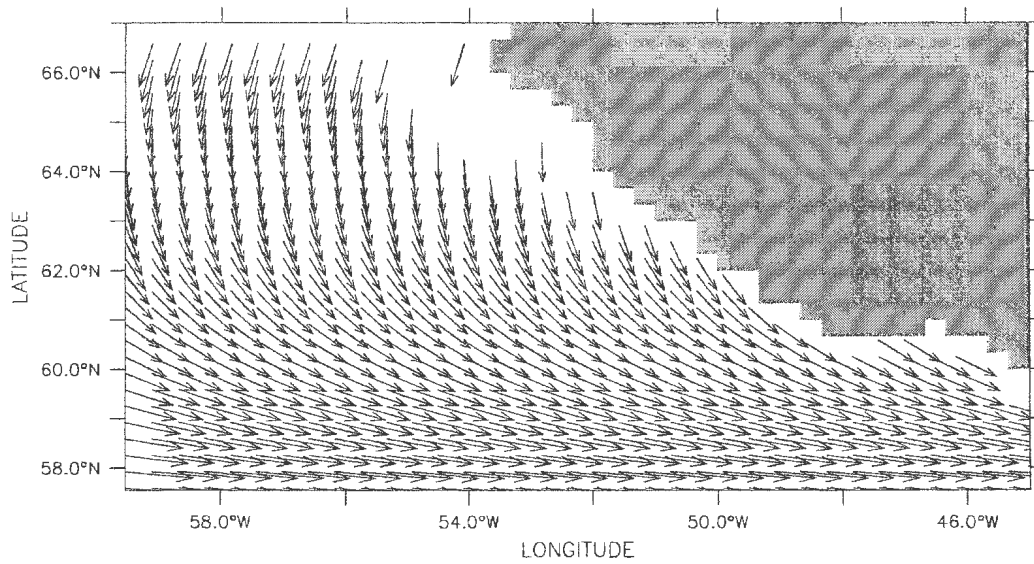
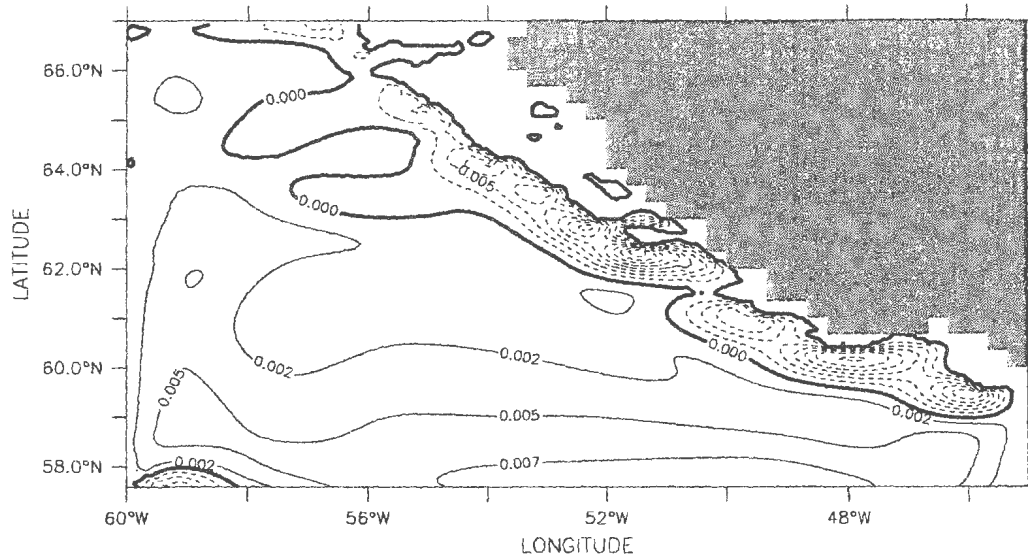
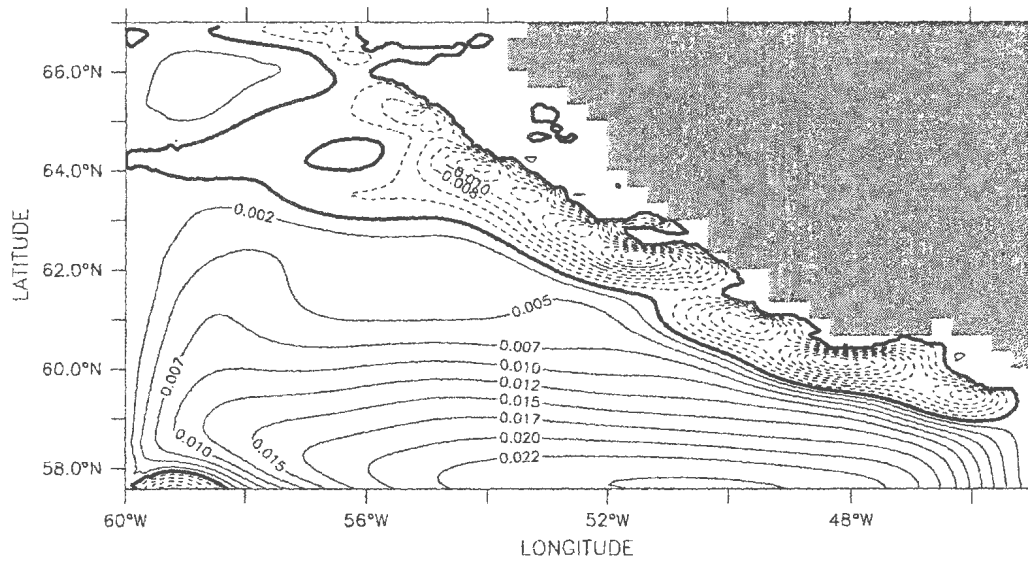


Figure 6.7: (a) Wind forcing and (b) The initial field of surface temperature used in this experiment.

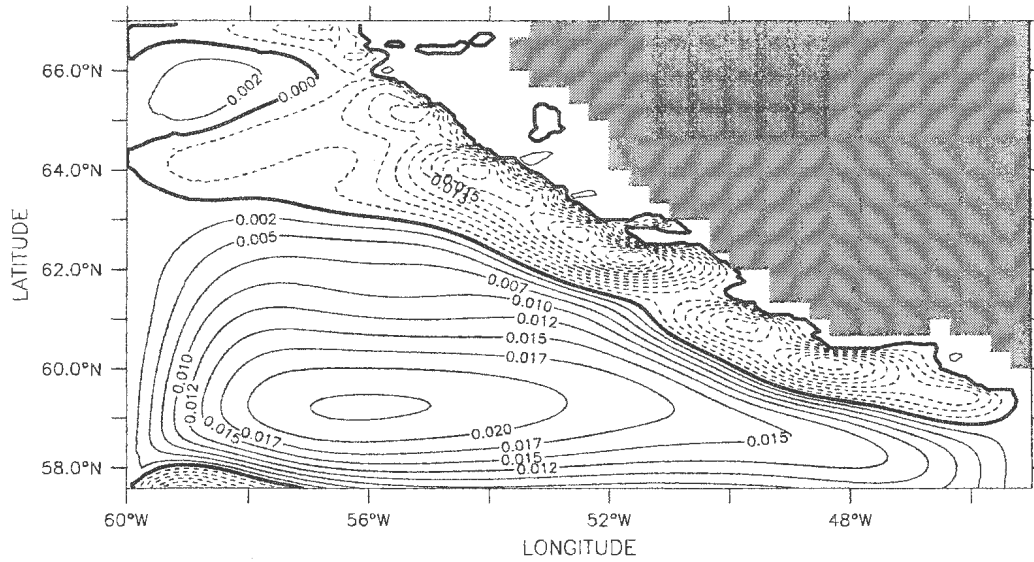


Zonal velocity (m/sec) after 5 days

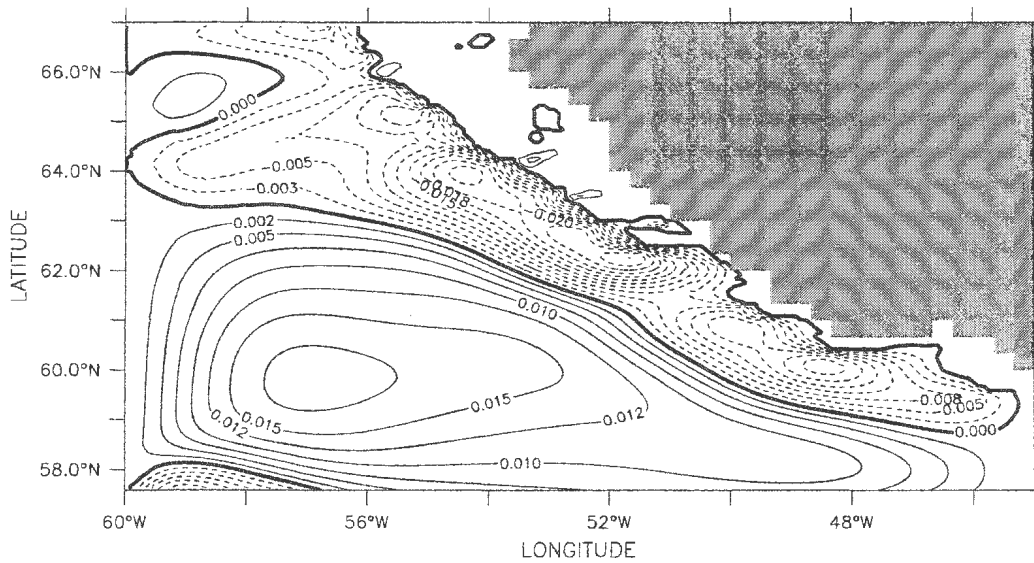


Zonal velocity (m/sec) after 10 days

Figure 6.8: Zonal velocity contours at level 1 (25 m) after 5 and 10 days of model run.

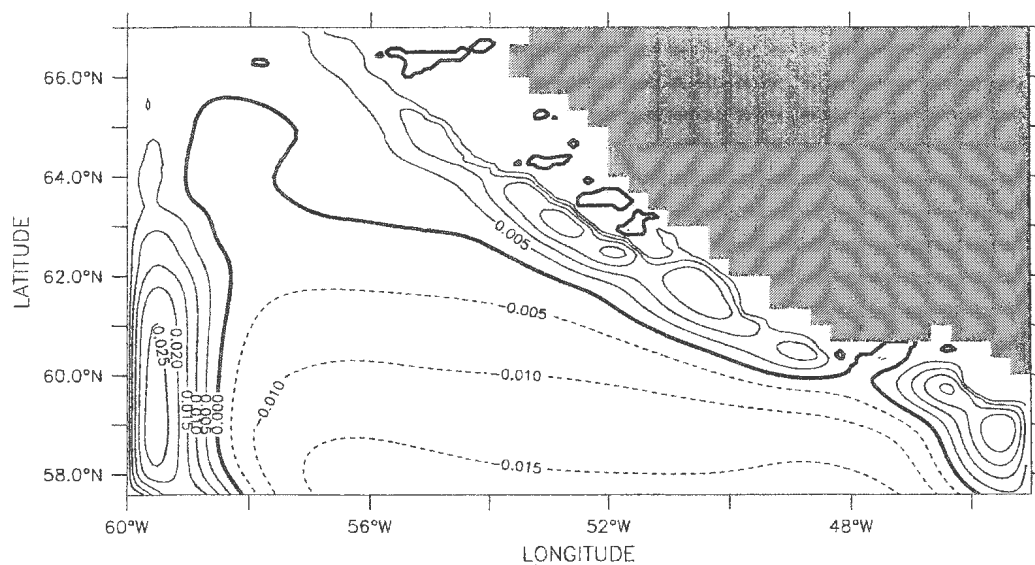


Zonal velocity (m/sec) after 20 days

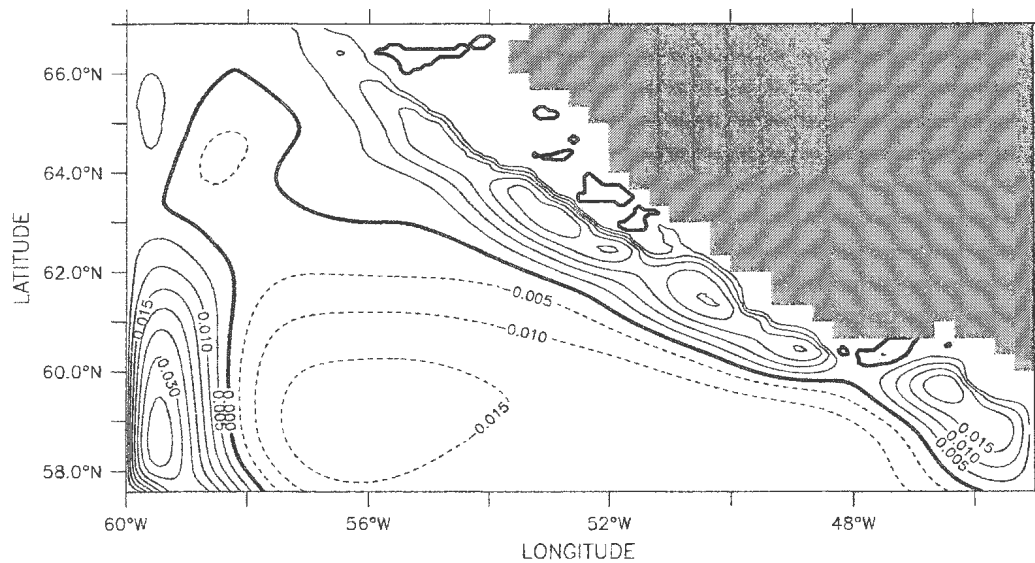


Zonal velocity (m/sec) after 30 days

Figure 6.9: Zonal velocity contours at level 1 (25 m) after 20 and 30 days of model run.

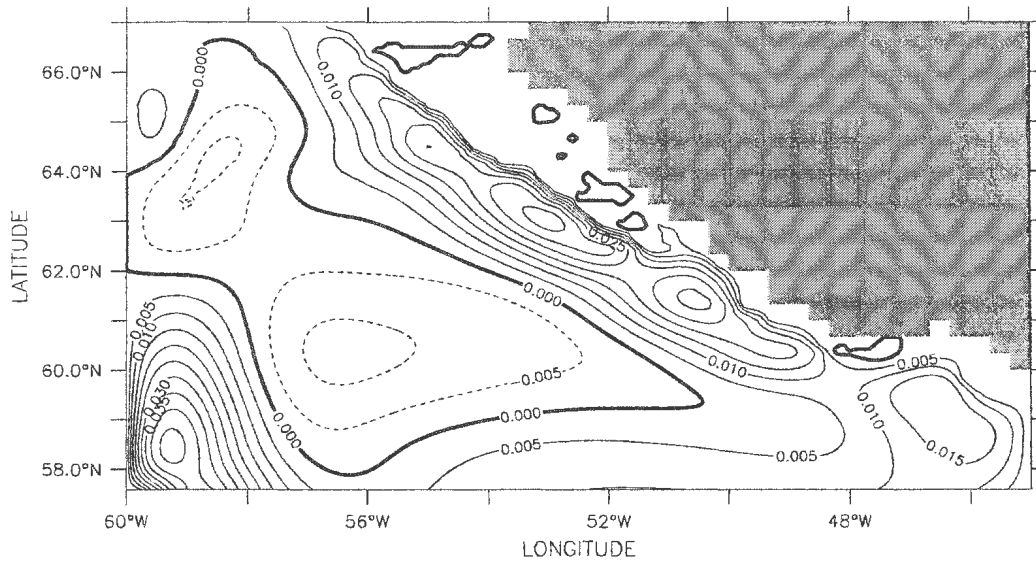


Meridional velocity (m/sec) after 5 days

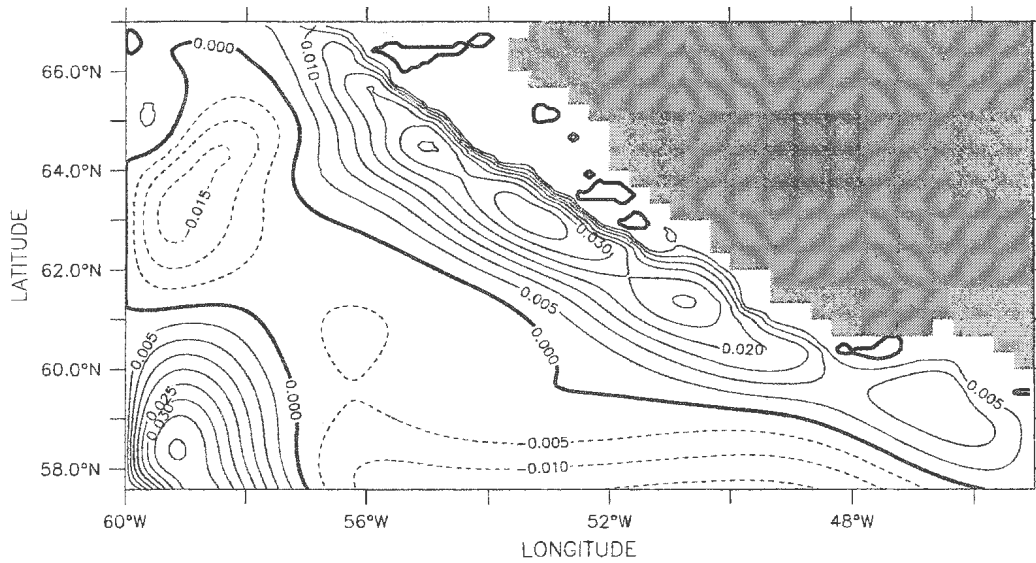


Meridional velocity (m/sec) after 10 days

Figure 6.10: Meridional velocity contours at level 1 (25 m) after 5 and 10 days of model run.

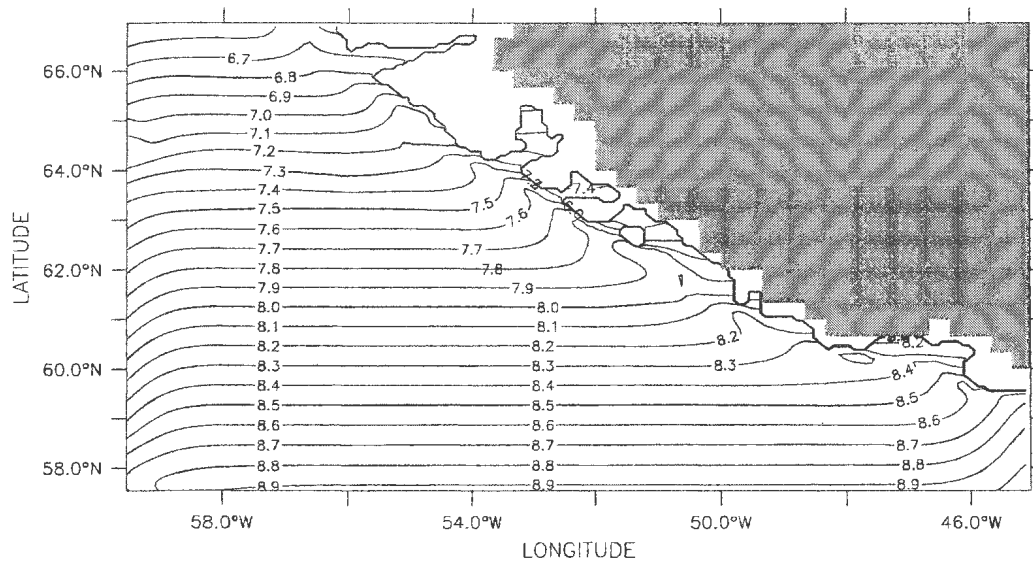


Meridional velocity (m/sec) after 20 days

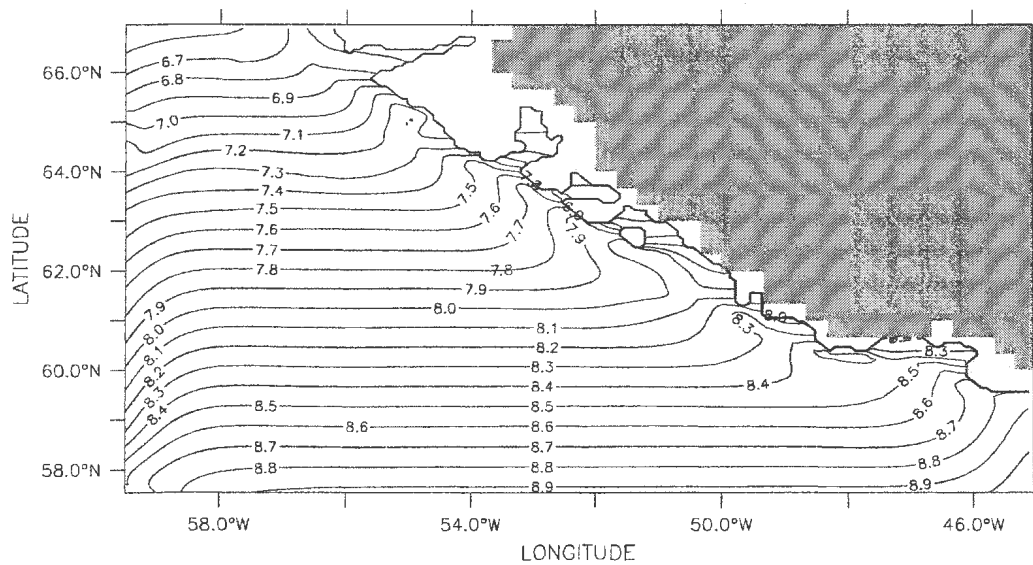


Meridional velocity (m/sec) after 30 days

Figure 6.11: Meridional velocity contours at level 1 (25 m) after 20 and 30 days of model run.

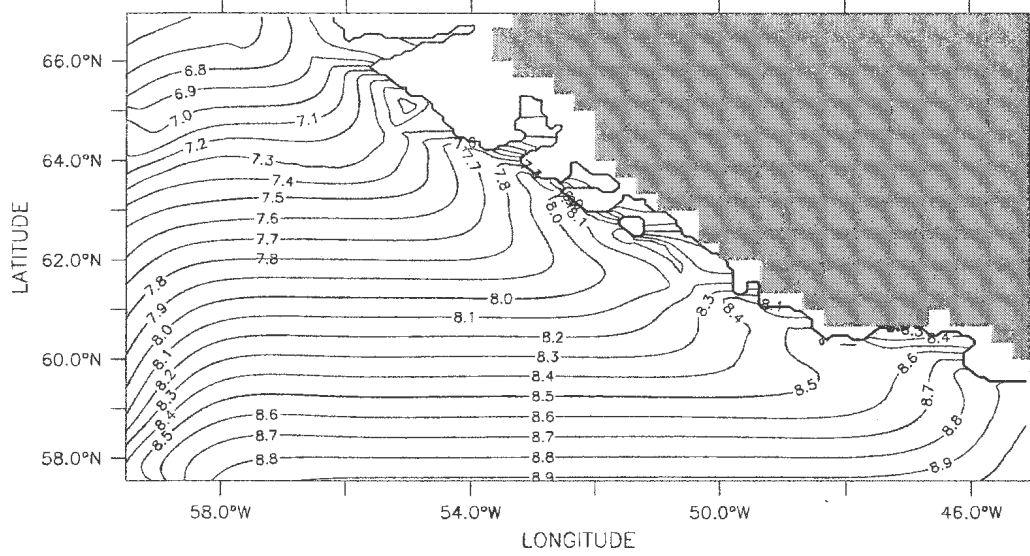


Potential temperature (deg C) after 5 days

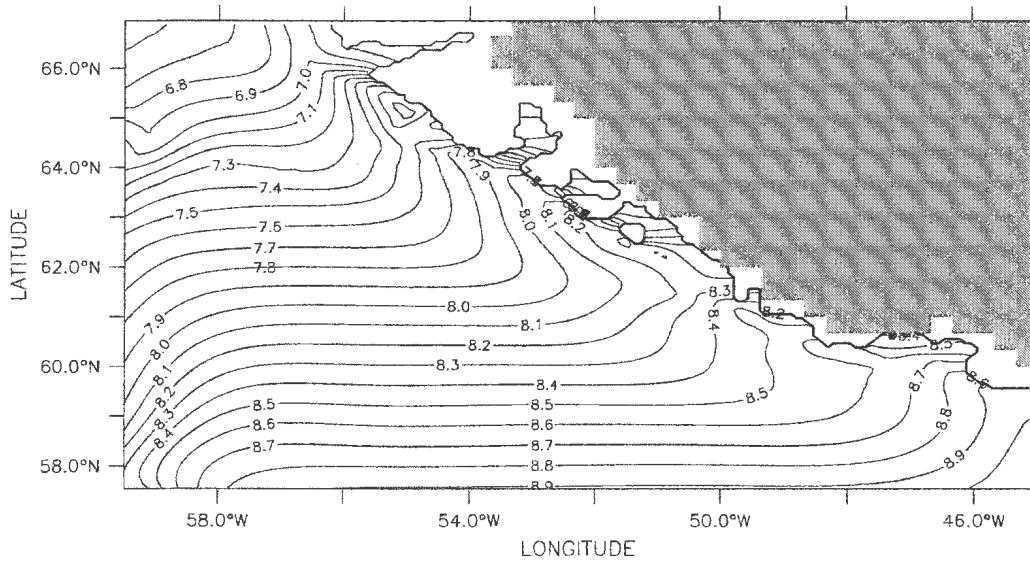


Potential temperature (deg C) after 10 days

Figure 6.12: Temperature contours at level 2 (150 m) after 5 and 10 days of model run.



Potential temperature (deg C) after 20 days

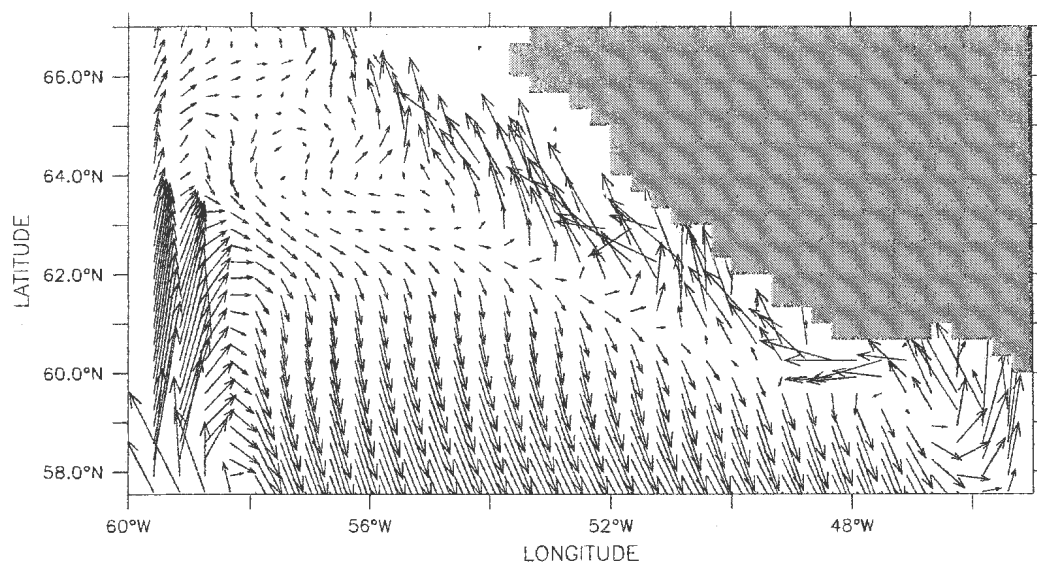


Potential temperature (deg C) after 30 days

Figure 6.13: Temperature contours at level 2 (150 m) after 20 and 30 days of model run.

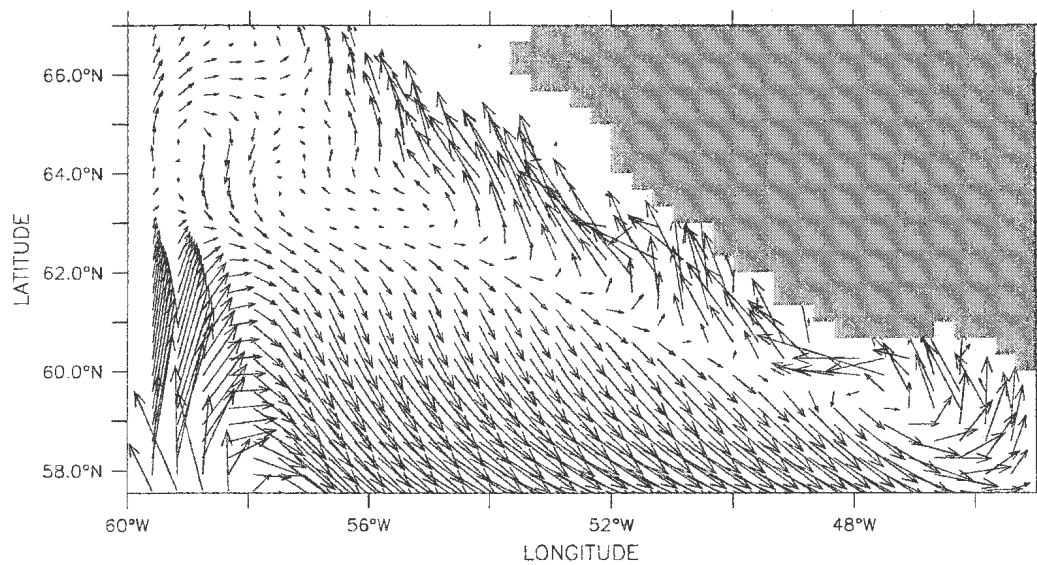
parameters and the open boundary conditions used in this experiment are the same as those used in the experiment 1.

A time sequence of the fields of zonal (u) and meridional (v) velocity components, and temperature field is shown in Figs. 6.8 - 6.13. The wind and thermal forcings (Fig. 6.7a and Fig. 6.7b) used in this experiment are expected to lead to different dynamical responses. The thermal forcing (temperature gradient) establishes coastally trapped Kelvin waves, and the presence of these waves is evident in the Figs. 6.12 - 6.15. The waves are baroclinic, as the velocity at level 1 (25 m, Fig. 6.14 and Fig. 6.15) is opposite to the direction at level 5 (1850 m, not shown). The waves propagate out of the model domain without being reflected or modified. After the passage of the Kelvin wave front a steady poleward flowing coastal current is established. The current advects warm water from the south of the model domain (Fig. 6.12 and Fig. 6.13), and is continually augmented by additional onshore flow. Although the coastal poleward current velocities are maintained throughout the experiment, offshore of the coastal flow in the southern half of the model domain there is a region of southward flow discernible in Fig. 6.14. This is attributable to the eastward (onshore) component of wind forcing (Fig. 6.7a), according to the Ekman theory their effect on the surface current transport mass southward. In the northern end of the model domain, the flow in the offshore region is more complex (Fig. 6.14). Regions of onshore and offshore flow that could be seen are due to the combined effects of wind and thermal forcing, and the closed western boundary. In time, in the southern end of the model domain, the current driven by thermal gradient opposes the



Velocity vectors (m/sec) after 5 days

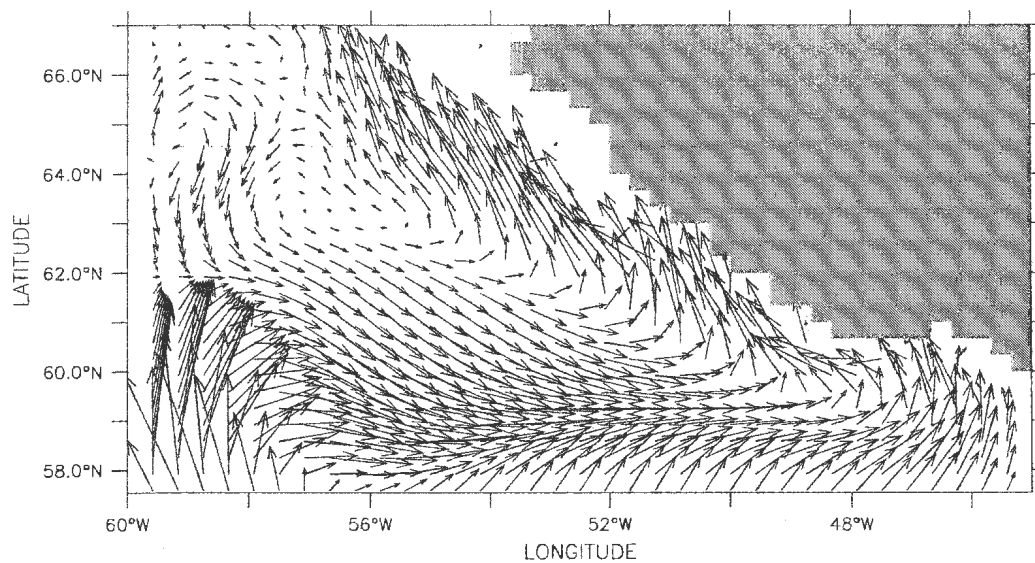
→ $1.157E-02$



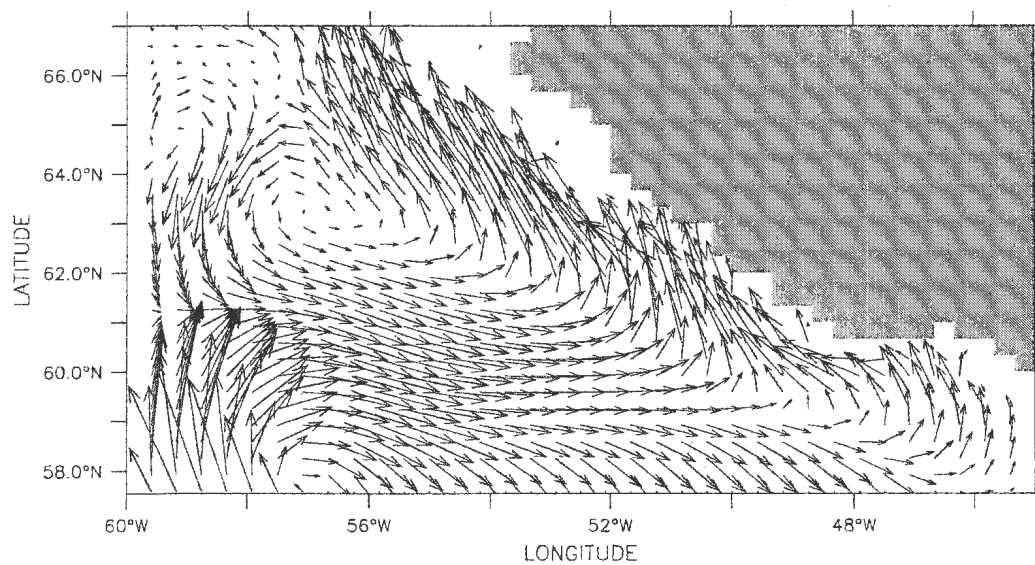
Velocity vectors (m/sec) after 10 days

→ $1.711E-02$

Figure 6.14: Velocity vectors at level 1 (25 m) after 5 and 10 days of model run.

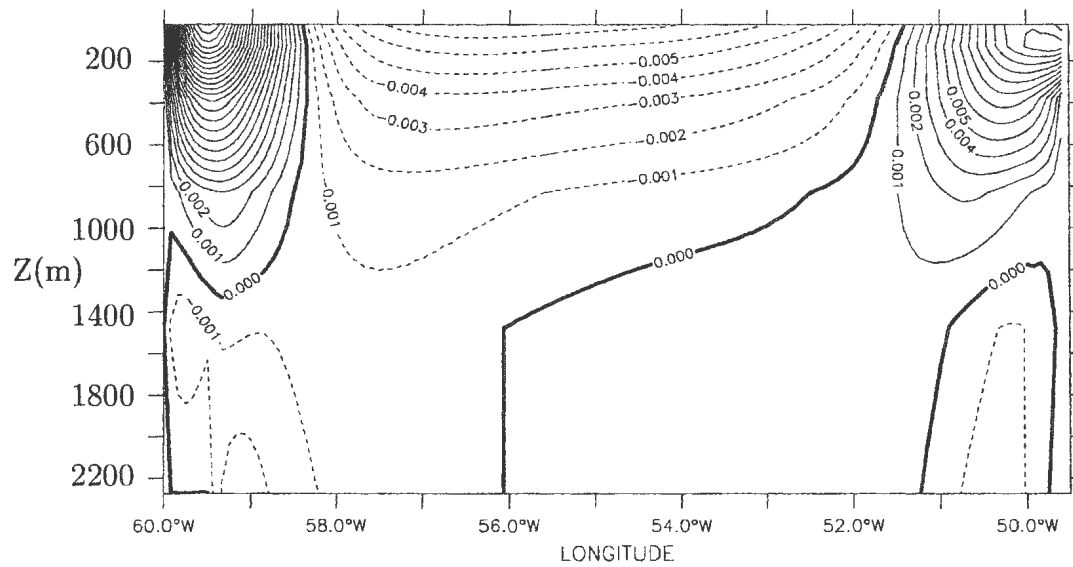


Velocity vectors (m/sec) after 20 days
→ 1.819E-02

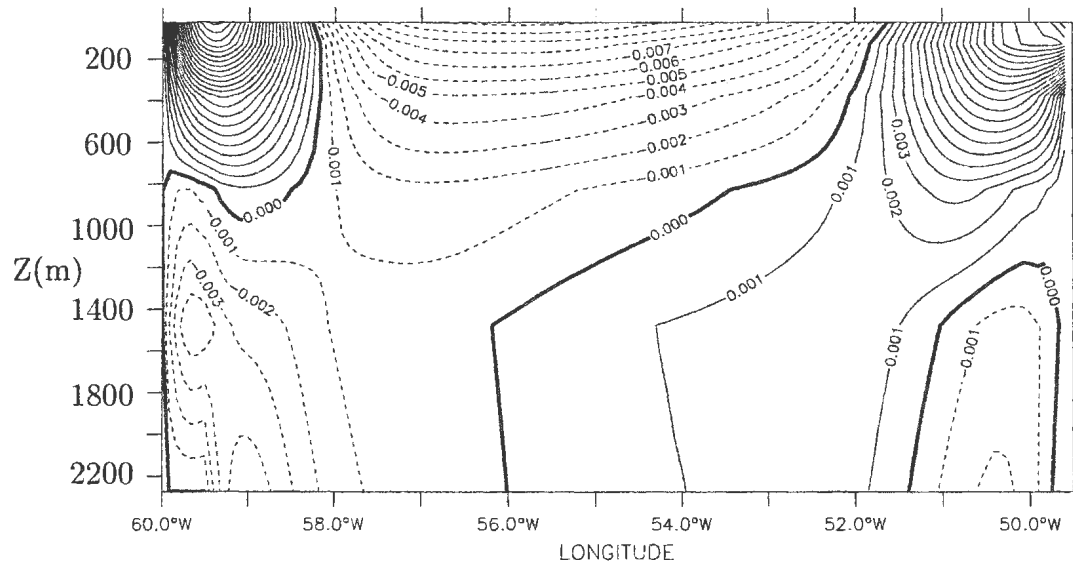


Velocity vectors (m/sec) after 30 days
→ 1.783E-02

Figure 6.15: Velocity vectors at level 1 (25 m) after 20 and 30 days of model run.

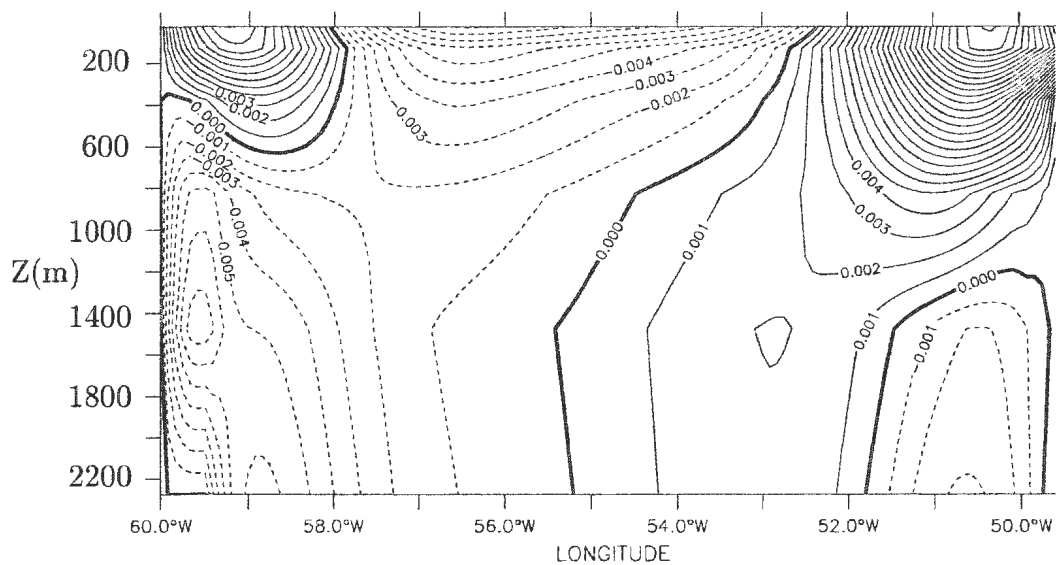


Vertical section of meridional velocity (m/sec) after 5 days

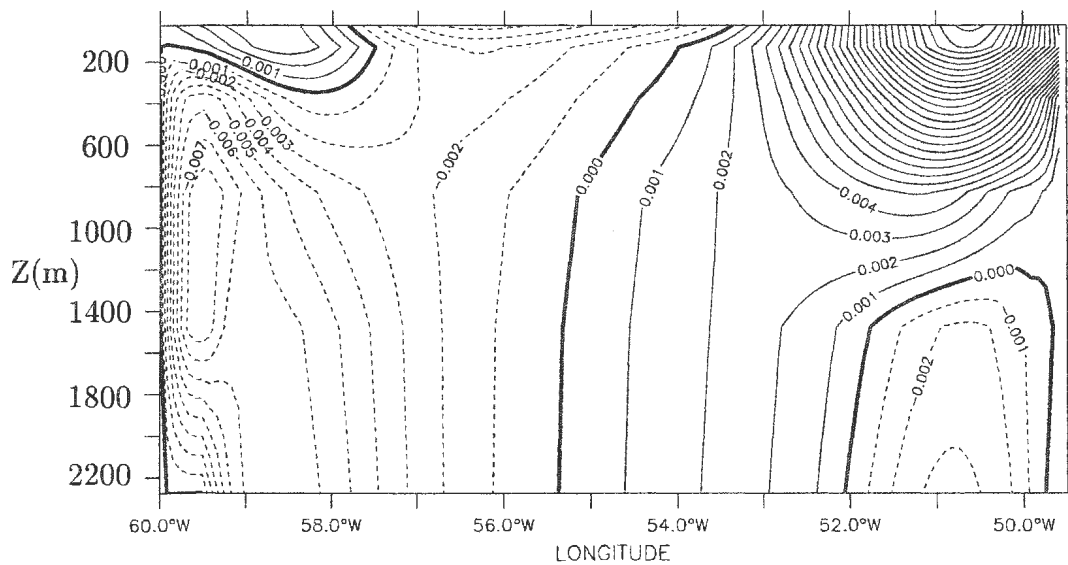


Vertical section of meridional velocity (m/sec) after 10 days

Figure 6.16: Vertical section of meridional velocity at 61° N after 5 and 10 days of model run.

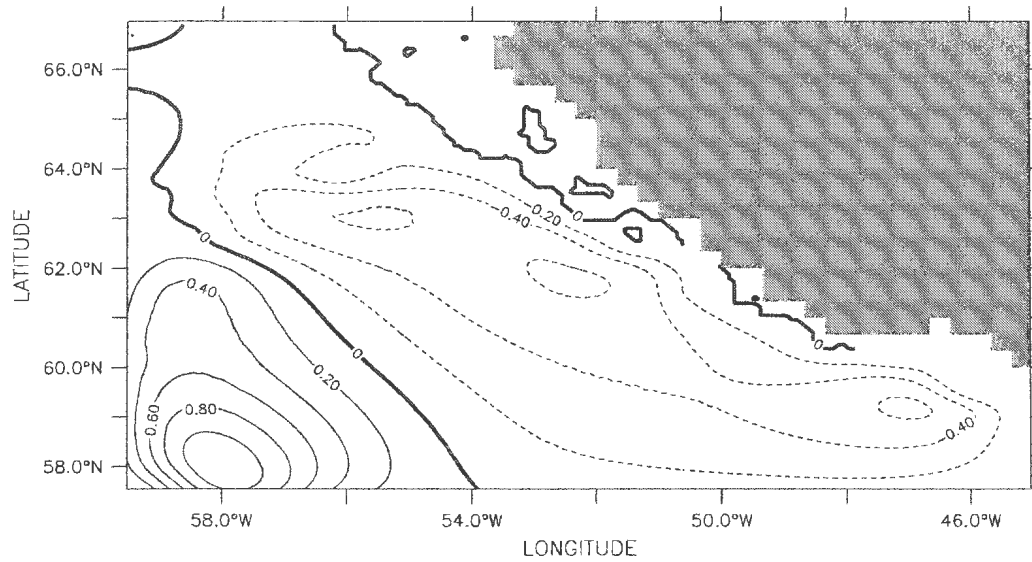


Vertical section of meridional velocity (m/sec) after 20 days

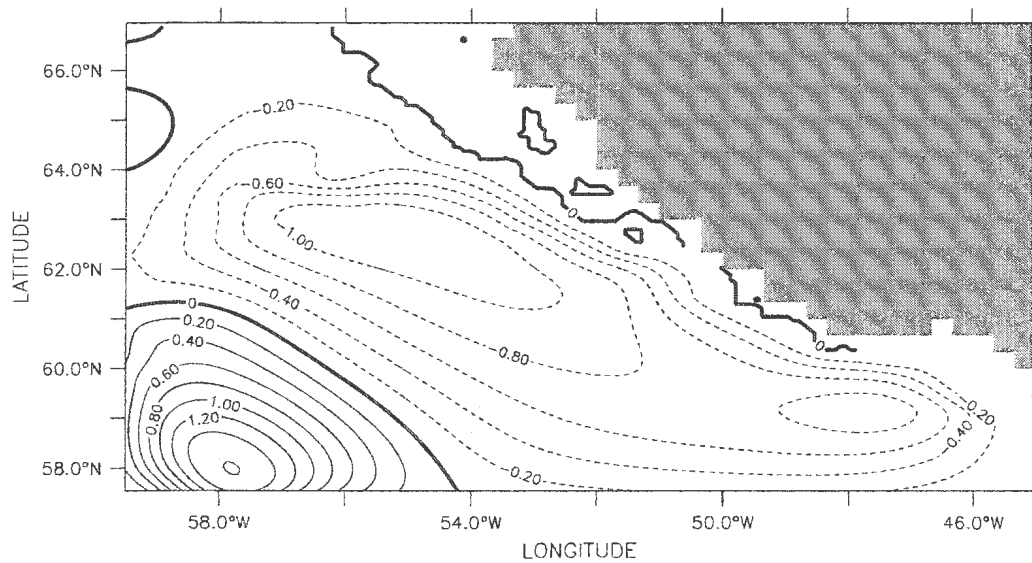


Vertical section of meridional velocity (m/sec) after 30 days

Figure 6.17: Vertical section of meridional velocity at 61° N after 20 and 30 days of model run.

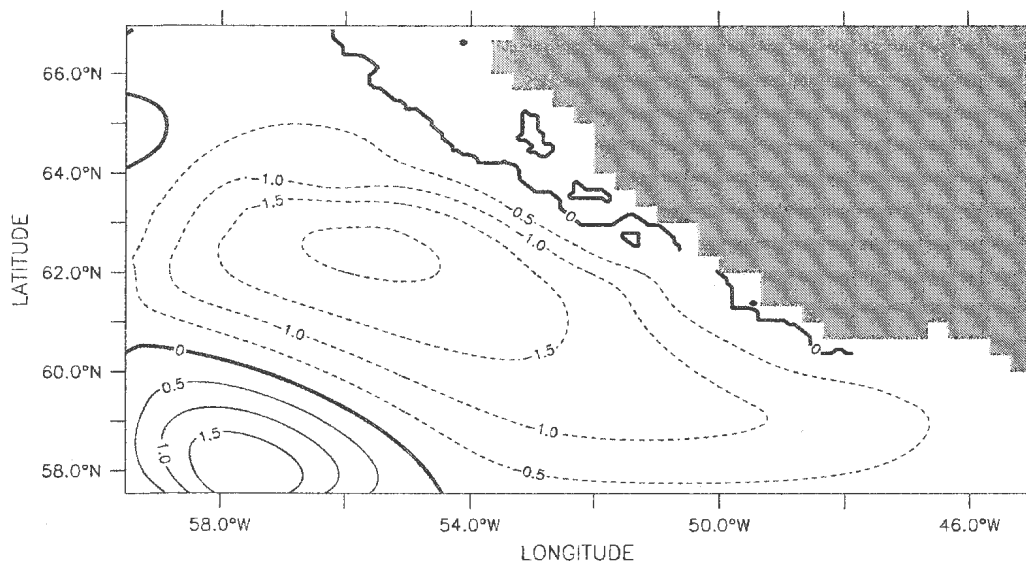


Stream function (Sv) after 5 days

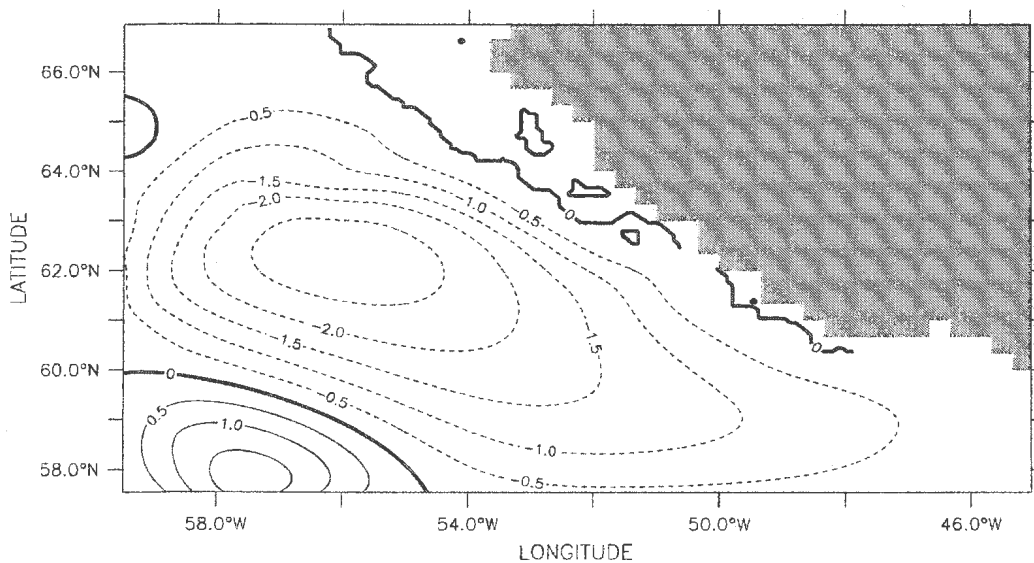


Stream function (Sv) after 10 days

Figure 6.18: Stream function after 5 and 10 days of model run. Positive values (solid lines) and negative values (dashed lines) indicate anticyclonic and cyclonic circulation respectively.



Stream function after 20 days



Stream function after 30 days

Figure 6.19: Stream function after 20 and 30 days of model run. Positive values (solid lines) and negative values (dashed lines) indicate anticyclonic and cyclonic circulation respectively.

wind driven flow and the current flow gets augmented and flows eastward which feeds into the poleward flowing coastal current.

A time sequence of the vertical cross-section of the meridional velocity at 61° N is shown Figs. 6.16 and 6.17. The flow patterns in these figures show the vertical structure of the poleward surface current and a southward flowing undercurrent. After 20 days of model run (Fig. 6.17), the poleward flowing current axis is located ~ 80 km off the coast and extends from ~ 100 m depth near the coast to ~ 1000 - 1300 m depth offshore. Core velocities range from ~ 0.02 to 0.03 ms^{-1} . A weaker undercurrent with a core velocity of $\sim 0.001 \text{ ms}^{-1}$ is also seen. A comparison of the poleward flowing current and the opposite flowing undercurrent after 5 days (Fig. 6.16) and that after 30 days (Fig. 6.17) shows that as the core of the undercurrent becomes wider, it displaces the core of the poleward flowing current farther off-shore. As a result, there may be vertical and horizontal shear instabilities between the poleward surface current and the undercurrent that could lead to the development of meanders and eddies. The evidence of meanders and developed eddies can be seen in the velocity and the stream function fields (Figs. 6.8 - 6.11, Fig. 6.18 and Fig. 6.19) after 5 days of model run. Three distinct stream function cells (Fig. 6.18) develop along the irregular coastline of the model domain between $\sim 59^\circ$ N and 64° N. The cells are cyclonic, and have a diameter of ~ 30 - 50 km with alongshore spacings of ~ 100 - 200 km between them. A qualitative comparison of the results of the model simulation with the results of the analyses of NOAA-AVHRR infrared images (Chapter

5) obtained over the West Greenland region suggests that both model and image analysis show the presence of meanders and eddies between $\sim 59^\circ$ N and 64° N along the coast of West Greenland. In particular, the diameters of the eddies present in the images obtained between 30 th June 1995 and 29 th July 1995 (~ 30 -60 km, Figs. 5.5 - 5.8, Chapter 5) compares well with the results obtained using the model. On the basis of these results, it is seen that the phenomenological behaviour of the model simulations is qualitatively similar to the results of the analyses of NOAA-AVHRR infrared images. It should be noted that the numerical model is run for 90 days. The length of this time period was chosen to include the generation of current and eddies that may form on the flow. Also, as the model does not include any seasonal variations in the forcing mechanisms nor does it include any storm scale variability in the wind forcing that may generate meanders/eddies, it is unrealistic to run the model for a longer period.

6.3 Summary

In this chapter, first a numerical experiment was performed to test the behaviour of the latest version of the chosen model (MOM2) that covers the waters of the West Greenland to the initial and boundary conditions. An initial sharp perturbation (density front) was used in this numerical experiment, and a passive open boundary condition was chosen along the open boundaries. Results of the model experiment show the formation of baroclinic Kelvin waves and successful passage of the waves through the open boundaries of the model without distorting the interior solution. Results also show the satisfactory

behaviour of the model. Based on the computation of internal Rossby radius of deformation for first vertical mode (~ 11 km), it was found that the grid spacing of $1/6^\circ \times 1/6^\circ$ (which is ~ 9 km and 18 km in zonal and meridional directions) was not adequate enough to resolve the Rossby radius in both directions. Next, the effects of wind and thermal forcing in the generation of current meanders and eddies using the model with ETOPO5 bottom topography were examined. In this experiment, the grid spacing was decreased to $1/12^\circ \times 1/12^\circ$ (which is ~ 5 km and 9 km in zonal and meridional directions), sufficient to resolve the Rossby radius of deformation in both directions. Results of the experiment indicate that the flow induced by the temperature gradient establishes a steady poleward flowing surface current and an undercurrent flowing in the opposite direction. In time the core of the surface current gets displaced and moves offshore, suggesting vertical and horizontal shear between the poleward surface current and the undercurrent that could lead to instabilities and result in the generation of meanders and eddies. Wind forcing effects were clearly discernible at the southern end of the model domain, but the flow generated by temperature gradient is seen to oppose the flow generated by wind forcing. A qualitative comparison of the results of model simulation with the results of the analyses of NOAA-AVHRR images obtained over the West Greenland region suggest that both model and images show the presence of current meanders and eddies. These numerical experiments carried out using a fully three dimensional regional, ocean circulation model provide insight into the dynamical processes responsible for the generation of current meanders and eddies, and will help in designing complex investigations with

more realistic initial and boundary conditions.

Chapter 7

Summary and Discussion

The installation of a satellite receiving station in Northwest Atlantic Fisheries Centre, St. John's provided AVHRR data over the West Greenland region. Despite the problems of excessive cloudiness over this region, sufficient number of images acquired during 1995 and 1996 could be found that represented the summer and fall conditions. Preprocessing steps such as identification of missing scanlines, radiometric calibration to convert thermal infrared data to brightness temperatures, image navigation to correct for geometric distortions due to earth shape/rotation and satellite orbit variations, cloud identification and land masking were performed to the selected images. The processed thermal imagery reveals the presence of interesting oceanographic features over the waters of the West Greenland region. A distinct feature that could be identified in all the analysed images is the sea surface front characterized by frontal waves, meanders and eddies between the cold East Greenland Current water of Arctic origin and the warm Irminger Current water of Atlantic origin. Although, we did not have simultaneous shipboard observations in the West Greenland region to validate the features observed in the satellite images, examination of the available hydrographic conditions collected during July 1994

and January 1995 indicate the existence of two current components, the cold East Greenland Current and the warm Irminger Current. Many of the mesoscale features identified in the satellite images have important implications for the origin and maintenance of the regions marine ecosystems, including shelf edge exchange processes, and stratified slope water intrusions onto the shelf. Such processes provide a mechanism for injection of nutrient rich waters into the upper layers of the ocean, thus increasing the productivity of the region.

A three-dimensional, primitive equation regional model that covers the waters off the coast of West Greenland was used to examine the dynamical processes responsible for the generation of current meanders and eddies. As the model used is the latest version of the GFDL MOM2 model, first a numerical experiment was conducted to test the behaviour of the model, and to verify the response of the model to the chosen initial and open boundary conditions. An idealized sharp density front based on the hydrographic observations off the coast of West Greenland was chosen to initialize the model from rest. Along the open boundaries of the model, a passive open boundary condition in which there is no forcing at the boundary and phenomena generated within the model domain are allowed to pass out without distorting the interior was used. The motivation to choose these initial and boundary conditions were based on the papers by Hsieh and Gill (1984) and Stevens (1990). The results show the formation of two baroclinic Kelvin waves, and the chosen boundary condition allows the Kelvin waves to propagate out of

the model domain without affecting the interior solution. It was also found that the grid resolution of $1/6^\circ \times 1/6^\circ$ (which is ~ 9 and 18 km in zonal and meridional directions) was not adequate enough to resolve the internal Rossby radius of deformation ~ 11 km (computed using the potential density profile based on the hydrographic observations off the coast of West Greenland) in both the directions. Next, an experiment was carried out using the model with realistic bottom topography (ETOPO5 topography) to investigate the combined effects of wind and thermal forcing in the generation of current meanders and eddies. In this experiment, the grid spacing was decreased to $1/12^\circ \times 1/12^\circ$ (~ 5 and 9 km in zonal and meridional directions), adequate to resolve the Rossby radius in both the directions. The wind and thermal forcings used in this experiment were based on the zonal averages of annual mean wind stress and temperature data of Hellerman and Rosenstein (1983) and Levitus (1982) respectively. In response to the wind and thermal forcings, a poleward flowing surface current and an undercurrent flowing in the opposite direction were generated. In time the core of the poleward flowing current gets displaced and moves offshore suggesting that there may be both horizontal and vertical shear that could lead to instabilities and development of meanders and eddies. A qualitative comparison of the results of the model simulation and NOAA-AVHRR image analyses obtained over West Greenland suggest that the phenomenological behaviour of the model simulations is similar to the mesoscale features observed in the satellite images.

In summary, the analyses of the NOAA-AVHRR infrared images provide a clear picture of the spatially complex frontal system in the West Greenland region. The AVHRR imagery is thus proven to be a valuable tool for spatial/temporal analysis of oceanographic features in this region, for hypothesis formation in dynamical and modelling studies. The results call for a plan to a well coordinated field program designed to further investigate the features observed, and to merge active radar observations from oceanographic satellite such as ERS-1 and 2, RADARSAT and TOPEX/Poseidon with the NOAA-AVHRR data. The numerical modelling studies help us to understand the complicated dynamics involved in modelling the mesoscale features such as meanders and eddies, and call for a detailed investigation with more realistic initial and boundary conditions.

REFERENCES

- Apel, J.R., 1980: Satellite sensing of ocean surface dynamics. *Annu. Rev. Earth Planet. Sci.*, **8**, 304.
- Aagaard, K and E.C. Carmack, 1989: The role of sea-ice and other freshwater in the Arctic circulation. *J. Geophys. Res.*, **94**, 14485-14498.
- Barton, I.J., 1995: Satellite-derived sea surface temperatures: Current status. *J. of Geophysical Res.*, **100**, C5 8777-8790.
- Blaeck, R., R. Onke and J.D. Woods, 1988: A two dimensional model of mesoscale frontogenesis in the ocean. *Q. J. R. Meteorol. Soc.*, **114B**, 347-372.
- Borstad, G.A., R.M. Brown, D. Truax, T.R. Mulligan and J.F.R. Gower, 1982: Remote sensing techniques for fisheries oceanography: examples from British Columbia. *NAFO Sci. Coun. Studies*, **4**, 69-76.
- Bottomley, M., C.K. Folland, J. Hsiung, R.E. Newell and D.E. Parker, 1990. Global Ocean Surface Temperature Atlas, MIT press, Cambridge, Mass.
- Bowman and R.L. Iverson, 1987: Estuarine and plume fronts. In *Oceanic Fronts in Coastal Processes*. Springer-Verlag, Newyork, pp.87
- Brouwer, D., 1959: Solution of the problem of artificial satellite theory without drag. *Astron. J.*, **64**, 378-397.
- Bruce, J.G., 1995: Eddies southwest of Denmark Strait. *Deep-sea Research*, **42**, 1 13-29.
- Bryan, K., 1969: A numerical method for the study of the circulation of the world ocean. *J. Computational Physics*, **4**, 347-376.
- Bryan, K., S. Manabe and R.C. Pacanowski, 1975: A global-atmosphere Climate model. Part II. The oceanic circulation. *J. Phys. Oceanogr.*, **5**, 30.
- Buch, E., 1982: Review of Oceanographic Conditions in Subareas 0 and 1 during the 1970-79 Decade: *NAFO Sci. Coun. Studies*, 43-50.
- Bullard, R.K., 1983a: Land into sea does not go. In *Remote Sensing Applications in Marine Science and Technology*, edited by A.P. Cracknell (Dordrecht: D. Reidel). P. 373.
- Canon, G.Y and D.R. Maynard, 1983: An aerial survey of fishing effort in the lobster fishery of the northern Northumberland Strait. *CAFSAC Research Document*, 83/28, pp 15.
- Churchill, J.H and P.C. Cornillon, 1991: Water discharged from the Gulf Stream north of Cape Hatteras. *J. Geophys. Res.*, **96**, 22227.

- Clarke, R.A., 1984: Transport through the Cape Farewell-Flemish Cap section. *Rapp. P-v Reun. Cons. int. Explor. Mer.*, **185**, 120-130.
- Clarke, R.A. and J.C. Gascard, 1983: The formation of Labrador Sea water: Part I, Large Scale processes. *J. of Phys. Oceanogr.*, **13(10)** 1764-1768.
- Côté, S and A.R.L. Tatnall 1995b: Estimation of ocean surface currents from satellite imagery using a Hopfield neural network. *Proceedings of the Third Thematic conference on Remote Sensing for Marine and Coastal Environments.*, Seattle, WA, 18-20 September 1995 (Ann Arbor, MI:ERIM), Vol. I, 538-549.
- Cotter, D.J., 1990: The United States operational polar and geostationary satellite. *Weather satellite: System, Data and Environmental Applications*. P.K. Rao, S.J. Holmes, R.K. Anderson, J.S. Winston and P.E. Lehr, Eds., American Meteorological Society, Boston, chap III, 1.
- Cracknell, A.P and W.G. Huang, 1988: Surface currents off the west coast of Ireland studied from satellite images. *Int. J. Remote Sensing*, **9**, 439.
- Davey, M.K., W.W. Hsieh and R.C. Wajsowicz, 1983: The free Kelvin wave with lateral and vertical viscosity. *J. Phys. Oceanogr.*, **13**, 2182-2191.
- Emery, W.J., W.G. Lee and L. Maggard, 1984: Geographic and seasonal distribution of Brunt-Väisälä frequency and Rossby radii in the North Pacific and North Atlantic. *J. Phys. Oceanogr.*, **14**, 294-317.
- Emery, W.J., A.C. Thomas, M.J. Collins, W.R. Crawford and D.L. Mackas, 1986: An objective method for computing advective surface velocities from sequential infrared satellite images. *J. Geophys. Res.*, **91**, 12865- 12878.
- Emery, W. J., J. Brown and Z. P. Nowak, 1989: AVHRR image navigation: Summary and review. *Photogramm. Eng. Rem. Sen.*, **55**, 1175-1183.
- Emery, W. J., C. Fowler and C.A. Clayson, 1992: Satellite-Image-derived Gulf Stream Currents compared with numerical model results. *J. Atmos. and Oceanic Technology*, **9**, 286-304.
- Fielder, P.C., 1984: Satellite observations of the 1982-1983 El Nino along the U.S. Pacific coast. *Science*, **224**, 1251-1254.
- Fielder, P.C and H. Bernard, 1987: Tuna aggregation and feeding near fronts observed in satellite imagery. *Continental shelf Res.*, **7**, 871-881.
- Flament, P., L. Armi and L. Washburn, 1985: The evolving structure of an upwelling filament. *J. Geophysical Res.*, **90**, 11765-11778.
- Gill, A.E., 1982: *Atmosphere and Ocean Dynamics*. Academic Press, 662 pp.
- Griffiths, R.W and P.F. Linden, 1982: Laboratory experiments on fronts. Part-I: Density-driven boundary currents. *Geophys. Astrophys. Fluid Dyn.*, **19**, 159-187.

- Haidgovel, D.B., A. Beckmann and K.S. Hedstrom, 1991: Dynamical simulation of filament formation and evolution in the coastal transition zone. *J. Geophys. Res.*, **96**, 15017-15040.
- Hsieh, W.W., M.K. Davey and R.C. Wajsowicz, 1983: The free Kelvin wave in finite-difference numerical models. *J. Phys. Oceanogr.*, **10**, 1729-1741.
- Hsieh, W.W. and A.E. Gill, 1984: The Rossby Adjustment problem in a rotating, stratified channel, with and without topography. *J. Phys. Oceanogr.*, **14**(2), 424-437.
- Hellerman, S, and M. Rosenstein, 1983: Normal monthly wind stress over the world ocean with error estimates, *J. Phys. Oceanogr.*, **13**, 1093-1104.
- Hermann, F., P.M. Hansan and Sv.Aa. Horstad, 1965: The effects of temperature and currents on the distribution and survival of cod larvae at West Greenland. *ICANF spec. Publi.*, **6**, 389-395.
- Holland, W.R., 1978: The role of mesoscale eddies in the general circulation of the ocean - Numerical experiments using a wind-driven quasi-geostrophic model. *J. Phys. Oceanogr.*, **8**, 363-392.
- Holland, W.R., D.E. Harrison and A.J. Semtner Jr., 1983: Eddy resolving numerical models of large-scale ocean circulation, in *Eddies in Marine Science*, edited by A.R. Robinson, Springer-Verlag, Newyork, 379-403.
- Hoots F.R. and R.L. Roehrich., 1980: Models for propagation of NORAD elements sets. Project Spacetrack Report No. 3, Dec. 1980.
- Ikeda, M., 1981: Meanders and detached eddies of a strong eastward flowing jet using a two-layer quasi-geostrophic model. *J. Phys. Oceanogr.*, **11**, 526-540.
- Ikeda, M and J.R. Apel, 1981: Mesoscale eddies detached from spatially growing meanders in an eastward flowing oceanic jet using a two-layer quasi-geostrophic model. *J. Phys. Oceanogr.*, **11**, 1638-1661.
- Ikeda, M., W.J. Emery and L.A. Mysak, 1984a: Seasonal variability in meanders of the California Current system off Vancouver island. *J. Geophys. Res.*, **89**, 3487-3505.
- Ikeda, M., L.A. Mysak and W.J. Emery, 1984b: Observations and modelling of satellite-sensed meanders and eddies off Vancouver Island. *J. of Phys. Oceanogr.*, **14**, 3-21.
- Ikeda, M and W.J. Emery, 1984: Satellite observations and modelling of meanders in the California Current system off Oregon and northern California. *J. of Phys. Oceanogr.*, **14** 1434-1450.
- Ikeda, M., 1987: Modeling Interpretation of Mesoscale Meanders of the Ice Edge off the Labrador Coast Observed in NOAA Satellite Imagery. *J. of Phys. Oceanogr.*, **17** 1468-1483.
- Ikeda, M., J.A. Johannessen, K. Lygre and S. Sandven, 1989: A process study of mesoscale meanders and eddies in the Norwegian Coastal Current. *J. of Phys. Oceanogr.*, **19** 20.

- Johannessen, O.M., J.A. Johannessen, J. Morison, B.A. Farrelly and E.A.S. Svedsen, 1983: Oceanographic Conditions in the Marginal Ice Zone North of Svalbard in Early Fall 1979 with an Emphasis on Mesoscale processes. *J. of Geophys. Res.*, **88**, C5, 2755-2769.
- Johannessen, J.A., E.A.S. Svedsen, S. Sandven, O.M. Johannessen and K. Lygre, 1989: Synoptic studies of the three dimensional structure of mesoscale eddies in the Norwegian Coastal Current during winter. *J. of Phys. Oceanogr.*, **19** 3-23.
- Kaula, W.M., 1966: Theory of satellite Geodesy. Waltham, MA: Blaisdell.
- Killworth, P.D., 1983: Long-wave instability of an isolated front. *Geophys. Astrophys. Fluid Dyn.*, **25**, 235-258.
- Killworth, P.D., N. Paldor and M.E. Stern, 1984: Wave propagation and growth on a surface front in a two-layer geostrophic current. *J. Mar. Res.*, **42**, 761-785.
- Kimura, S and T. Sugimoto, 1993: Short-period fluctuations in meander of the Kuroshio's path off Cape Shino Misaki. *J. of Geophys. Res.*, **98**, 2407.
- Krauss, W., R. Döscher, A. Lehmann and T. Viehoff, 1990: On Eddy Scales in the Eastern and Northern North Atlantic Ocean as a function of latitude. *J. of Geophysical Res.*, **95**, C10, 18049-18056.
- Lauritson, L., G.G. Nelson, and R.W. Porto, 1979 (and updates): Data extraction and calibration of TIROS-N/NOAA A-G radiometers. *NOAA Tech. Memo.*, NESS **107**, U.S. Department of Commerce, Washington, D. C.
- Laurs, R.M., P.C. Fielder and D.R. Montgomery, 1984: Albacore tuna catch distribution relative to environmental features observed from satellites. *Deep-sea Res.*, **31**, 1085-1099.
- La Violette, P.E., 1984: The advection of submesoscale thermal features in the Alboran sea Gyre. *J. Phys. Oceanogr.*, **14**, 3, 550-565.
- Lazier, J.R.N., 1973: The renewal of Labrador Sea water. *Deep-Sea Res.*, **20**, 341-353.
- LeBlond, P.H., 1982: Satellite observations of Labrador current undulations. *Atmos.-Ocean.*, **20**, 129-142.
- Lee, A.J., 1968: NORWESTLANT surveys: Physical oceanography. *ICNAF special Publ.*, **7**, Part 1, 31-54.
- Lee, A.J. and D. Ellet, 1967: On the water masses of the North Atlantic Ocean. *Deep-Sea Res.*, **16**, 77-84.
- Lee, T.N., J.A. Yoder and P.A. Atkinson, 1991: Gulf Stream frontal eddy influence on productivity of the Southeast U.S. continental shelf. *J. of Geophys. Res.*, **91**, 22191-22205.
- Legeckis, R., 1975: Application of synchronous meteorological satellite data to the study of time-dependent sea surface temperature changes along the boundary of the Gulf stream. *Geophys. Res. Lett.*, **2**, 435-439.

- Levitus, S., 1982: Climatological atlas of the world ocean, NOAA Prof. Paper 13, US Govt printing Office, Washington, DC.
- Maul, G.A., F. Williams, M. Roffer and F.M Sousa, 1984: Remotely sensed oceanographic patterns and variability of bluefin tuna catch in the Gulf of Mexico. *J. of Oceanologia Acta*, **7**, 469-479.
- Messieh, S.N., 1984: Recent changes in fishing effort and catch rates of inshore herring fisheries in the southern Gulf of St. Lawrence. DFO Gulf region, P.O. Box 5030, Moncton, NB, pp 34.
- Messieh, S.N and P. Macpherson, 1980: Aerial survey of herring gillnets the southern Gulf of St. Lawrence. *Marine Fish Div.* DFO, P.O. Box 1006, Dartmouth, NS., pp 29.
- Montgomery, D.R., R.E. Wittenberg-Fay and R.W. Austin, 1986: The application of satellite-derived ocean colour products to commercial fishing operations. *Marine Tech. Society. J.*, **20(2)**, 72-86.
- Mooers, C.N.K and R.A. Robinson, 1984: Turbulent jets and eddies in the California Current and inferred cross-shore transports. *Science*, **223**, 51-53.
- Nakashima, B.S., G.A. Borstad, D.A. Hill and R.C. Kerr, 1989: Remote sensing of fish schools: early results from a digital imaging spectrometer. Presented at the *IGRASS '89*, 12 the Canadian Symposium on Remote Sensing, Vancouver, B.C., Canada, 2044-2046.
- Niiler, P.P., S. Piasek, L. Neuberg and A. Warn-Varnas, 1992: Sea surface temperature variability of the Iceland-Faeroe front. *J. of Geophys. Res.*, **97**, 17777.
- NOAA Polar Orbiter Data Users Guide, 1990: NESDIS, NOAA, National Climate Data Centre, Satellite Data Service Division, Washington, D.C.
- Oguz, T., P.E. La Violette and U. Unluata, 1992: The upper layer circulation of the Black Sea: its variability as inferred from hydrographic and satellite observations. *J. of Geophys. Res.*, **97**, 12569.
- Orlanski, I., 1968: Instability of frontal waves. *J. Atmos. Sci.*, **25**, 297-332.
- Orlanski, I., 1976: A simple boundary condition for unbounded hyperbolic flows. *J. Comp. Phys.*, **21**, 251.
- Pacanowski, R.C., 1996: MOM2 Version 2, Documentation, User's Guide and Reference Manual. GFDL Ocean Technical Report No. 3.2, Geophysical Fluid Dynamics Laboratory/NOAA Princeton, N.J. 08542.
- Pearce, A.F and R.W. Griffiths, 1991: The mesoscale structure of the Leewin Current: a comparison of laboratory models and satellite imagery. *J. of Geophys. Res.*, **96**, 16739.
- Pedlosky, J., 1964: The stability of currents in the atmosphere and the ocean I. *J. Atmos. Sci.*, **21**, 202-219.

- Peláez and J.A. McGowan, 1986: Phytoplankton pigment patterns in the California Current as determined by satellite. *Limno. Oceanogr.*, **31**, 927-950.
- Pingree, R.D., 1978: Cyclonic eddies and cross-frontal mixing. *J. Mar. Biol. Ass., U.K.*, **58**, 955-963.
- Pingree, R.D, G.R. Forster and G.K. Morrison, 1974: Turbulent convergent tidal fronts. *J. Marine Biological Assoc. of U.K.*, **54**, 469-479.
- Pingree, R.D and D.K. Griffiths, 1978: Tidal fronts on the shelf seas ground the British Isles. *J. Geophys. Res.*, **83**, 4615-4622.
- Ramos, A.G., J. Santiago, P. Sangra and M. Canton, 1992: An application of satellite derived temperature data to the skipjack (*Katsuwonus pelamis* Linnaeus, 1758) and albacore tuna (*Thunnus alalunga* Bonaterre, 1788) fisheries in the north-east Atlantic. *Int. J. Remote sensing*, **17**, 749-759.
- Randerson, J.T and J.J. Simpson, 1993: Recurrent patterns in surface thermal fronts associated with cold filaments along the west coast of North America. *Remote Sens. Environ.*, **46**, 146-163.
- Reeves, R.G., 1975: *Manual of remote sensing*. American Society of Photogrammetry, Falls Church, Virginia, U.S.A, Vols. I and II, 2144pp.
- Richardson, P.L., 1980: Gulf Stream ring trajectories. *J. Phys. Oceanogr.*, **10**, 90.
- Robinson, A.R., M.A. Spall and N. Pinardi, 1988: Gulf Stream simulations and the dynamics of ring and meander processes. *J. of Phys. Oceanogr.*, **18**, 1811.
- Rosborough, G. W., D.G. Baldwin and W.J. Emery, 1994: Precise AVHRR image navigation. *IEEE Trans. On Geosci. and Rem. Sen.*, **32**, 644-657.
- Scwalb, A., 1978: The TIROS-N/NOAA satellite series. *NOAA Tech. Memo.*, NESS **95**, U.S. Department of Commerce, Washington, D. C.
- Scwalb, A., 1990: The ATN and GOES sensors. *Weather satellite: System, Data and Environmental Applications*. P.K. Rao, S.J. Holmes, R.K. Anderson, J.S. Winston and P.E. Lehr, Eds., American Meteorological Society, Boston, chap IV, 2.
- Semtner, A.J., 1986: Finite-difference formulation of a world ocean model. In *Proceedings of the NATO Advanced study institute on Advanced Physical Oceanographic Numerical Modelling* (J.J. O' Brien, ed.), D. Reidel Publishing Co., Dordrecht, 187-202.
- Simpson, J.H., 1981: The shelf-sea fronts- implications of their existence and behaviour. *Phil. Trans. Roy. Soc. London*, **A302**, 531-543.
- Simpson, J.J., 1987: Transport processes affecting the survival of pelagic fish stock in the California Current. *Am. Fish. Soc. Symp.*, **2**, 39-60.
- Simpson, J.J., 1994: Remote sensing in Fisheries: A tool for better management in the utilization of renewable resource. *Can. J. Fish. Aquat. Sci.*, **51**, 743-771.

- Simpson, J.H., D.G. Hughes and N.C.G. Moris, 1977: The relation of seasonal stratification to tidal mixing on the continental shelf. In: *Angel, M. (ed.), A voyage of discovery*, Oxford, Pergamon press, pp327-340.
- Smith, D.C., IV, J.H. Morison, J.A. Johannessen and N. Untersteiner, 1984: Topographic generation of an eddy at the edge of the East Greenland Current. *J. of Geophys. Res.*, **89**, 8205-8208.
- Stein, M., 1994: Climatic conditions around Greenland. *NAFO Sci. Coun. Studies*, **25**, 59-65.
- Stein, M. and E. Buch., 1985: 1983: an unusual year off West Greenland? *Arch. FischWiss*, **36**, 81-92.
- Stern, M.E., J.A. Whitehead and B.L. Hua, 1982: The intrusion of a density current along the coast of a rotating fluid. *J. Fluid Mech.*, **123**, 237-265.
- Stevens, D.P., 1990: On open boundary conditions for three dimensional primitive equation ocean circulation models. *Geophys. Astrophys. Fluid Dynamics*, **51**, 103-133.
- Stommel, H., 1966: *The Gulf Stream*. University of California Press, 248pp.
- Straka, J., J. Klokocnik and H. Grabl, 1989: Navigation of satellite measurements without ground control points. *Int. J. Rem. Sens.*, **14**, 1181-2003.
- Sund, P., M. Blackburn and F. Williams, 1981: Tunas and their environment in the Pacific Ocean: a review. *Oceanography and Marine Biology Annual Reviews*, **19**, 443-512.
- Sur, H.I., E. Ozsoy, Y.P. Ilyin and U. Unluata, 1996: Coastal/deep ocean interactions in the Black Sea and their ecological/environmental impacts. *J. Marine Systems*, **7**, 293-320.
- Svejkovsky, J., 1988a: Sea surface flow estimation from Advanced Very High Resolution Radiometer and Coastal Zone Colour Scanner satellite imagery. A verification study. *J. of Geophys. Res.*, **12**, 1189-1205.
- Svejkovsky, J., 1988b: Fishfinding from space. *Saltwater Sportsman* 50: 96-87f, 178-179.
- Talley, L.D and M.S. McCartney, 1982: Distribution and circulation of Labrador Sea water. *J. of Phys. Oceanogr.*, **19** 3-23.
- Thompson, R.E. and J.F.R. Gower, 1985: A wind induced Mesoscale eddy over Vancouver Island Continental slope. *J. of Geophysical Res.*, **90**, C5, 8981-8993.
- Turner, G.S., 1981: Small scale mixing processes. In. *evolution of Phys. Ocean*, Edited by Bawrren and C. Wunsch, 236-262.
- Vaughan, R.A and I.D. Downey, 1988: Circulation patterns in AVHRR imagery. *Int. J. Remote sensing*, **9**, 697-700.

- Vastano, A.C. and S.E. Borders, 1984: Sea surface motion over an anticyclonic eddy on the Oyashio front. *Remote Sens. Environ.*, **16**, 87-90.
- Vastano, A.C. and R.O. Reid, 1985: Sea surface topography estimation with infrared satellite imagery. *J. Atmos. Oceanic Technol.*, **2**, 393-400.
- Vastano, A.C., S. Borders and R. Wittenberg, 1985: Sea surface flow estimation with infrared and visible imagery. *J. of Atmos. and Oceanic Technology*, **2**, 401-403.
- Wadhams, P., 1981: The ice cover in the Greenland and Norwegian seas. *Rev. Geophys. Space Phys.*, **19(3)**, 345-393.
- Wadhams, P., and V.A. Squire, 1983: An ice-water vortex at the edge of the East Greenland Current. *J. Geophys. Res.*, **88**, 2770-2780.
- Wahl, D.D. and J.J. Simpson, 1990: Physical processes affecting the objective determination of near-surface velocity from satellite data. *J. Geophys. Res.*, **95**, 13511-13619.
- Wegner, G., 1973: Geostrophische Oberflächenströmung im nördlichen Nordatlantischen Ozean im Internationalen Geophysikalischen Jahr 1957-58. *Ber. Dt. Wiss. Komm. Meeresforsch.*, **22**, 411-426.
- Wertz, J.R., 1978: *Spacecraft Attitude Determination and Control*. Dordrecht, The Netherlands: D. Reidel.



